Changes in Microstructure and Mechanical Properties of Aluminum Alloys Heavily Deformed by Torsion

By

Sunisa Khamsuk

A Dissertation submitted to Kyoto University for
Doctor of Philosophy in Engineering

Department of Materials Science and Engineering
Graduate School of Engineering

Kyoto University

2013

TABLE OF CONTENTS

Chapter 1 Background and purpose

1.1 Introduction

During last 50 years, aluminum has been the second most used metallic material after the iron and steels in industries [1], which is owing to its characteristic properties. Aluminum alloys have various advantages among lots of metallic materials, such as high ductility, good formability, light weight, strength, and easy recyclability. Even though aluminum alloys have good mechanical properties as mentioned above, its strength is not sufficient for some commercial uses. Therefore, several methods, such as adding alloying elements (i.e., Cu, Mg, Si, Fe, Cr and so on) [2], surface treatments [3] and grain refinement [4, 5-12], have been suggested to improve the strength of aluminum alloys for fulfilling the demands. From an economical point of view, grain refinement appears to be the most effective way to improve the strength of aluminum alloys with low cost. Grain refinement is well known as the method to enhance strength of metals and alloys, and the relationship between yield strength (σ_y) and mean grain size (D) is described by the Hall-Petch relationship [13, 14]:

$$\sigma_y = \sigma_0 + k_y D^{-\frac{1}{2}} \tag{1.1}$$

where σ_0 is the friction stress required to move dislocation in coarse-grained materials, and k_y is the Hall-Petch coefficient. According to **Eq.1.1**, the strength increases with decreasing the mean grain size. In addition, it has been also reported that the toughness and superplastic properties are enhanced by the decrease in grain size [15]. Furthermore, some researchers have shown interesting experimental results that the ultrafine-grained

(UFG) aluminum having the mean grain size smaller than 1 μm exhibits a surprisingly higher strength than that of the conventional coarse-grained aluminum [16] as well as unique deformation behaviors that have never been observed in coarse-grained counterparts [5]. These are the motivation for widespread research works in ultrafine grained metallic materials.

1.2 Techniques to fabricate the ultrafine grained materials

Owing to the growing interests in UFG materials, a number of techniques for fabricating UFG structures in metallic materials have been developed. In general, conventional fine-grained metallic materials could be produced by cold rolling followed by annealing which results in recrystallization characterized by nucleation and growth of new grains. However, the minimum grain size obtained by this process was approximately 10 μm in aluminum alloys [5]. It is well known that aluminum has high stacking fault energy so that dynamic recovery during plastic deformation at low temperatures and static recovery during annealing process can easily happen to decrease the driving force for recrystallization. Therefore, it is difficult to produce UFG structures having mean grain size smaller than 1 μm in aluminum alloys by this route.

In the last two decades, UFG aluminum alloys having mean grain sizes smaller than 1 μm have been successfully produced. For obtaining UFG structures, bulk materials are severely deformed to ultra high strain, which is called "severe plastic deformation (SPD)" processes. Recently, various SPD techniques are available for introducing high strain into bulk materials, such as cyclic extrusion and compression (CEC) [17], multi-directional forging [18], twist extrusion [19], high pressure torsion (HPT) [20-22], equal channel angular pressing (ECAP) [23-25], and accumulative roll

bonding (ARB) [26, 27]. Here, three SPD processes, which are intensively studied, are described.

1.2.1 High pressure torsion (HPT)

HPT is the most famous and successful SPD process for producing bulk UFG metals and alloys. The principle of the HPT process is schematically shown in **Fig. 1.1 (a)**. The small disk sample is placed onto the lower die, subsequently compressed by the upper die (plunger) under a high pressure of several GPa, and then subjected to torsion straining along the peripheral direction of the disc by rotating the plunger. By this process, fine grain sizes in a range of 20 nm to 50 nm could be obtained. However, the HPT has the disadvantage that the sample sizes are fairly small, which are generally smaller than 1 mm in thickness and 20 mm in diameter [22].

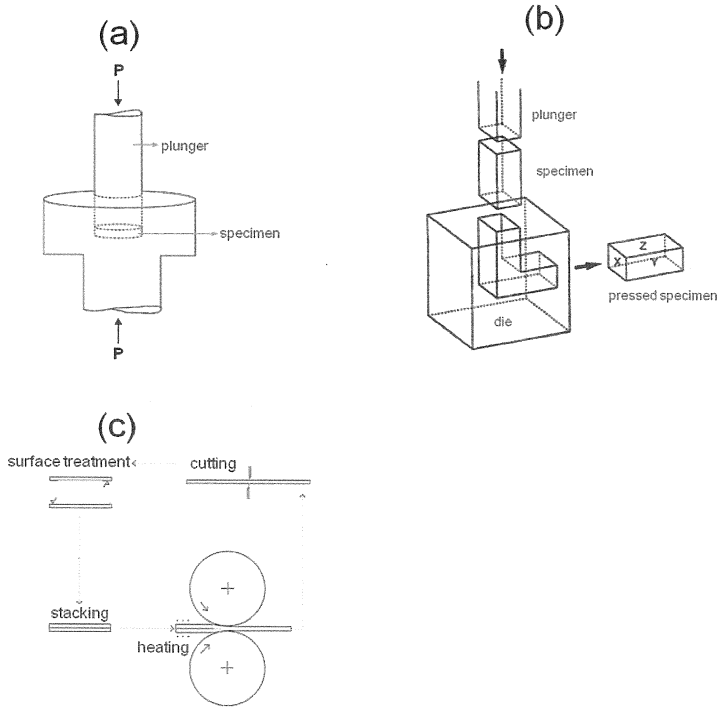

Fig. 1.1 Schematic illustrations showing the procedures of the several SPD processes: (a) HPT [10], (b) ECAP [25], and (c) ARB [27].

1.2.2 Equal channel angular pressing (ECAP)

ECAP is one of the most common methods of SPD for fabricating bulk ultrafine grained metallic materials. The principle of ECAP is illustrated schematically in **Fig. 1.1 (b)**. A bar specimen is pressed through the die having an angular channel by a plunger. The specimen is deformed in simple shear when the specimen passes the corner of the channel. Because cross-sectional area of the specimen is constant even after the pass, the procedures can be repeated limitlessly so that the large plastic strain is imposed on the materials. During last two decades, the formation of UFG structure in aluminum and magnesium alloys during ECAP has been extensively studied [25] since there alloys have relatively low flow stresses. In the ECAP, the specimens can be deformed also at elevated temperatures. However, it should be noted here that ECAP is a discontinuous "batch" process.

1.2.3 Accumulative roll bonding (ARB)

ARB has been developed by Saito et al. in 1998 [27]. The principle of the ARB is schematically shown in **Fig. 1.1 (c)**. ARB is a SPD process using the rolling deformation, which is the most advantageous metal working process for producing bulky metallic materials (plates, sheets, bars, etc.) continuously. In the ARB, SPD is introduced into the sheet materials without geometrical change of the sheet. This is achieved by repeating the procedure where cutting the 50%-rolled sheet into two pieces, then degreasing and wire-brushing once side of the surfaces of the sheets, stacking them together to make the total dimensions of the sheet initial one, and rolling them [27]. Here, the rolling in the ARB process is not only a deformation process but also a bonding process, i.e., roll bonding, so that one-body solid material could be obtained.

The ARB has a potential to be a continuous process in the industry, but it is carried out as a "batch" process substantially in laboratory experiments.

1.2.4 Possibility of torsion deformation

Although those SPD processes mentioned above have high capacity to produce UFG metallic materials, the major drawback of those processes is that they are discontinuous processes. Discontinuous processes have the disadvantage of the limitation on controlling the deformation conditions such as temperature and strain rate during the processing. It is well known that the evolution of microstructure of metals and alloys are strongly dependent on deformation parameters (i.e., strain, strain rate and deformation temperature). Hence, those processes are not suitable tools for studying the effects of deformation temperature and strain rate on the microstructure evolution in the metallic materials. Therefore, in order to study the effect of deformation conditions on the change of microstructure during SPD, it is necessary to use the continuous SPD process. Torsion could be a promising process to clarify the effects of deformation parameters on the evolution of microstructure during severe plastic deformation.

Torsion deformation is a simple shear deformation process, which has an ability to introduce ultra high strain to bulk metallic materials continuously. The principle of the torsion deformation and the detail of the torsion deformation machine are shown in **Fig. 1.2 (a)** and **(b)**, respectively. The bar specimen is placed into the torsion machine, and then the specimen is subjected to torsion deformation by rotating one end of the bar specimen. In the torsion deformation, the strain rate and deformation temperature could be controlled preciously throughout the process. The strain rate is altered simply by changing the rate of rotation, and it is possible to achieve strain rates ranging from 10^{-4}

s^{-1} to 10^2 s^{-1} in the torsion machine used in this study. For the elevated temperature deformation in the torsion machine used in the present study, the specimens were heated up by the induction coil to the deformation temperature. The deformation temperature was controlled by the thermocouple welded at the edge of the gauge section. The heated specimens were subjected to torsion deformation under a constant deformation temperature and a constant rotation speed. After that the hot deformed specimens were quenched by water injection. The torque and angular displacement were recorded during the torsion deformation, for constructing stress-strain behaviors in torsion deformation. The torsion specimens with 4 mm in the gauge length and 8 mm in the diameter were used in the present study.

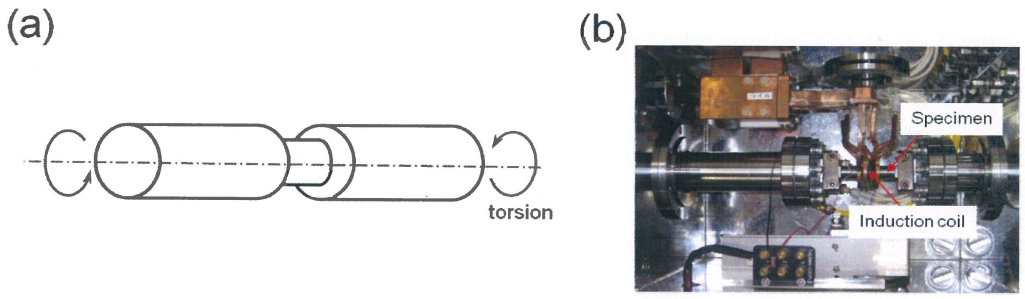

Fig. 1.2 (a) Schematic diagram of the torsion deformation. (b) Inside view of the chamber of torsion deformation machine.

In the torsion deformation, the equivalent strain (ε_{eq}) and equivalent stress (σ) can be calculated using the classical equations shown below [28-30]:

$$\varepsilon_{eq} = \frac{2\pi RN}{L\sqrt{3}} \tag{1.2}$$

$$\sigma = \frac{M}{2\pi R^3\sqrt{3}}(3+k+m) \tag{1.3}$$

where R is the radius, L is the gauge length, N is the number of rotations, M is the

torsion moment, k is the strain-hardening coefficient (k was taken as zero, which is valid merely at the peak torque and in steady-state flow), m is the strain rate sensitivity described by $\{\log M / \log \dot{\varepsilon}\}_T$ and $\dot{\varepsilon}$ is the strain rate. The torsion moment (torque) is recorded during the torsion deformation.

1.3 Objective and strategy of the present study

UFG materials have become the subject of interest in material science researches, because of their unique structures and outstanding mechanical properties as compared with the coarse grained materials. The most widely used techniques for fabricating bulk UFG metals and alloys have been SPD processes, such as ARB [27], HPT [22] and ECAP [25]. However, as the author mentioned in the previous section that these processes are batch processes, in other words, discontinuous processes, so that some of the important deformation parameters, such as strain rate and deformation temperature, cannot be controlled precisely during deformation. It is well known that those deformation parameters have a strong effect on the microstructure evolution of metallic materials. Therefore, the formation mechanism of UFG structures during SPD has been discussed only as a function of strain, and it has not yet been fully clarified. In order to clarify the influences of deformation conditions (especially, temperature and strain rate) on the development of ultrafine grained microstructures in aluminum and its alloys during SPD process, it is necessary to employ a simple and reliable testing or deformation technique in which temperature and strain rate are precisely and continuously controlled. From such a viewpoint, torsion deformation could be a promising continuous SPD process in which heating rate, deformation temperature, imposed strain and strain rate can be accurately controlled. Torsion deformation is not a new technique. It has been used for more than 50 years as the method for evaluating hot

workability of materials and for simulating thermomechanical processing such as multipass bar rolling [30]. However, the torsion deformation has been rarely used as a SPD process for fabricating bulk ultrafine grained materials. It is expected that the grain refinement mechanism and the microstructural characteristic of the ultrafine grains fabricated by SPD under well-controlled temperature and strain rate could be clarified by torsion deformation. Therefore, the purposes of the present study are as follows:

1. To clarify whether the torsion deformation can act as a SPD process to fabricate UFG structures, by studying the effect of strain on microstructural change in a commercial purity aluminum during torsion deformation at ambient temperature, and to clarify the grain refinement mechanism.
2. To study the effect of deformation conditions, i.e., strain rate and temperature, on the change in microstructure evolution in the pure aluminum during torsion deformation.
3. To investigate the mechanical properties of the UFG pure aluminum fabricated by torsion deformation.
4. To clarify the effect of precipitate on the formation of ultra fine grained structures during torsion deformation under various deformation conditions, using an Al-Cu alloy.

1.4 Outline of the thesis

The present dissertation consists of five chapters. In **Chapter 1**, the background and purpose of this dissertation are explained.

The bulk UFG metallic materials have been successfully produced by SPD processes. It has been known that a certain strain is required to achieve ultrafine grain with having high angle grain boundary. In **Chapter 2**, the evolution of the microstructure in the commercial purity aluminum heavily deformed by torsion

deformation is investigated. It is found that the UFG aluminum having mean grain size of 0.33 μm could be obtained after imposed strain of 5.27. This result indicated that torsion deformation worked as a kind of the SPD processes. The effect of deformation temperature and strain rate on the stress–strain behavior and microstructure evolution of the commercial purity aluminum during torsion deformation are also systematically studied.

In **Chapters 3**, mechanical properties of the UFG aluminum fabricated by torsion are investigated through tensile test. The strengthening mechanism is discussed, based on the microstructural parameters obtained in **Chapter 2**. The high strength is expected in the UFG aluminum produced by torsion deformation.

In **Chapter 4**, the effect of precipitate on the microstructure evolution of the aluminum alloy is clarified. The Al-Cu alloy is chosen for this study, because this material is widely used in the industries. Moreover, the effect of precipitates on the formation of the UFG structure during torsion deformation is rarely studied in this alloy.

In **Chapter 5**, conclusions and achievements in the present dissertation are summarized.

References

[1] Lumley RN (2011)
Fundamentals of aluminium metallurgy; production, processing and applications. 1st ed, Woodhead publishing limited, UK: 1.

[2] Rana RS, Purohit R and Das S
Reviews on the influences of alloying elements on the microstructure and mechanical properties of aluminum alloys and aluminum alloy composites.
IJSRP (2012) 2:1-7.

[3] Funatani K
Emerging technology in surface modification of light metals.
Surg Coat Tech (2000) 133-134:264-272.

[4] Masumura R, Hazzledine PM and Pande CS
Yield stress of fine grained materials.
Acta Mater (1998) 46:4527-4534.

[5] Tsuji N, Ito Y, Saito Y and Minamino Y
Strength and ductility of ultrafine grained aluminum and iron produced by ARB and annealing.
Scripta Mater (2002) 47:893-899.

[6] Yu CY, Kao PW and Chang CP
Transition of tensile deformation behaviors in ultrafine-grained aluminum.
Acta Mater (2005) 53:4019-4028.

[7] Huang X, Kamikawa N and Hansen N
Strengthening mechanisms in nanostructured aluminum.
Mater Sci Eng A (2008) 483-484:102-104.

[8] Kamikawa N, Huang X, Tsuji N and Hansen N
Strengthening mechanisms in nanostructured high-purity aluminium deformed to high strain and annealed.
Acta Mater (2009) 57:4198-4208.

[9] Bowen JR, Prangnell PB, Jensen D Juul and Hansen N
Microstructural parameters and flow stress in Al–0.13% Mg deformed by ECAE processing.
Mater Sci Eng A (2004) 387-389:235-239.

[10] Meyers MA, Mishra A and Benson DJ
Mechanical properties of nanocrystalline materials.
Prog Mater Sci (2006) 51:427-556.

[11] Hall EQ
The deformation and ageing of mild steel: III discussion of results.
Proc Phys Soc B (1951) 64:747-753.

[12] Choi HJ, Lee SW, Park JS and Bae DH
Tensile behavior of bulk nanocrystalline aluminum synthesized by hot extrusion of ball- milled powders.
Scripta Mater (2008) 59:1123-1126.

[13] Danaf EI, Soliman E, Almajid MS and Rayes MM
Enhancement of mechanical properties and grain size refinement of commercial purity aluminum 1050 processed by ECAP.
Mater Sci Eng A (2007) 458:226-234.

[14] Petch NJ
The fracture of metals.
Prog Metal Phy (1954) 5:1-52.

[15] Valiev RZ, Zehetbauer MJ and Estrin Y
The innovation potential of bulk nanostructured materials.
Adv Eng Mater (2007) 9:527-533.

[16] Gubicza J, Chinh NQ, Horita Z and Langdon TG
Effect of Mg addition on microstructure and mechanical properties of aluminum.
Mater Sci Eng A (2004) 387-389:55-59.

[17] Richert M, Liu Q and Hansen N
Microstructural evolution over a large strain range in aluminium deformed by cyclic extrusion compression.
Mater Sci Eng A (1999) 260: 275-283.

[18] Sitdikov O, Sakai T, Goloborodko A, Miura H and Kaibyshev R
Effect of pass strain on grain refinement in 7475 Al alloy during hot multidirectional forging.
Mater Trans (2004) 45:2232-2238.

[19] Varyutkhin VN, Beygelzimer Y, Synkov S and Orlov D
Application of twist extrusion.
Mater Sci For (2006) 503-504:335-340.

[20] Zhilyaev AP, Nurislamova GV, Kim BK, Baro MD, Szpunar JA and Langdon TG
Experimental parameters influencing grain refinement and microstructural evolution during high-pressure torsion.
Acta Mater (2003) 51:753-765.

[21] Valiev RZ, Kaibyshev OA, Kuznetsov RI, Musalimov R and Tsenev NK
The low-temperature superplasticity of metallic materials.
Doklady AN SSSR (1988) 301:864-866.

[22] Zhilyaev AP and Langdon TG
Using high-pressure torsion for metal processing: fundamentals and applications.
Prog Mater Sci (2008) 53:893-979.

[23] Valiev RZ, Krasiinikov NA and Tsenev NK
Plastic deformation of alloys with submicron-grained structure.
Mater Sci Eng A (1991)137:35-40.

[24] Segal VM
Materials processing by simple shear.
Mater Sci Eng A (1995)197:157-164.

[25] Valiev RZ and Langdon TG
Principles of equal-channel angular pressing as a processing tool for grain refinement.
Prog Mater Sci (2006) 51:881-981.

[26] Saito Y, Tsuji N, Utsunomiya H, Sakai T and Hong RG
Ultra-fine grained bulk aluminum produced by accumulative roll bonding (ARB) process.
Scripta Mater (1998) 39:1221-1227.

[27] Tsuji N, Saito Y, Lee SH and Minamino Y
ARB (accumulative roll-bonding) and other new techniques to produce bulk ultrafine grained materials.
Adv Eng Mater (2003) 5:338-344.

[28] Likhachev VA, Myshlyaev MM and Olevskii SS
Superplasticity and structure of aluminium.
Acta Meter (1974) 22: 829-834.

[29] Ryan ND, Mcqueen HJ and Jonas JJ (1983)
The deformation behavior of types 304, 316, and 317 austenitic stainless steels during hot torsion.
Can Metall Q 22: 369-378.

[30] Mcqueen HJ, Spigerelli S and Kassner ME
Hot deformation and processing of aluminum alloys.
Taylor & Francis Group, LLC (2011) 59.

Chapter 2 Effects of deformation conditions on microstructure evolution in commercial purity aluminum heavily deformed by torsion

2.1 Introduction

Severe plastic deformation (SPD) has been successfully used for producing bulk ultrafine-grained (UFG) metallic materials with grain sizes smaller than 1 μm [1]. Several SPD techniques are now available for introducing high strains into bulk materials, including cyclic extrusion compression (CEC) [2], high pressure torsion (HPT) [3], equal channel angular pressing (ECAP) [4,5], and accumulative roll bonding (ARB) [6]. The formation mechanism of UFG structures is understood in terms of *grain subdivision*, where deformation-induced boundaries subdivide the original crystals [7-11]. It has been also known that a certain amount of strain is necessary to obtain ultrafine grains with large misorientations [12]. On the other hand, the effects of other deformation conditions, i.e., strain rate and temperature, on the formation of ultrafine grained structures have not yet been systematically understood. This is primarily because most of the SPD processes mentioned above are discontinuous "batch" processes in which it is difficult to carry out ultrahigh strain deformation at a constant strain rate and temperature continuously. As mentioned in **Chapter 1**, torsion deformation could be a promising process to clarify the influence of deformation conditions on microstructure and mechanical behavior in ultrafine grained materials, in which heating rate, deformation temperature, imposed strain and strain rate can be accurately controlled [13].

During last decades, the evolutions of microstructure and the mechanical behavior of aluminum deformed by torsion at elevated temperatures have been studied [14-16].

All of the investigations found that the microstructural development and mechanical behavior in aluminum during hot torsion consist of the complex dynamic restoration mechanisms. It has been also reported that the grain size and morphology of the grain were strongly affected by the deformation parameters such as strain, strain rate and deformation temperature. Those deformation parameters are found to be the crucial factors to determine microstructures in aluminum. Although many researchers have studied the effect of deformation conditions on microstructure and mechanical properties in aluminum, the most of these investigations were focused on the mechanical and microstructural properties of aluminum deformed at high temperatures ($> 0.4\ T_m$, where T_m is the melting point temperature of aluminum alloy) and at low strain rate ($< 10^{-2}\ s^{-1}$). So far, the complete and clear view on the deformation mechanism of aluminum is not available for the wide ranges of equivalent strains, deformation temperatures and strain rates. In the present study, the author systematically investigates the microstructural evolution in aluminum deformed under a wide ranges of equivalent strain, deformation temperature and stain rate by torsion deformation.

2.2 Experimental procedure

2.2.1 Effect of strain on microstructural evolution

Commercial purity aluminum (1100Al) bars were used in this study. The chemical composition of the material is shown in **Table 2.1**.

Table 2.1: Chemical composition of the 1100Al studied (mass%).

Si	Fe	Cu	Mn	Zn	Ti	Al
0.09	0.61	0.11	0.01	0.02	0.02	Bal.

The starting bars were machined into torsion specimens with dimensions of 4 mm in gage length and 8 mm in diameter (**Fig. 2.1 (a)**), and torsion deformation was applied to achieve high strain deformation. The specimens were deformed in torsion at room temperature by rotations of 0.25, 0.50, 1.00, 1.50 and 1.60, corresponding to the equivalent strains of 0.91, 1.81, 3.63, 5.44 and 5.85 at the specimen surface, respectively. The rotation speed was 1.66×10^{-5} rotation per minute so that the strain rate at the specimen surface was 10^{-3} s^{-1}.

The shear strain (γ) and shear stress (τ) at the surface of the specimen were computed from the torsion results using the classical equations shown below [15,17,18]:

$$\gamma = \frac{2\pi RN}{L} \tag{2.1}$$

$$\tau = \frac{M}{2\pi R^3}(3 + k + m) \tag{2.2}$$

where R is the radius, L is the gage length, N is the number of rotations, M is the torsion moment (torque) (M is recorded during the torsion deformation), k is the strain-hardening coefficient (k was taken as zero, which is valid merely at the peak torque and in steady-state flow), m is the strain rate sensitivity described by $\{logM/log\dot{\varepsilon}\}_T$, $\dot{\varepsilon}$ is the strain rate and T is the deformation temperature.

The equivalent strain (ε_{eq}) and equivalent stress (σ) in torsion were computed by the use of von Mises equations [19]:

$$\varepsilon_{eq} = \frac{\gamma}{\sqrt{3}} \tag{2.3}$$

$$\sigma = \frac{\tau}{\sqrt{3}} \tag{2.4}$$

2.2.2 Effects of deformation temperature and strain rate on microstructural evolution

In order to understand the effects of deformation temperature and strain rate on the microstructural evolution in the commercial purity aluminum, torsion deformations were conducted at five different temperatures and four different strain rates. The torsion deformation procedure is schematically shown in **Fig. 2.2**. The torsion specimens were heated by an induction coil at a heating rate of 0.5 $°Cs^{-1}$ to the deformation temperatures, which ranged from 100 to 400 °C, and kept for 600 s to stabilize the temperature of the specimen. After that, torsion deformation was carried out to various equivalent strains under a constant strain rate in the range of 10^{-2} s^{-1} to 10^{2} s^{-1}. Then the deformed specimens were immediately quenched with water injection to prevent microstructure modifications. The cooling rate during water quenching was recorded to be approximately 200 °C s^{-1}. On the other hand, the torsion deformation was also performed at room temperature to various equivalent strains at various strain rates. The stress and stain data were obtained from the torque and angular displacement data recorded during torsion deformation.

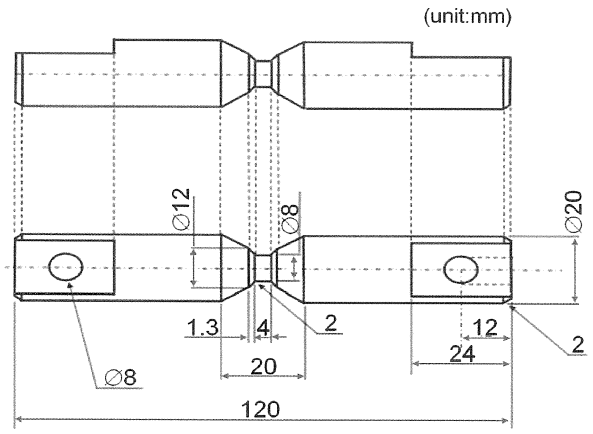

Fig. 2.1 Schematic illustrations of the dimension and shape of torsion specimen

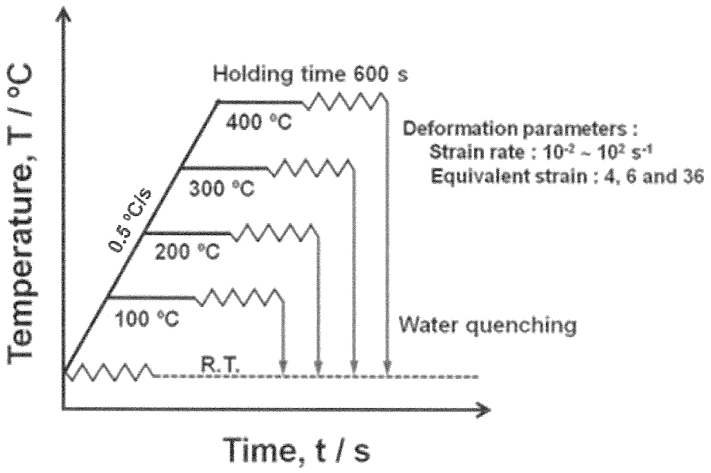

Fig. 2.2 Schematic illustration showing the heat patterns in torsion deformation.

2.2.3 Characterizations

2.2.3.1 Microstructure observation

Microstructures of the torsion deformed specimens were characterized by electron back-scattering diffraction (EBSD) measurement and transmission electron microscopy (TEM). The EBSD scans were carried out on the longitudinal section at r = 0.9R (R: radius of specimen) position from the center of the specimen, shown in **Fig. 2.3 (a)**, and at different locations on the transverse sections perpendicular to the torsion axis to examine homogeneity of deformation microstructure. Specimens for EBSD analysis were prepared by mechanical polishing, followed by electropolishing at -30 °C at a voltage of 12 V in a solution of 30 vol.% nitric acid (HNO_3) and 70 vol.% methanol (CH_3OH). EBSD observation was performed in a field-emission scanning electron microscope (FE-SEM, Phillips FEI XL30S FEG) at an accelerating voltage of 15 kV. For TEM analysis, thin-foil specimens were prepared by twin-jet electopolishing under the same temperature and solution as those for the EBSD observation. TEM

observations were performed in a JEOL-2000EX TEM microscope with a double-tile stage at an operating voltage of 200 kV.

2.2.3.2 Hardness test

Hardness tests were conducted for the torsion deformed specimens using Shimadzu micro-hardness tester equipped with Vickers indenter. Load of 1 kg and dwell time of 10 s were used in all tests. Hardness measurements were carried out at various radial positions on the polished surfaces of transverse sections of the torsion deformed specimens, as shown schematically in **Fig. 2.3 (b)**.

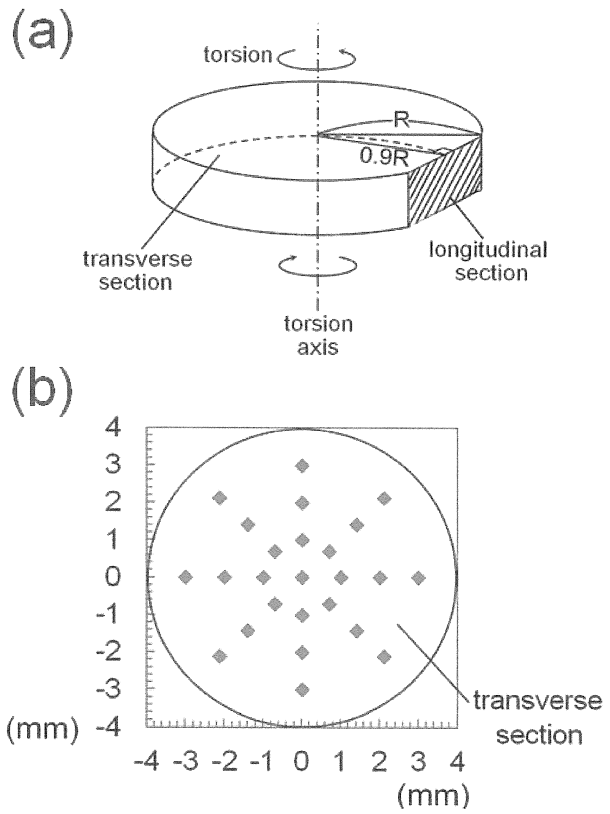

Fig. 2.3 Schematic illustrations of (a) the longitudinal section for indicating the plane for microstructure observations, and (b) the positions of hardness measurement on the transverse section.

2.3 Effect of imposed strain on microstructure evolution

2.3.1 Microstructure evolution during torsion deformation

Figure 2.4 shows (grain) boundary maps obtained from EBSD measurement on longitudinal sections of the starting material and the specimens torsion deformed to various equivalent strains (ε_{eq} = 0.82 - 5.27). These equivalent strains were calculated at the observation position (0.9R). In the figures, the black and gray lines represent high-angle grain boundaries ($\theta \geq 15°$, θ: misorientation) and low-angle grain boundaries ($2° \leq \theta < 15°$), respectively. Boundaries having misorientations below 2° are not included in the analysis in order to remove the inaccuracy in EBSD measurement and analysis. It is clearly seen in **Fig. 2.4 (a)** that the starting material exhibits a fully recrystallized microstructure with the average grain size of 23 μm. In cases of the imposed equivalent strains below 2, low-angle boundaries are mainly observed along the shear direction, (**Fig. 2.4 (b, c)**). With increasing torsion strain, fine grains surrounded by high angle grain boundaries are generated. However, a large number of grains with low-angle boundaries remain in the structure after ε_{eq} = 3.27 (**Fig. 2.4 (d)**). By increasing equivalent strain to 4.90, the amount of fine grains with high angle boundaries is increased (**Fig. 2.4 (e)**). The specimen deformed to an equivalent strain of 5.27 exhibits finer and more equiaxed grains. When all boundaries are taken into account, the mean grain size is 0.32 μm. Most of those fine grains are surrounded by high-angle grain boundaries (**Fig. 2.4 (f)**).

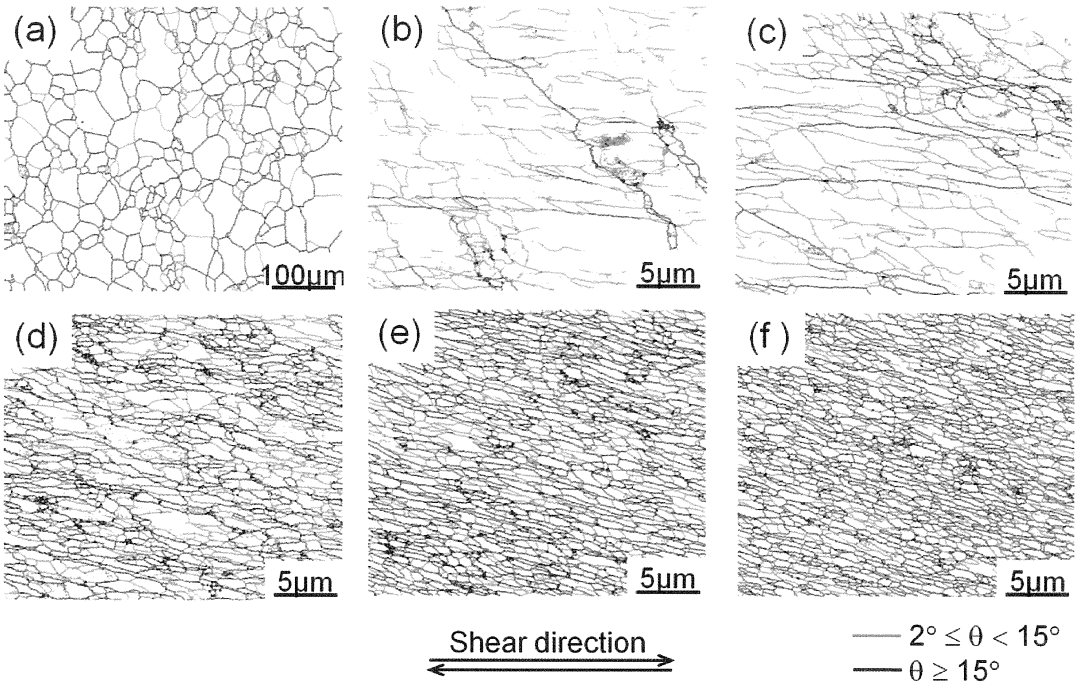

Fig. 2.4 EBSD boundary maps of the specimens torsion deformed to various equivalent strains at RT: (a) undeformed material, (b) ε_{eq} = 0.82, (c) ε_{eq} = 1.63, (d) ε_{eq} = 3.27, (e) ε_{eq} = 4.90, and (f) ε_{eq} = 5.27. Observed on the longitudinal sections at 0.9R.

The average grain size and fraction of high angle boundaries obtained from the EBSD data are summarized in **Table 2.2**, where D_{All} is the average (sub)grain size obtained from all boundaries having misorientation above 2° and D_{HAGB} is the mean grain size obtained from high angle grain boundaries ($\theta \geq 15°$). Fractions of high-angle boundaries (F^{HAGB}) are also summarized in the table. The main finding is the evolution of ultrafine grained microstructure in the 1100Al with increasing torsion strain. The grain size decreases and the fraction of high angle grain boundaries increases with increasing equivalent strain. Similar observations have been reported in several materials severely deformed by ARB [20], ECAP [4, 21] and HPT [22, 23] processes. It has been considered that the formation of ultrafine grained microstructures during high plastic deformation can be understood in terms of *grain subdivision*. *Grain subdivision*

[10,11] is the process in which geometrically necessary boundaries (GNBs) and incidental dislocation boundaries (IDBs) induced by plastic deformation subdivide the original crystals. Based on the microstructural results, the features of the ultrafine grain formation during torsion deformation process can be described as follows: at low strain ($\varepsilon_{eq} < 2$), the original grains are deformed and start to be subdivided into subgrains with low-angle misorientation, and those subgrains are elongated in the direction nearly parallel to the shear direction, as shown in **Fig. 2.4 (b, c)**. New ultrafine grains with high-angle boundaries are generated at medium strains ($2 < \varepsilon_{eq} < 4$). At this stage a number of low-angle boundaries still remain in the structure as shown in **Fig. 2.4 (d)**. An ultrafine grain structure with the fraction of high-angle grain boundary above 0.65 is obtained at high strains ($\varepsilon_{eq} \geq 4.9$). More equiaxed ultrafine grains (~ 0.32 μm) are homogeneously formed in the microstructure at ultrahigh strain ($\varepsilon_{eq} = 5.27$) as seen in **Fig. 2.4 (f)**. The present results agree well with that reported by Hansen et al. [10] who demonstrated that elongated deformation structures of pure aluminum formed by conventional rolling changed from oriented structures into more equiaxed structures at high strain. Such a morphological transition has been also observed in processes where deformation involves a significant shear component [10], or when the deformation direction is changed [11].

Table 2.2: Summary of the microstructural parameters of the 1100Al specimens torsion deformed to various equivalent strains at RT, where D_{All} is the average grain size with having misorientation above 2 °, and D_{HAGB} is the mean grain size obtained from high angle grain boundaries ($\theta \geq 15°$). The parameters were measured using EBSD data measured on longitudinal sections shown in **Fig. 2.1**.

Equivalent strain (at $0.9R$)	Average grain size (μm)		Fraction of high angle boundaries, F^{HAGB}
	D_{All}	D_{HAGB}	
0	23.4	28.0	0.76
0.82	1.94	6.29	0.18
1.63	0.56	1.86	0.35
3.27	0.40	0.46	0.55
4.90	0.35	0.36	0.67
5.27	0.32	0.33	0.76

2.3.2 Comparison between torsion deformation and ARB

Figure 2.5 shows a comparison between torsion deformation and ARB process by plotting the average grain size (D_{All}) and fraction of high angle boundaries (F^{HAGB}) in the 1100Al deformed by two processes as a function of equivalent strain. The ARB data were taken from a previous report by Kamikawa [24]. It is obvious in **Fig. 2.5 (a)** that the grain size of the specimens deformed by torsion exhibits the similar trend as that deformed by ARB. Grain size decreases with increasing strain. However, observing the microstructural change in **Fig. 2.5 (a)** carefully (see the insert), it is found that at similar strains the grain sizes of the specimen ARB processed are finer than those of the torsion deformed specimens. At the same time, it is also observed that the increasing rate of fraction of high-angle grain boundary in the ARB processed specimens is greater than that in the torsion deformed specimens. In other words, the evolution of the ultrafine grained structures in the 1100Al was faster in the ARB than that in the torsion. A

similar observation has been reported by Zhilyaev et al. [25] who demonstrated that different deformation processes resulted in different grain sizes in high purity nickel. Probably this difference is caused by the difference in strain path. In the torsion deformation, monotonic simple shear is the dominant deformation mode, while the deformation in the ARB process is more complicated. Because the corresponding ARB process was carried out without lubrication [24], redundant shear strains were applied at the subsurface regions of the sheet due to large friction between rolls and the sheet, as well as the plane strain compression normal to the rolling plane. Half of the surface regions come to the center in the ARB process, making the strain path of each region complicated.

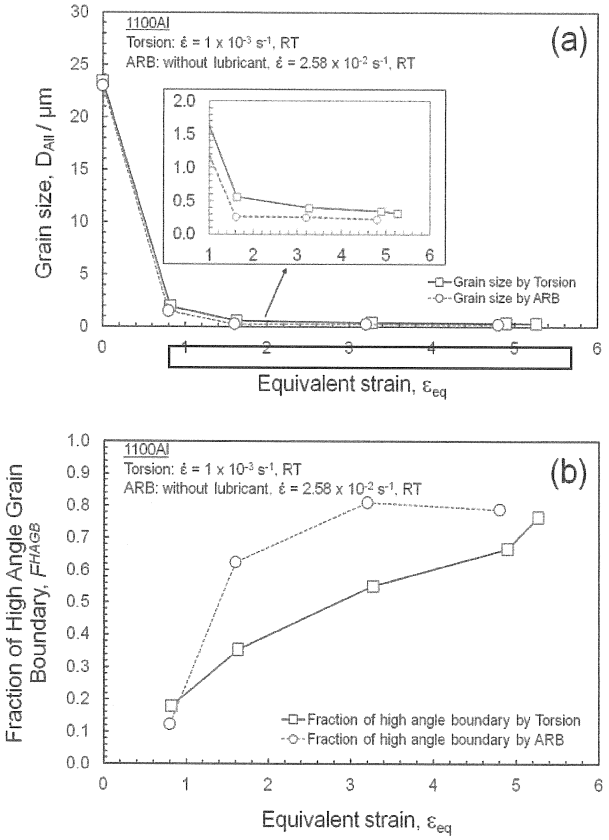

Fig. 2.5 (a) Average grain size (D_{All}) and (b) fraction of high-angle boundaries (F^{HAGB}) in the 1100Al deformed by torsion and ARB [24] at RT, plotted as a function of equivalent strain.

2.3.3 Microhardness

Figure 2.6 shows the hardness values at various radial positions in the torsion specimens after different rotation from 0.5 to 1.6. The hardness measurements were carried out on the transverse sections perpendicular to the torsion axis, as was shown in **Fig. 2.1**. The lower broken line corresponds to the hardness level of the unprocessed specimen, 27.4 Hv. The main results presented in **Fig. 2.6** are summarized as follows. First, the hardness values increase with increasing applied torsion rotation. Second, the values of hardness increase with increasing the distance from the center of the specimen. This is attributed to the difference in strain along the radial position in torsion deformation, as is expressed in **Eq. (2.1)**. According to **Eq. (2.1)**, the shear strain at the center is ideally zero and it increases linearly with approaching to the surface. Thus, the microstructure along the radius should be inhomogeneous, as is shown later (**Fig. 2.7**). The hardness value near the center reveals strain hardening, although the strain at the centre should be ideally zero. This may be attributed to the compressive deformation happening in the torsion process. The increase of the hardness with plastic strain is caused by strain hardening and grain reinfinement strengthening.

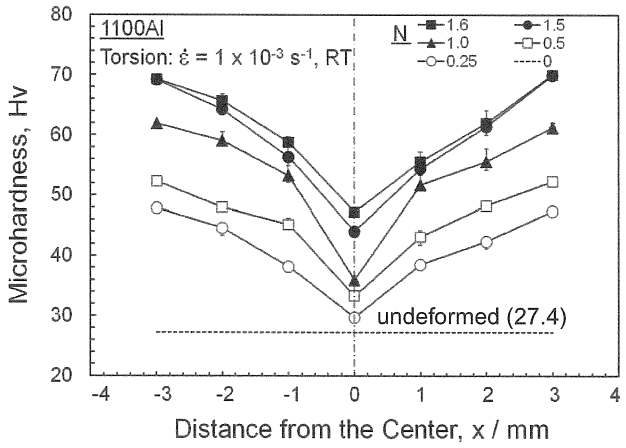

Fig. 2.6 Average microhardness values at various radial positions in the 1100Al specimens torsion deformed to different rotations (N) at RT.

Figure 2.7 shows the EBSD grain boundary maps at different radial positions in the 1100Al specimen torsion deformed by 1.5 rotations: (a) at the center of the sample (r = 0), (b) r = 0.2*R*, (c) r = 0.5*R* and (d) r = 0.9*R*, where *R* is the radius of the sample (4 mm). Corresponding equivalent strains are 0, 1.09, 2.72, and 4.90, respectively. The results clearly show that these four areas have different microstructures. The microstructure at the center of the specimen, of which the shear strain should be ideally zero, shows coarse grains with less low-angle boundaries inside (**Fig. 2.7 (a)**). In **Fig. 2.7 (b)** corresponding to r = 0.2*R* (ε_{eq} = 1.09), new grains with smaller grain sizes are partly formed, but most of the regions exhibit low-angle boundaries (deformation structures). Grain size (D_{All}) decreases with increasing the distance from the center to the edge of the specimen, i.e., with increasing equivalent strain (**Fig. 2.7 (c, d)**). The mean grain sizes (D_{All}) at different positions from 0 to 0.9R are 17.2 μm, 2.0 μm, 0.99 μm and 0.62 μm, respectively. The fractions of high-angle boundaries at different positions are 0.85, 0.18, 0.30 and 0.53, respectively. The fraction of high-angle boundaries rapidly decreases from the center to 0.2R due to the introduction of deformation structures (**Fig. 2.7 (b)**), and then it significantly increases with increasing distance from the specimen axis.

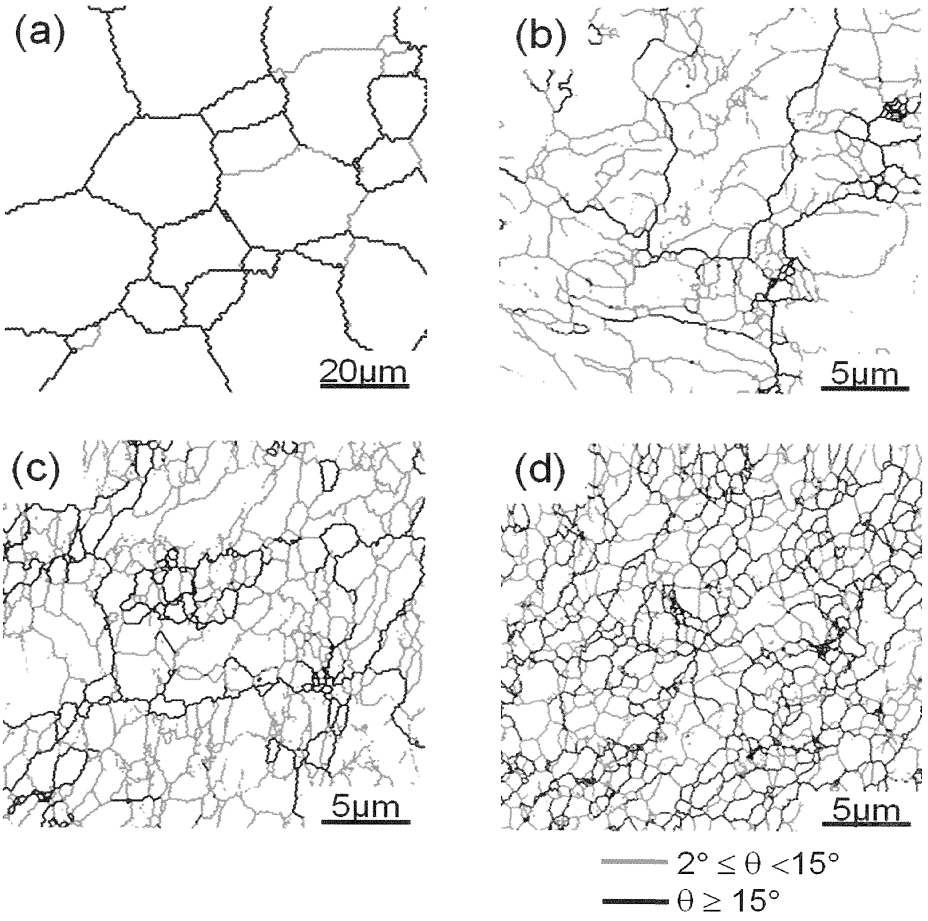

Fig. 2.7 EBSD grain boundary maps at different radial positions of the 1100Al specimens torsion deformed by 1.5 rotations at RT. (a) At the center of the sample (r = 0), (b) r = 0.2*R*, (c) r = 0.5*R* and (d) r = 0.9*R*, where *R* is the radius of the sample (4.0 mm). The corresponding equivalent strains (ε_{eq}) are (a) 0, (b) 1.09, (c) 2.72, and (d) 4.90, respectively.

It was found that at the same strain the fraction of high-angle boundary observed on the transverse-section **(Fig. 2.7)** was lower than that observed on longitudinal-section **(Fig. 2.5 (b))**. The discrepancy might be attributed to the difference in strain rate along the radial position in torsion deformation. The strain and strain rate increase with approaching to the edge of the specimen, so that the microstructures observed on the transverse-section were those formed under lower strain rate even at the same level of strain. On the other hand, it should be noted that even at the same edge position

(0.9R), the grain size observed on the transverse-section was smaller than that observed on the longitudinal section. This indicates that three-dimensional morphology of the ultrafine grains formed by torsion is not equiaxed.

The hardness data in **Fig. 2.6** are replotted as a function of equivalent strain in **Fig. 2.8**. It can be seen that the hardness continuously increases with increasing equivalent strain, so that the hardness corresponds well with an imposed strain. We have also found the scattering of hardness values at the center regions; the hardness value obviously increases with increasing deformation rotation. By the way, a homogeneous microstructure has been reported in Al processed to high strain by HPT [26]. The deformation in HPT is fundamentally similar to the torsion deformation, i.e., monotonic simple shear. This difference is presumably attributed to the fact that the previous study in HTP was carried out up to extremely high shear strain of 184, which corresponded to total equivalent strain of 106. At the same time, there are several reports showing inhomogeneous hardness distribution after HPT process [27-29]. Vorhauer and Pippan [29] have found that an inhomogeneous microstructure appeared in an austenitic steel deformed to ultrahigh strain (ε_{eq} = 324) by HPT [29]. This difference may suggest that the strain necessary for obtaining homogeneous microstructure depends on the kind of materials.

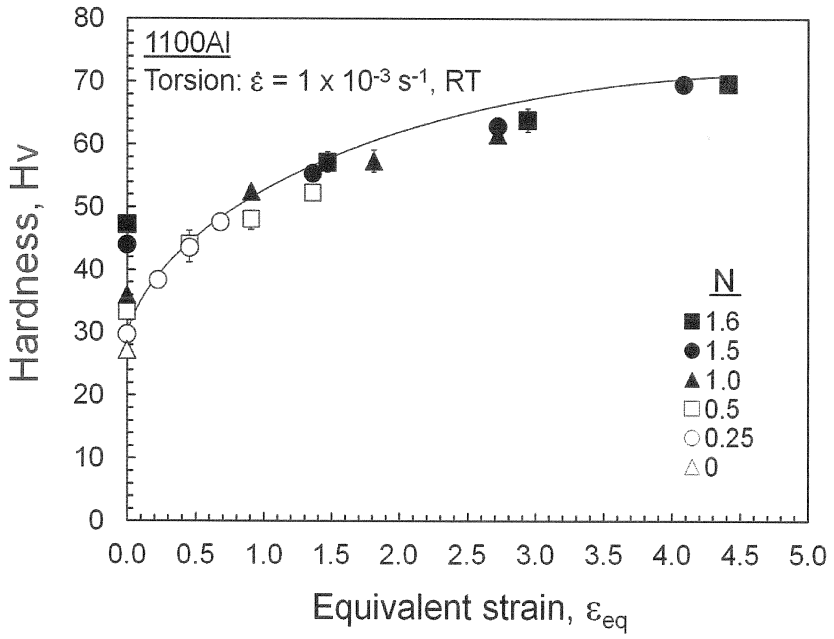

Fig. 2.8 Average microhardness values at various radial positions of the 1100Al specimens deformed to different torsion rotations (*N*) at RT, plotted as a function of equivalent strain.

It can be concluded from the present investigation that torsion deformation worked as a kind of severe plastic deformation for fabricating ultrafine grained microstructures. Though the microstructures were heterogeneous depending on the radial positions, the microstructural parameters were well understood in terms of equivalent strain. The results indicated that torsion deformation was useful to investigate the effect of deformation conditions on the ultrafine grain formation, which will be studied in the following sections.

2.3.4 Summary

In this section (2.3), the effect of strain on microstructure and hardness of a commercial purity (1100Al) deformed by torsion at RT has been studied. The main results are summarized as follows:

1. The grain size decreased and fraction of high-angle boundaries increased with increasing plastic strain in torsion deformation. The grain size of 0.32 μm and the high-angle boundary fraction of 0.76 were achieved after equivalent strain of 5.27. It indicated that the torsion deformation worked as a kind of severe plastic deformation. The torsion would make it possible to study ultra-high strain deformation under controlled temperature and strain rate.

2. The grain size and misoreintation angle of the 1100 aluminum deformed by torsion had the same trend as those heavily deformed by ARB. However, the ARB process showed higher efficiency in producing ultrafine grained microstructure, than torsion deformation. This was probably because the strain path in torsion was much simpler than that in ARB.

3. The hardness values increased with increasing the equivalent strain and the radial position in the sample. Although the hardness and microstructure were heterogeneous on the transverse sections, they showed a good correlation with the equivalent strain imposed at each radial position.

2.4 Effects of strain rate and deformation temperature on microstructural evolution

2.4.1 Stress-strain behavior

The stress-strain curves of the commercial purity aluminum torsion deformed at various temperatures (RT to 400 °C) and strain rates (10^{-2} s^{-1} to 10^{2} s^{-1}) are shown in **Fig. 2.9**. It is found that at a constant strain rate, flow stress increases with decreasing deformation temperature. To the contrary, at a certain temperature, the flow stress increases with increasing strain rate at temperatures ranging from 100 °C to 400 °C, except at room temperature. The flow stress of the specimen deformed at room temperature increases slightly with increasing strain rate up to the strain rate of 10^{-1} s^{-1}. Beyond the strain rate of 10^{-1} s^{-1}, the flow stress decreases significantly with increase in strain rate. The decrease in stress with increasing strain rate at RT may be due to the temperature rise (adiabatic heating) caused by plastic deformation, which results in decreasing flow stress.

The specimens deformed under these deformation conditions exhibited three typical stress-strain curves, depending on the deformation parameters. The specimens deformed at low temperatures (RT-200 °C) illustrated two types of stress-strain curves. The first type was simple work hardening, i.e., the flow stress increased monotonously with increasing strain until the maximum stress followed by failure. The second type was dynamic recovery. That is, the flow stress increased with raising strain to the maximum stress. After the maximum stress, the stress-strain curve exhibited steady-state flow stress. For the specimens deformed at high temperatures ($T \geq 300$ °C) and at low strain rates ($\dot{\varepsilon} < 10^{0}$ s^{-1}), the flow stress raises with increasing strain to the peak stress followed by stress softening and steady-state flow stress, which is the third type.

These results revealed that the flow stresses, and the shapes of the flow curves were strongly dependent on deformation temperature and strain rate.

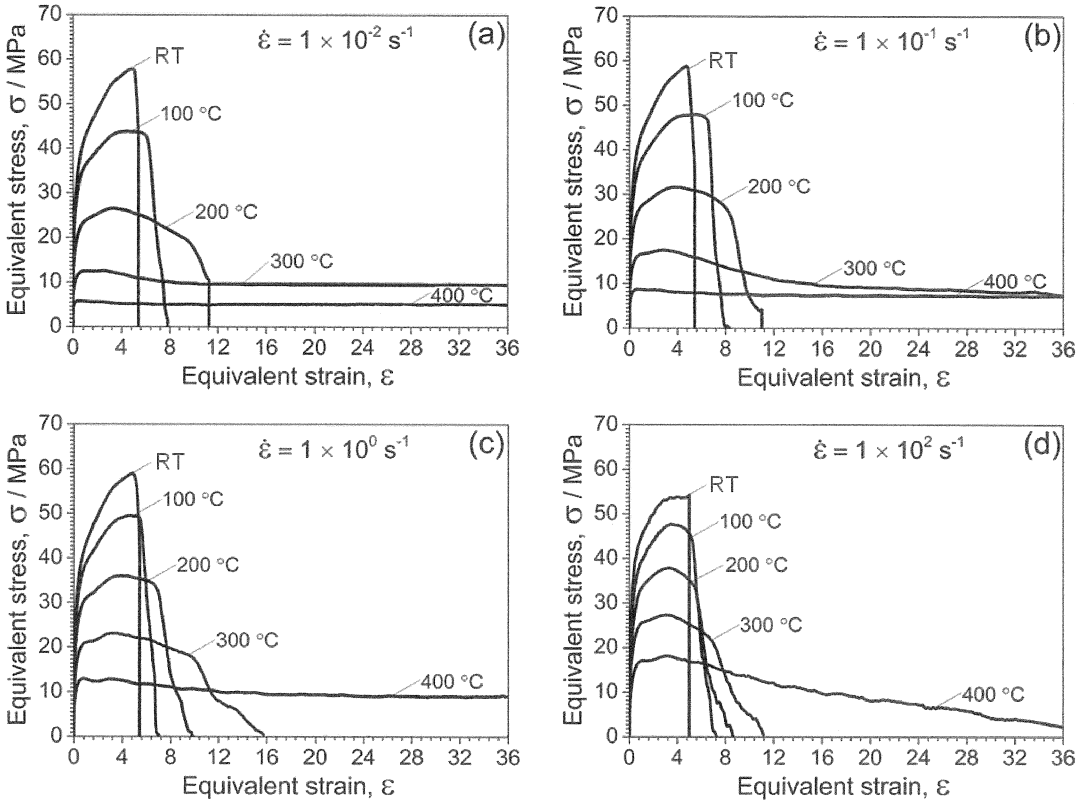

Fig. 2.9 Stress-strain curves of the specimens torsion deformed at various deformation temperatures from RT to 400 °C at various strain rates (a) $\dot{\varepsilon} = 10^{-2}$ s^{-1}, (b) $\dot{\varepsilon} = 10^{-1}$ s^{-1}, (c) $\dot{\varepsilon} = 10^{0}$ s^{-1} and (d) $\dot{\varepsilon} = 10^{2}$ s^{-1}.

Generally, the dependence of the flow stress on deformation temperature and strain rate can be represented by the Arrhenius-type equation using the Zener-Hollomon parameter, as shown below:

$$Z = A\sigma_M^{\,n} \tag{2.5}$$

$$Z = A'\exp(\beta\cdot\sigma_M)^{\,n'} \tag{2.6}$$

$$Z = A''[\sinh(\alpha\cdot\sigma_M)]^{\,n''} \tag{2.7}$$

$$Z = \dot{\varepsilon} \exp\left(\frac{Q}{RT}\right) \tag{2.8}$$

where Z is the Zener-Hollomon parameter, σ_M is the maximum stress, n, n' and n'' are the stress exponent, A, A', A'', α and β are materials constant, R is the gas constant, T is absolute temperature, and Q is an apparent activation energy for high temperature deformation. These equations were originally developed for creep [18, 30]. However, they can be also utilized for high strain rates at wide ranges of temperatures in ultrafine grained materials [31, 32]. The equations (2.5) to (2.7) are referred as power-law, exponential and hyperbolic-sine equations, respectively [33]. The power-law equation is suitable for the low stress conditions, while the exponential equation is appropriate for the high stress conditions. The hyperbolic-sine equation is applicable for both cases. Since the specimens deformed under the present experimental deformation conditions exhibited low flow stress (see **Fig. 2.9**), the power law is applied. In the present study, the apparent activation energy of 156 kJ mol^{-1} is taken for calculating Z from the result of deformation in commercial purity aluminum reported by Jonas et al. [30]. Jonas and his coworker have used this value to correlate both creep and hot-working data in commercial purity aluminum [14]. This Q value is close to the activation energy for self-diffusion in aluminum (142 kJ mol^{-1}) [18].

The maximum stresses obtained from the stress-strain curves in **Fig. 2.9** are plotted as a function of Z parameter in the log-log scale in **Fig. 2.10 (a)**. It is found that the maximum stress decreases with decreasing Zener-Hollomon (Z) parameter. The relationship between stress and Z parameters can be approximated by two linear lines as show in **Fig. 2.10 (a)**. The change in the slope of σ_M-Z plot occurs at a critical Z value (Z_c) of 2.47×10^{15} s^{-1}. Some researchers have claimed that a transition of the slope is

resulted from the changes in deformation mechanisms [32, 35]. However, the deviation of data points from the linear line in the power-law at high Z region (i.e. high stress) might be also attributed to the limitation of power-law expression (power-law breakdown) [36]. Therefore, in order to clarify this, the hyperbolic-sine equation is applied. The same Q value applies in **Eq. (2.5)** and a material constant value (α) of 0.0043 MPa^{-1} [30] are used as fitting parameters in hyperbolic-sine equation. The sinh ($\alpha \cdot \sigma_M$) was calculated using **Eq. (2.7)** and plotted versus Z parameter in **Fig. 2.10 (b)**. It was found that the hyperbolic-sine law shows the similar results with the power law, indicating that the power law is valid for this experimental data. In addition, Sherby and Burke have systematically investigated the creep behavior of pure metals and alloys, and showed that power law breakdown occurs at a normalized strain rate of $\dot{\varepsilon}/D \cong 10^{13}$ m^{-2}, where D is the diffusion coefficient [35, 37]. The value of D can be calculated using the following equation [35]:

$$D = 1.24 \times 10^{-4} \exp(-156/RT) \quad m^2 s^{-1} \tag{2.9}$$

It should be noted here that the deviation of data points occurs approximately at equivalent strain rate of 10^{-2} s^{-1} and at 200 °C. It is found that the normalized equivalent strain rate at the deviation point is 1.6×10^{-7} m^{-2}. This value is significantly lower than the equivalent strain rate of power law breakdown point. These results indicate that the apparent change in slope in the σ_M-Z plot at Z_c in **Fig. 2.10 (a)** is not attributed to power law breakdown. The reasons for the transition will be discussed in the following sections based on the microstructures. The two separate regions are mentioned here as region I and II, respectively.

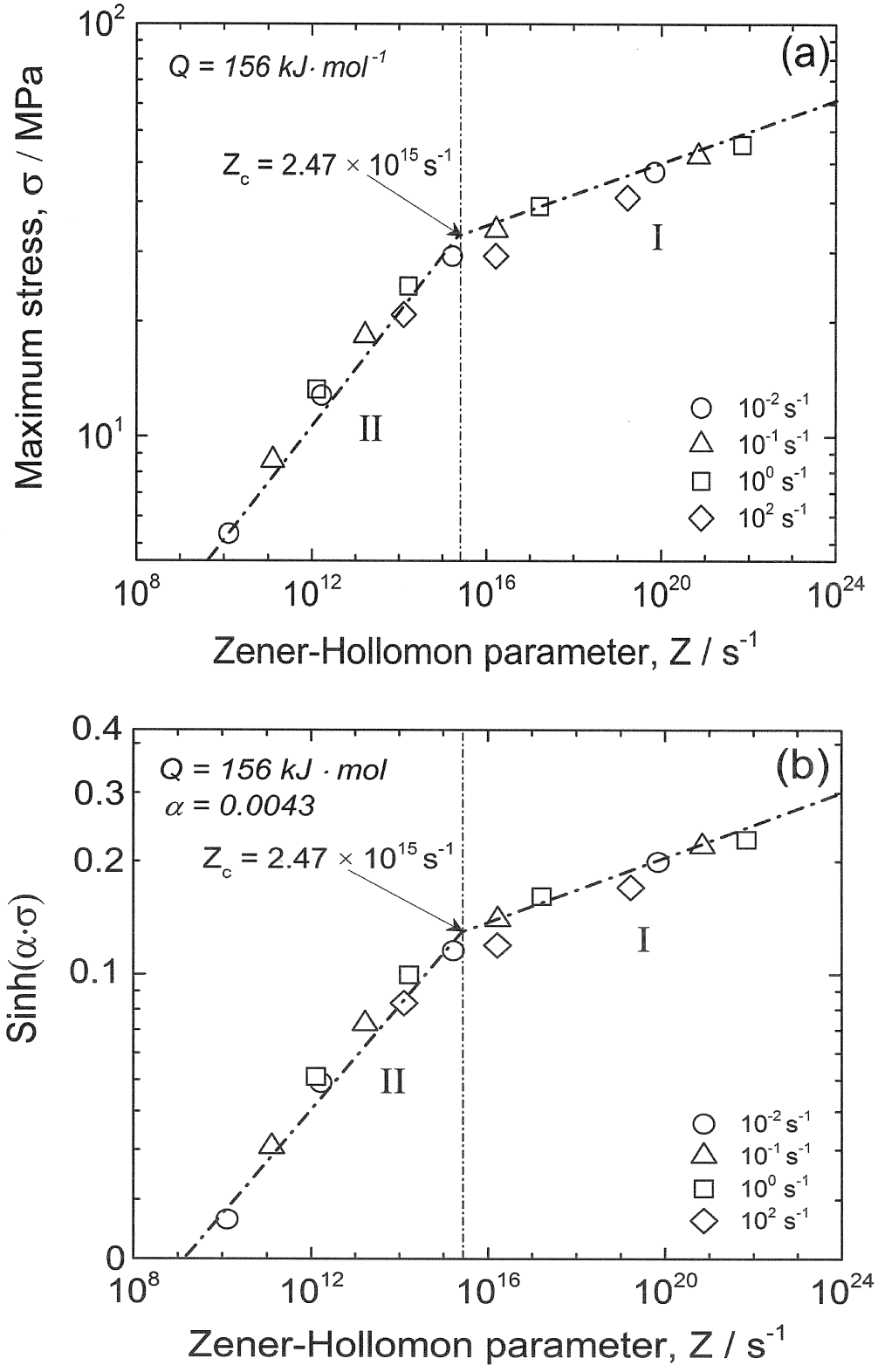

Fig. 2.10 The maximum flow stress plotted as a function of Zener-Hollomon parameters calculated by (a) power law, and (b) hyperbolic-sine equations.

The n values determined in the regions I and II using **Eq. (2.5)** are shown in **Fig. 2.11 (a)** and **(b),** respectively. These n values are used for re-calculating Q values (apparent activation energy for high temperature deformation) in region I and II using **Eq.2.5**. The Q values evaluated are 128 and 164 kJ mol^{-1} in the region I and II, respectively. The evaluated n, Q and Z parameters are also summarized in **Table 2.3**. In this table, the shaded area is indicated the deformation conditions of the region I.

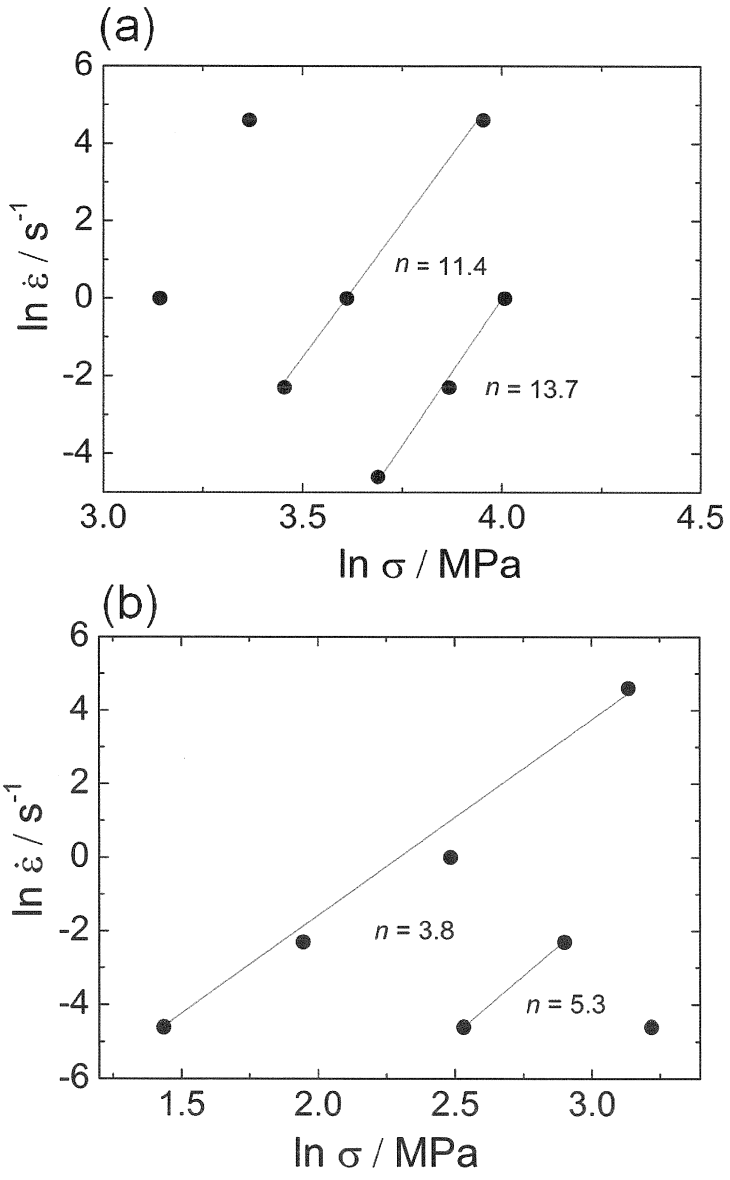

Fig. 2.11 The evaluated n values in (a) region I and (b) region II.

Table 2.3: Summary of deformation variables (strain rate and deformation temperature), the calculated Z, n and Q values.

Strain rate, $\dot{\varepsilon}$ / s^{-1}	Zener-Hollomon parameter, Z / s^{-1}					Q	n
	RT	100 °C	200 °C	300 °C	400 °C		
10^{-2}	2.21×10^{25}	7.03×10^{19}	1.69×10^{15}	1.67×10^{12}	1.28×10^{10}	128	12.5
10^{-1}	2.21×10^{26}	7.03×10^{20}	1.69×10^{16}	1.67×10^{13}	1.28×10^{11}		
10^{0}	2.21×10^{27}	7.03×10^{21}	1.69×10^{17}	1.67×10^{14}	1.28×10^{12}	164	4.5
10^{2}	2.21×10^{29}	7.03×10^{23}	1.69×10^{19}	1.67×10^{16}	1.28×10^{14}		

2.4.2 Microstructure observation

Figures 2.12 and **2.13** show EBSD boundary maps of the commercial purity aluminum deformed under various Z conditions to the equivalent strains of 3.6 and 5.4, respectively. In the grain boundary maps, the black and red lines indicate the high-angle boundary and the low-angle boundary, respectively. **Figure 2.12 (a)-(c)** shows the deformation microstructures of the specimens deformed at high Z conditions (region I: $Z \geq Z_c$) to an equivalent strain of 3.6. In the region I, the microstructure mainly consists of the lamellar structure, which is nearly parallel to the shear direction. The grain size and the amount of high-angle grain boundaries increase gradually with decrease in Z value. Below Z_c (i.e., in region II), different structures are observed. The morphologies of the deformation structure in the specimens deformed under region II conditions are significantly different from those of the specimens processed under region I conditions, as shown in **Fig. 2.12 (d)-(f)**. In the region II, the structure comprises of equiaxed grains surrounded by high-angle boundaries. The grain size increases significantly with decreasing Z parameter. On the other hand, further increase in the equivalent strain causes no changes in the morphology, as shown in **Fig. 2.13**. At an equivalent strain of 5.6, the microstructures are similar to those found in the specimens deformed to an

equivalent strain of 3.6. The grain size increases with decreasing Z value and the grain morphology clearly transits from elongated grains to equiaxed grains at Z_c.

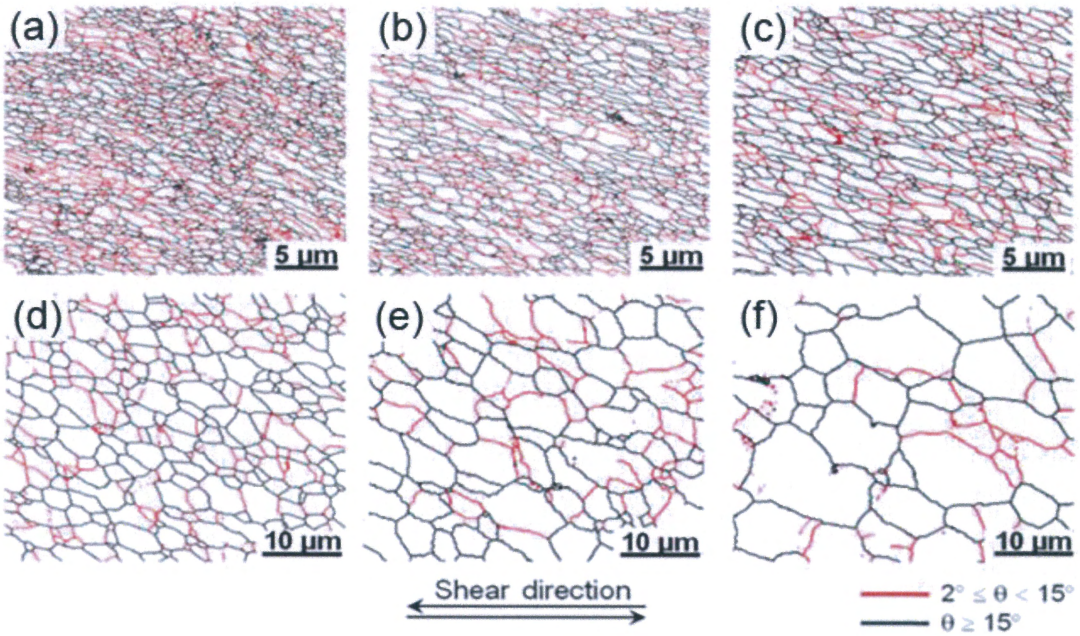

Fig. 2.12 EBSD boundary maps of the specimens torsion deformed to an equivalent strain of 3.6 under various Z conditions: (a) $Z = 2.21 \times 10^{26}$ s^{-1} (Region I), (b) $Z = 7.03 \times 10^{19}$ s^{-1} (Region I), (c) $Z = 1.69 \times 10^{16}$ s^{-1} (Region I), (d) $Z = 1.28 \times 10^{14}$ s^{-1} (Region II), (e) $Z = 1.67 \times 10^{12}$ s^{-1} (Region II), and (f) $Z = 1.28 \times 10^{10}$ s^{-1} (Region II).

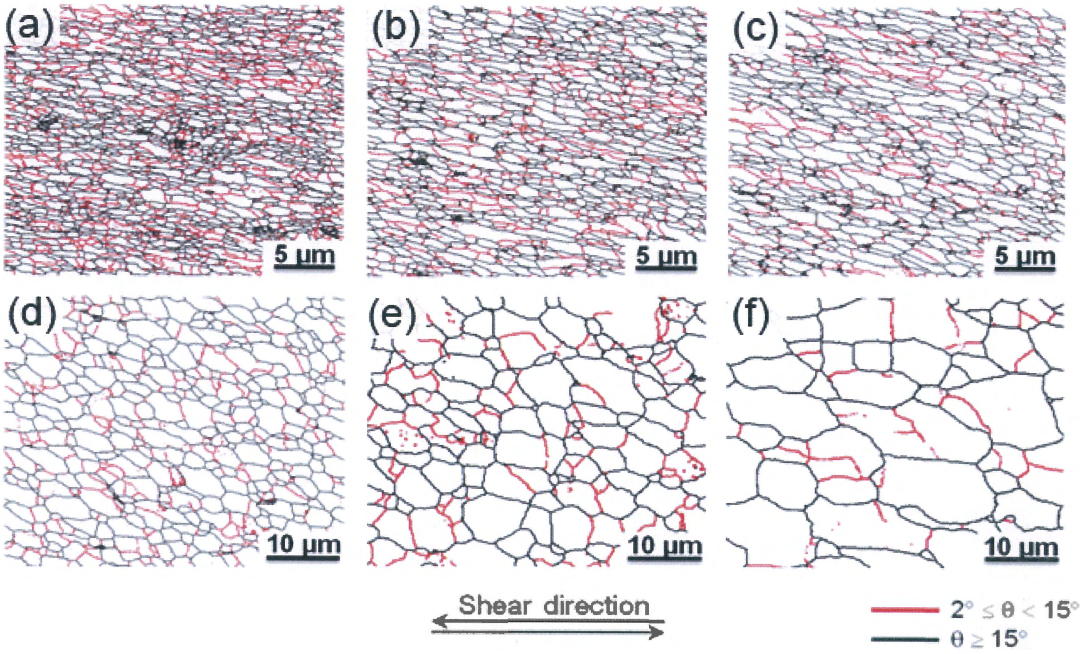

Fig. 2.13 EBSD boundary maps of the specimens torsion deformed to an equivalent strain of 5.4 under various Z conditions: (a) $Z = 2.21 \times 10^{26}$ s^{-1} (Region I), (b) $Z = 7.03 \times 10^{19}$ s^{-1} (Region I), (c) $Z = 1.69 \times 10^{16}$ s^{-1} (Region I), (d) $Z = 1.28 \times 10^{14}$ s^{-1} (Region II), (e) $Z = 1.67 \times 10^{12}$ s^{-1} (Region II), and (f) $Z = 1.28 \times 10^{10}$ s^{-1} (Region II).

In order to observe more details in microstructure, TEM observations were performed. TEM micrographs of the specimens deformed under various Z conditions are shown in **Fig. 2.14**. It is found that the microstructures of the specimens deformed under high Z conditions consist of elongated grains having large amount of dislocations as shown in **Fig. 2.14 (a)**. With decreasing Z value, the amount of dislocations decreases and cell structures are formed through dislocation annihilation and rearrangement (**Fig. 2.14 (b)**). With decreasing Z value below Z_c, the structure transforms from elongated grains to the equiaxed grains having low dislocation densities (**Fig. 2.14 (c, d)**).

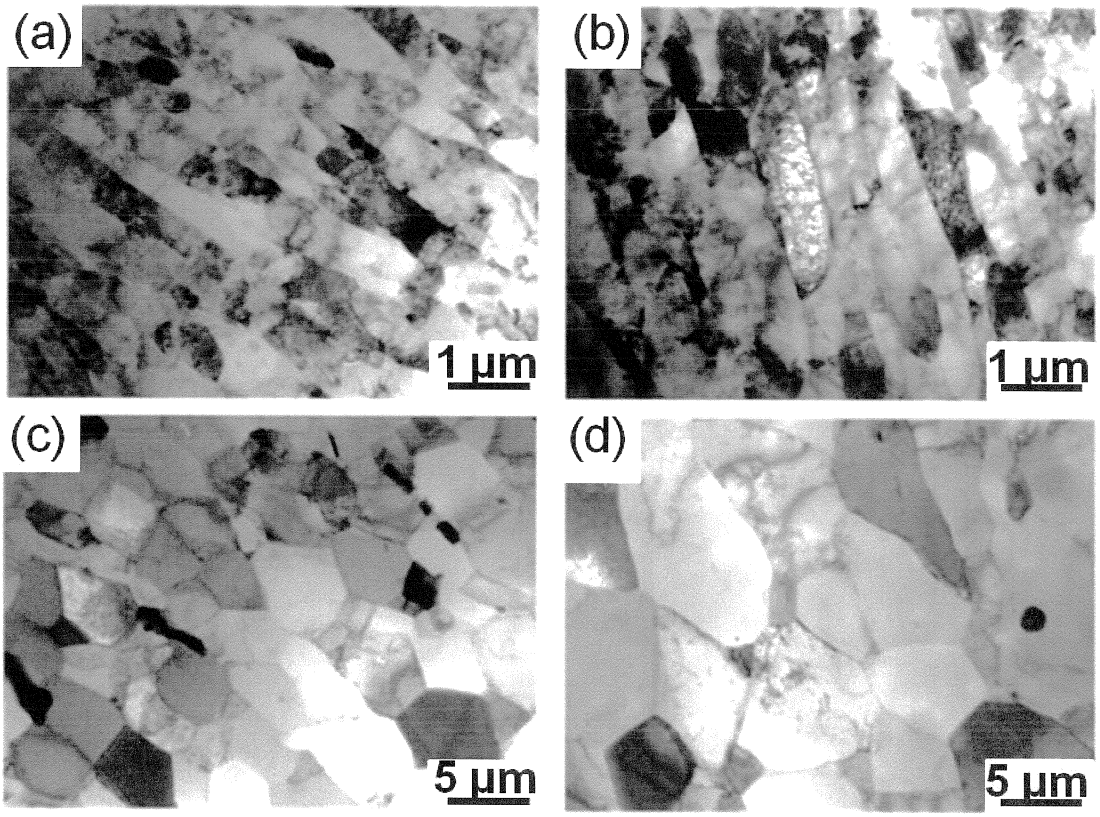

Fig. 2.14 TEM micrographs of the specimens torsion deformed to an equivalent strain of 3.6 under various Z conditions: (a) $Z = 2.21 \times 10^{26}$ s^{-1} (Region I), (b) $Z = 7.03 \times 10^{19}$ s^{-1} (Region I), (c) $Z = 1.28 \times 10^{14}$ s^{-1} (Region II) and (d) $Z = 1.28 \times 10^{10}$ s^{-1} (Region II).

Figure 2.15 shows the distribution of boundary misorientation angle obtained by EBSD in the specimens deformed to an equivalent strain of 3.6 under different Z conditions. The changes in misorientation angle distributions with decreasing Z values can be described as follows: (i) in the region I, the misorientation angle evolves the large peaks at low-angles, especially at misorientation angle below 10°. Decreasing Z value results in a peak shift from low-angle region to high-angle regions. (ii) In the region II, the results are different from the region I. The fraction of low misorientation angle mainly below 5° raises with decrease in Z value, meanwhile the fraction of high misorientation angle above 30° also increases continuously with decreasing Z value. Moreover, the average misorientation does not change so much with decrease in Z value

in the region II. The results indicate that the deformation conditions has strongly influenced on the microstructural evolution.

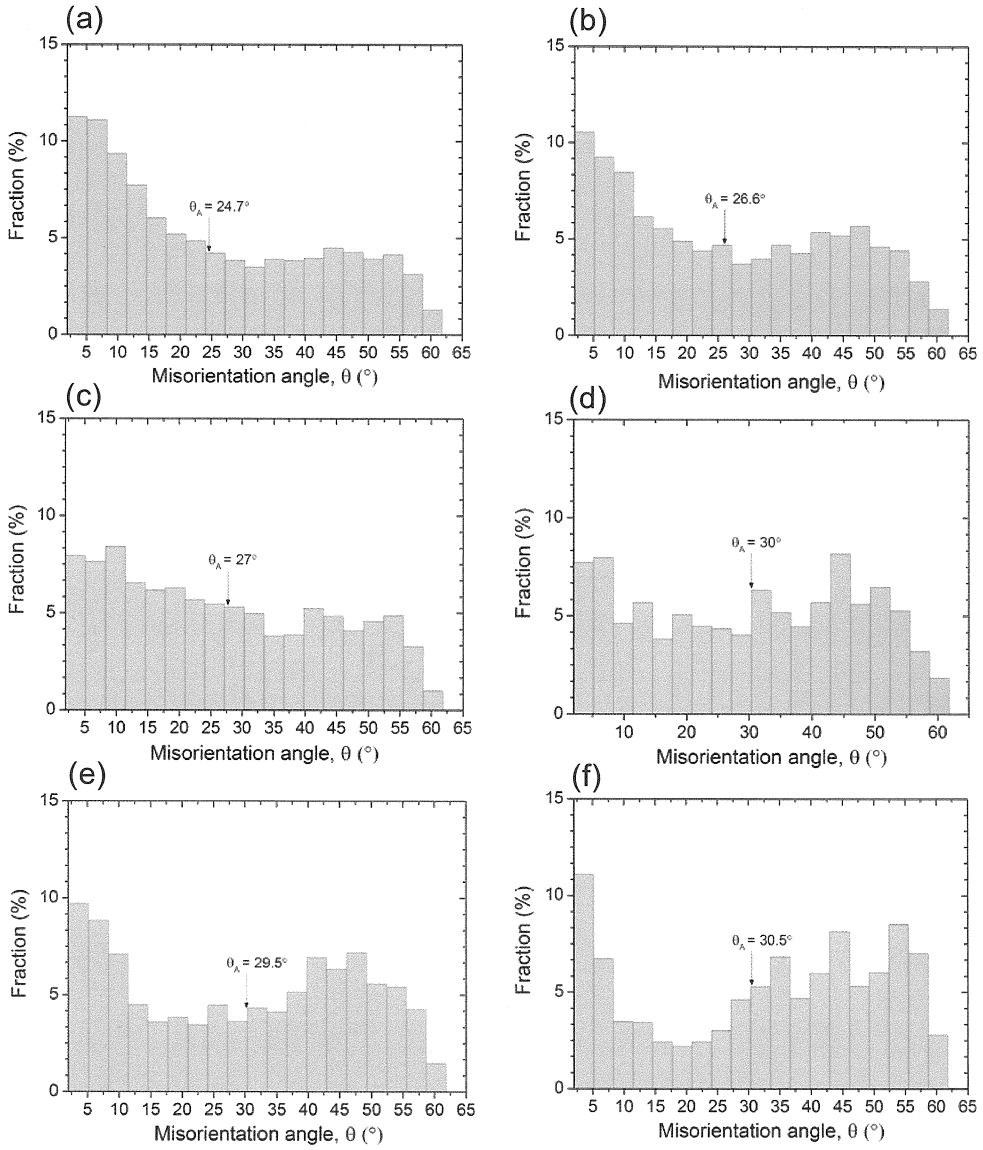

Fig. 2.15 Distribution of boundary misorientation angle obtained by EBSD in the specimens torsion deformed to an equivalent strain of 3.6 under different Z conditions: (a) $Z = 2.21 \times 10^{26}$ s^{-1} (Region I), (b) $Z = 7.03 \times 10^{19}$ s^{-1} (Region I), (c) $Z = 1.69 \times 10^{16}$ s^{-1} (Region I), (d) $Z = 1.28 \times 10^{14}$ s^{-1} (Region II), (e) $Z = 1.67 \times 10^{12}$ s^{-1} (Region II), and (f) $Z = 1.28 \times 10^{10}$ s^{-1} (Region II).

2.4.3 Z parameter dependence of microstructures

The average grain size (D_{all}) and fraction of high-angle grain boundary (F^{HAGB}) obtained from the grain boundary maps shown in **Fig. 2.12** and **2.13** are plotted as a function of Z parameter in log-log scale in **Fig. 2.16 (a)** and **(b)**, respectively. The grain size data of the same materials deformed by extrusion at intermediate to high temperatures (255-490 °C) and in the wide range of strain rates from 0.7 to 9.6 s^{-1} are also included in (a) for comparison [32, 38]. These plots indicate that the grain size and fraction of high-angle grain boundary are strongly dependent on Z parameter. The grain size tends to decrease with increasing Z value. However, the decrease in the grain size is not continuous: the transition of slope in D_{all}-Z plot occurs at around $Z = 2.47 \times 10^{-15}$ s^{-1}. The grain size decreases rapidly with increasing Z value up to Z_c, then slightly decreases with further increasing Z value. Meanwhile, the fraction of high-grain boundaries increases slightly with increasing Z value up to Z_c. In contrast, above Z_c, the fraction of high-grain boundaries decreases with increasing Z value as shown in **Fig. 2.16 (b).**

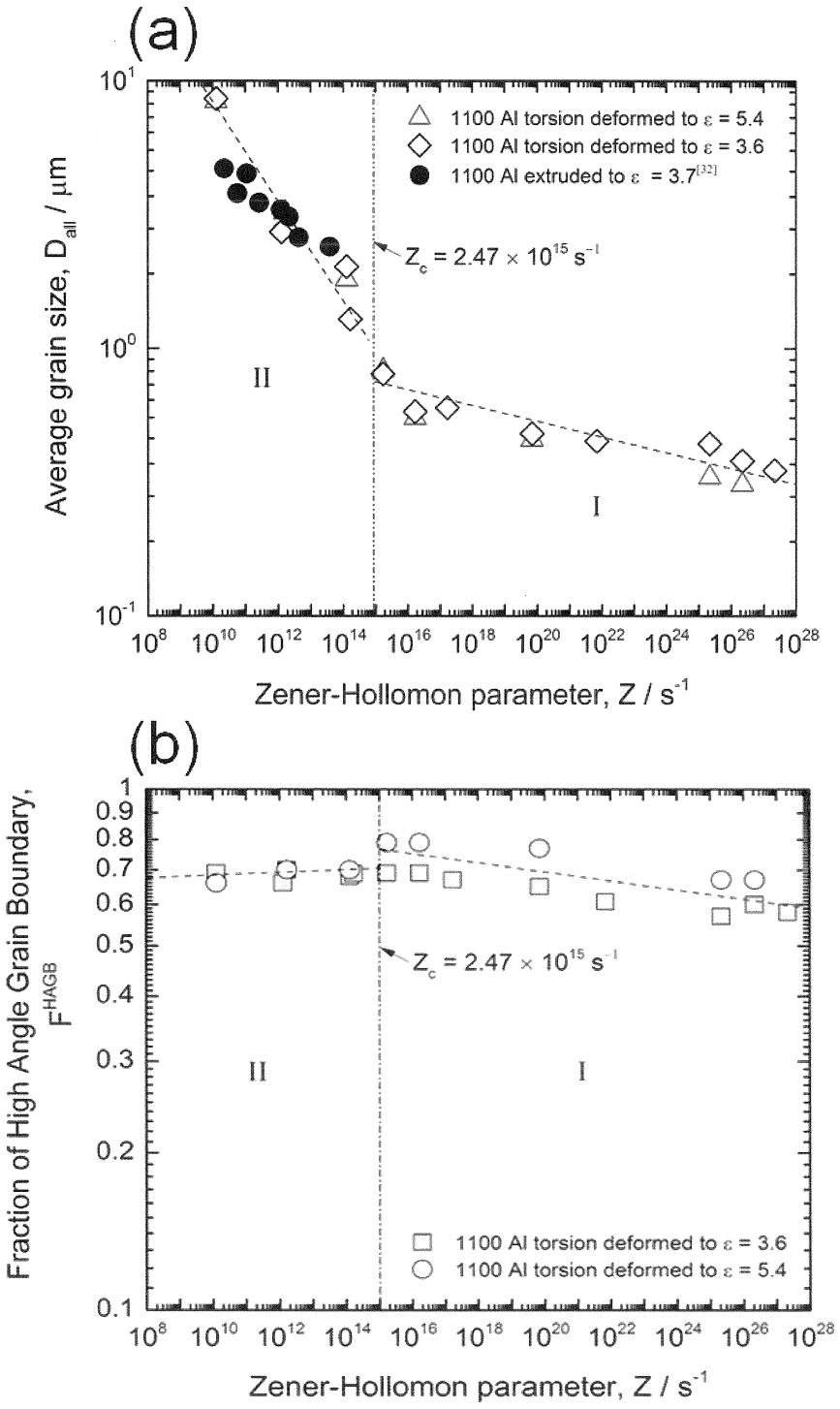

Fig. 2.16 (a) Average grain size (D_{all}) and (b) fraction of high-angle boundaries (F^{HAGB}) plotted as a function of Z parameter in log-log scale.

2.4.4 Discussions

2.4.2.1 Microstructure evolution mechanism dependent on Z parameter

The stress-strain curve analysis in a wide range of Z parameter from 1.28×10^{10} to 2.21×10^{29} s^{-1} showed two different regions: high Z value region (region I: $Z \geq Z_c$) and low Z value region (region II: $Z < Z_c$). The differences of these two regions are discussed in terms of microstructure evolution mechanisms.

In high Z region (region I), the specimens showed two types of stress-strain curves, i.e., work hardening and dynamic recovery. The n and Q values obtained from the stress- strain curves were 12.5 and 128 kJ mol^{-1}, respectively. This n value is slightly high but it is a typical value often observed in aluminum deformed at high Z conditions [14, 39]. The measured n value is very close to the stress exponent value anticipated for the deformation mechanism controlled by dislocation pipe diffusions in aluminum (n = 10) [40]. In addition, the evaluated Q value is comparable to the activation energy anticipated for dislocation cross-slip in aluminum (Q = 115 kJ mol^{-1}) [41, 42]. These results suggest that dynamic recovery mainly by dislocation cross-slip is the rate controlling mechanism in the high Z region. The microstructures quantitatively support this interpretation. That is, the microstructure consists of elongated grain structure, and the grain size does not significantly change with decreasing Z value (**Fig. 2.11 (a) – (c)**) and increasing equivalent strain (**Fig. 2.12**) in region I. Meanwhile, the amount of dislocations decreases and the dislocation structure changes from random tangles into more organized cell or subgrain structures with decreasing Z value. This is caused by the annihilation and rearrangement of dislocations (**Fig. 2.13 (a) – (b)**). It is reasonable to conclude, therefore, that dynamic recovery governed by dislocation cross-slip is a prominent mechanism for

microstructure evolution in this region.

In low Z region (region II), softening and steady state flow stress were observed in the stress-strain curves. The n and Q values were 4.5 and 164 kJ mol^{-1}, respectively. Many researchers have observed similar n value in aluminum deformed at high temperatures. It has been reported that when the n equals to 4.5, dislocation climb is the rate controlling mechanism [30, 43]. This has been proved by extensive experimental works [30,40,43], and by Weertman's dislocation-climb theory [40]. However, the evaluated Q value is higher than the self-diffusion energy of aluminum (142 kJ mol^{-1}) [34], indicating that the microstructure evolution mechanism in this region is not only attributed to dislocation climb but also to another mechanism(s). It was found that the evaluated Q value was comparable to the activation energy for the grain boundary migration in aluminum (Q = 172 kJ mol^{-1}) [44], which suggests that grain boundary migration contributed to the microstructure evolution in region II. The microstructure results are consistent with interpretation. That is, the microstructures consist of equaixed grain structures (**Fig. 2.14 (c)**). With decreasing Z the amount of dislocations decreases, the grain size increases and the grain boundaries became straight and clear (**Fig. 2.14 (d)**). Therefore, it can be concluded here that dislocation climb together with (short range of) grain boundary migration are the main mechanism for microstructure evolution in low Z region.

2.4.4.2 Grain size dependent on Z parameter

An obvious Z parameter dependence of the grain sizes was demonstrated in the present commercial purity aluminum (see **Fig. 2.16 (a)**). This result is consistent with the previous literatures reporting that the increase in Z parameter leads to finer grain

size. The change of slope in the D_{all}-Z plot in **Fig. 2.16 (a)** could be attributed to the change in the mechanism from dynamic recovery governed by dislocation cross slip above Zc to dislocation climb accompanying with grain boundary migration.

In the region I, the increase in Z value results in the finer grains because dynamic recovery rate decreases and the number of dislocations operated increases under higher Z conditions (i.e., lower deformation temperature and higher strain rate) as can be seen in **Fig. 2.14 (a - b)**. Under a constant imposed equivalent strain of 3.6, increasing Z parameter from 1.70×10^{16} to 2.21×10^{26} s^{-1} results in refinement of the grain size from 0.58 μm to 0.38 μm. The specimens deformed under the region II deformation conditions also showed the similar results. That is, the grain size decreased with increasing Z value. However, it is found that the finest grain size obtained in region II is larger than 1 μm (D_{all} = 2.00 μm), in other words, the ultrafine grained structure cannot be obtained below Z_c. These results indicate that higher Z parameter, especially above Z_c, is more preferable for the formation of ultrafine grained microstructures.

Based on the above discussion and results shown in **Fig. 2.16 (a)**, the relationship between Z parameter and grain size (D) obtained in this study can be expressed by two equations;

$$\log D = 1.18 - 0.014 \log Z \tag{2.10}$$

$$\log D = 19 - 0.59 \log Z \tag{2.11}$$

Eqs. (2.10) and **(2.11)** correspond to the region I and region II in **Fig. 2.15 (a)**, respectively.

2.4.5 Summary

The stress-strain behavior and microstructural evolution in torsion deformation of the commercial purity aluminum were studied at a wide range of temperatures from room temperature to 400 °C and at various strain rates from 10^{-2} s^{-1} to 10^{2} s^{-1}. The main findings obtained are as follows:

1. Stress-strain curves exhibited three types of flow curves, which depended on the deformation conditions. For the specimens deformed at low temperatures (RT- 200 °C), the stress-strain curves demonstrated work hardening and dynamic recovery types. Meanwhile, at high temperatures ($T \geq 300$ °C) and at low strain rates ($\dot{\varepsilon} < 10^{0}$ s^{-1}), softening and steady-state flow stress were observed. The relationship between the flow stress and the deformation conditions could be expressed using Zener-Hollomon parameter (Z) in a power law form.

2. Two distinct regions were observed when the flow stress was plotted as a function of Z parameter. The n values observed in the high Z and low Z regions (the region I and region II) were 12.5 and 4.5, respectively. Activation energies were found to be 128 and 164 kJ mol^{-1}, respectively, in the region I and region II. In the high Z region, the microstructures revealed lamellar structures having high dislocation density, while the equaixed grain structures with low dislocation density were observed in the low Z region. The boundary of two regions appeared at $Z_c = 2.47 \times 10^{15}$ s^{-1}, which was demonstrated by the evident change of n value, Q value and microstructures.

3. In the region I, the main mechanism of microstructure evolution was dynamic recovery governed by dislocation cross slip. Meanwhile, grain boundary migration and dislocation climb were found to be the main microstructure evolution mechanism operated in the region II.

4. The grain size decreased with increasing Z parameter. The result indicated that higher Z parameter was more preferable for the formation of ultrafine grained microstructures.

2.5 Conclusions

In Chapter 2, the effects of deformation conditions on the microstructural evolution in a commercial purity aluminum during torsion deformation were systematically studied at wide ranges of strain, deformation temperature and strain rate. The microstructural evolution in the specimens torsion deformed under various deformation conditions was characterized by EBSD measurement and TEM. Microstructure observations revealed that the change in the grain size and misorientation angle in the commercial purity aluminum deformed by torsion showed similar trend with that deformed by ARB process. The grain size decreased and the fraction of high-angle grain boundary increased with increasing strain. The ultrafine grained structures with a mean grain size smaller than 1 μm having large amounts of high-angle grain boundaries were achieved after a strain of 5.27 On the other hand, the flow stress of the specimens deformed under various Z conditions (i.e. various strain rates and deformation temperatures) tended to decrease with decreasing Z value. A transition of the flow stress in the σ_M-Z plot was observed at critical Z value (Z_c) of 2.47 $\times 10^{15}$ s^{-1}. Microstructure observations revealed that the grain shape clearly transformed from elongated to equiaxed grains and the grain size significantly changed at the Z_c value.

Based on the results obtained in Chapter 2, it could be concluded that torsion deformation worked as a kind of SPD process. The deformation conditions strongly influenced the microstructure evolution. The flow stress and microstructure results suggested that the transition of the flow stress trend in the σ_M -Z plot could be attributed to the change in the mechanism from dynamic recovery governed by dislocation cross

slip to grain boundary migration accompanied with dislocation climb from high Z conditions to low Z conditions.

References

[1] Segal V (2006)
Process mechanics and structure formation during SPD. Severe plastic deformation: towards bulk production of nanostructured materials.
Nova science publishers, New York, 1-22.

[2] Richert M, Liu Q and Hansen N
Microstructural evolution over a large strain range in aluminium deformed by cyclic-extrusion-compression.
Mater Sci Eng A (1999) 260:275-283.

[3] Zhilyaev A and Langdon T
Using high-pressure torsion for metal processing: fundamentals and applications.
Prog Mater Sci (2008) 53:893-979.

[4] Segal V
Equal channel angular extrusion: from macromechanics to structure formation.
Mater Sci Eng A (1999) 271:322-333

[5] Valiev R and Langdon T
Principles of equal-channel angular pressing asa processing tool for grain refinement.
Prog Mater Sci (2006) 51:881-981.

[6] Tsuji N, Saito Y, Lee SH and Minamino Y
ARB (accumulative roll-bonding) and other new techniques to produce bulk ultrafine grained materials.
Adv Eng Mater (2003) 5:338-344.

[7] Huang X, Tsuji N, Hansen N and Minamino Y
Microstructural evolution during accumulative roll-bonding of commercial purity aluminum.
Mater Sci Eng A (2003) 340:265-271.

[8] Terada D, Inoue S and Tsuji N
Microstructure and mechanical properties of commercial purity titanium severely deformed by ARB process.
J Mater Sci (2007) 42:1673-1681.

[9] Hughes D and Hansen N
High angle boundaries formed by grain subdivision mechanisms.
Acta Mater (1997) 45:3871-3886.

[10] Hansen N and Jensen DJ
Development of microstructure in FCC metals during cold work.
Phil Trans R Soc Lond A (1999) 357:1447-1469

[11] Hansen N, Mehl RF and Medalist A
New discoveries in deformed metals.
Metall Mater Trans A (2001) 32:2917-2935

[12] Liu Q, Huang X, Lloyd DJ and HansenN
Microstructure and strength of commercial purity aluminium (AA 1200) cold-rolled to large strains.
Acta Mater (2002) 50:3789-3802.

[13] Nakata N and Militzer M
Modelling of microstructure evolution during hot rolling of a 780 MPa high strength steel.
ISIJ Int (2005) 45:82-90.

[14] Mcqueen HJ, Spigerelli S and Kassner ME
Hot deformation and processing of aluminum alloys.
Taylor & Francis Group, LLC (2011) 59.

[15] Bailey JA and Haas SL
Effect of strain rate and temperature on the resistance to torsional deformation of several aluminum alloys technological.
Int J Mech Sci (1972)14:735-754.

[16] Likhachev VA, Myshlyaev MM and Olevskii SS
Superplasticity and structure of aluminium.
Acta Meter (1974) 22:829-834.

[17] Ryan ND, Mcqueen HJ and Jonas JJ (1983)
The deformation behavior of types 304, 316, and 317 austenitic stainless steels during hot torsion.
Can Metall Q 22: 369-378.

[18] Imbert CC and Mcqueen HJ
Peak strength, strain hardening and dynamic restoration of A2 and M2 tool steels in hot deformation.
Mater Eng A (2001) 313:88-103.

[19] Shrivastava SC, Jonas JJ and Canova G
Theoretical and practical considerations.
J Mecha Phy Solid (1982) 30:75-90

[20] Hosseini S and ManeshHabib
High-strength, high-conductivity ultra-fine grains commercial pure copper produced by ARB process.
Mater Design (2009) 30:2911-2918.

[21] Neishi K, Horita Z and Langdon T
Grain refinement of pure nickel using equal-channel angular pressing.
Mater Sci Eng A (2002) 325:54-58.

[22] Todaka Y, Umemoto M, Yamazaki A, Sasaki J and Tsuchiya K
Influence of high-pressure torsion straining conditions on microstructure evolution in commercial purity aluminum.
Mater Trans (2008) 49:7-14.

[23] Loucif A, Figueiredo RB, Baudin T, Brisset F and Longdon T
Microstructural evolution in an Al-6061 alloy processed by high-pressure torsion.
Mater Sci Eng A (2010) 527:4864-4869.

[24] Kamikawa N (2005)
Grain refinement of structural metallic materials by accumulation roll bonding.
PhD thesis, Osaka University

[25] Zhilyaeva A, Kim B, Nurislamova G, Baroo M, Szpunar J and Langdon T
Orientation imagingmicroscopy of ultrafine-grained nickel.
Scr Mater (2002) 46:575-580.

[26] Xu C,Horita Z and Langdon T
The evolution of homogeneity in processing by high-pressure torsion.
Acta Mater (2007) 55:203-212.

[27] Jiang H, Zhu Y, Butt D, Alexandrov I and Lowe T
Microstructural evolution, microhardness and thermal stability of HPT-processed Cu.
Mater Sci Eng A (2000) 290:128-138.

[28] Sakai G, Nakamuraa K, Horita Z and Langdon T
Developing high-pressure torsion for use with bulk samples.
Mater Sci Eng A (2005) 406:268-273.

[29] Vorhauer A and Pippan R
On the homogeneity of deformation by high pressure torsion.
Scr Mater (2004) 51:921-925.

[30] Jonas JJ, Sellars CM and Tegart WJ
Strength and structure under hot-working conditions.
Int Mater Rev (1969) 14:1-24.

[31] Li Y, Zhang Y, Tao N and Lu K
Effect of the Zener–Hollomon parameter on the microstructures and mechanical properties of Cu subjected to plastic deformation.
Acta Mater (2009) 57:761-772.

[32] Mcqueen HJ and Hockett JE
Microstructures of aluminum compressed at various rates and temperatures.
Met Trans (1970) 1:2997-3004.

[33] Sellars CM and Mctegart WJ
On the mechanism of hot deformation.
Acta Metall (1966) 14: 1136-1138.

[34] Lundy TS and Murdock JF
Diffusion of Al26 and Mn54 in aluminum.
J Appl Phy (1962) 33: 1671.

[35] Yavari P and Langdon TG
An examination of the breakdown in creep by viscous glide in solid solution alloys at high stress levels.
Acta Metall (1982) 30:2181-2196.

[36] Srikant G, Marple B, Charit I and Murty KL
Characterization of stress rupture behavior of commercial-purity-Ti via burst testing.
Mater Sci Eng A (2007) 463:203-207.

[37] Sherby OD and Burke PM
Mechanical behavior of solids at high temperatures.
Prog Mater Sci (1967) 13:325-390.

[38] Wong WA and Jonas JJ
Aluminum extrusion as a thermally activated process.
Trans Metall Soc AIME (1968):2271-2280.

[39] Kovács-Csetényi E, Chinh NQ, Kovács I
Hot deformation mechanisms in commercial purity aluminium.
Phys Stat Sol (a) (1995)148: 135-141.

[40] Walser B and Sherby OD
The structure depence of power law.
Scripta Mettal (1982)16:213-219.

[41] Jaffe N and Dorn JE (1960)
Effect of temperature on the creep of polycrystalline aluminum by cross-slip mechanism.
Wright air development division air research and development command
United States air force wright-patterson air force base: 1-17.

[42] Sherby OD, Lytton JL and Dorn JE
Activation energies for creep of high-purity aluminum.
Acta Mettall (1957) 5:219-227.

[43] Chinh NQ, Illy J, Horita Z and Langdon TG
Using the stress–strain relationships to propose regions of low and high temperature plastic deformation in aluminum,
Mater Sci Eng A (2005) 410-411:234-238.

[44] Vandermeer RA and Jensen DJ
Microstructural path and temperature dependence of recrystallization in commercial aluminum.
Acta Mater (2001) 49:2083-2094.

Chapter 3 Mechanical properties of bulk ultrafine grained aluminum fabricated by torsion deformation

3.1 Introduction

Ultrafine-grained (UFG) materials have become an interesting subject in the research of materials science because of their unique microstructures and excellent mechanical properties [1]. It was demonstrated in the previous chapter that torsion deformation could be one of the severe plastic deformation (SPD) processes to fabricate bulk UFG aluminum alloys. The torsion deformation has an advantage in accurately controlling deformation conditions (i.e., temperature and strain rate) and also allows a continuous impose of large strain without interruption, compared with other SPD processes [2]. However, the microstructure and mechanical properties of the UFG materials fabricated by torsion deformation have not been fully clarified yet. One reason is that the torsion deformation has been rarely used for producing bulk UFG materials, and another reason is the difficulty to fabricate mechanical testing samples from torsion deformed specimens. In **Chapter 2**, the microstructure evolution of the UFG aluminum fabricated through torsion deformation has been systematically studied. Although the mechanical properties of the UFG materials produced by torsion deformation have not been widely investigated, the ultrahigh strength could be expected for the UFG aluminum according to well-known Hall-Petch relationship [3,4],

$$\sigma_y = \sigma_0 + k_y d^{-\frac{1}{2}} \tag{3.1}$$

where σ_y is the yield stress, σ_0 is the friction stress required to move dislocations in very coarse grains, k_y is the Hall-Petch coefficient, and d is the average grain size.

The Hall-Petch relationship suggests that the yield stress should increase proportionally with decreasing the minus square root of the mean grain size, in other words, the yield stress of the UFG material can be estimated from the microstructural parameter (grain size) by extrapolating the Hall-Petch relation of coarse grained materials. Recently, it has been also reported that the Hall-Petch relationship is no longer valid for UFG and nanostructured materials in some cases [5-10]. For example, several researchers have reported that the UFG materials exhibit ultrahigh strength, which is higher than that predicted from the Hall-Petch relationship for coarse-grained materials [5-10]. On this background, it can be said that the strengthening mechanism of the UFG materials is quite complex and still unclear. Therefore, in the present chapter the author tries to clarify the following two issues. One objective of this work is to characterize the mechanical properties and microstructures of the UFG materials fabricated by torsion deformation at various temperatures and strain rates. The other aim of the present chapter is to clarify the strengthening mechanism of the UFG materials on the basis of the microstructural parameters.

3.2 Experimental procedure

3.2.1 Torsion deformation

The material used in this chapter was a commercial purity aluminum (1100Al), which was the same material used in **Chapter 2**. The chemical composition of the material was listed in **Table 2.1**. The torsion specimens having a cylindrical gage part 4 mm in length and 8 mm in diameter were machined from the as-received aluminum bars. The details about the dimension and the shape of the torsion specimens were given in **Fig. 2.1**. In order to study the mechanical properties of the UFG aluminum, the

specimens were deformed up to 1.1 rotations (corresponding to the maximum equivalent strain of 4 at the surface) under five different Zener-Hollomon (Z) conditions (2.21×10^{26}, 1.69×10^{15}, 1.28×10^{14}, 1.67×10^{12} and 1.28×10^{10} s^{-1}) by torsion deformation. The deformation procedure was illustrated in **Fig. 2.2**.

3.2.2 Microstructural analysis

The microstructures of the torsion deformed specimens were well characterized by electron back-scattering diffraction (EBSD) measurement in a field-emission scanning electron microscope (FE-SEM, Phillips FEI XL30S FEG) and transmission electron microscopy (TEM). The results of the microstructural examinations such as morphology of the grain, grain size and misorientation angle obtained by the EBSD measurement and TEM have been reported in **Chapter 2** (**Figs. 2.4, 2.12, 2.14** and **2.15**). However, the dislocation densities in those torsion deformed specimens are not evaluated yet. Therefore, in this chapter, the dislocation densities in the torsion deformed specimens were determined by X-ray diffraction (XRD). The X-ray measurement was performed using Rigaku Smart-Lab X-ray diffractometer with Cu Kα radiation.

3.2.3 Mechanical testing

Mechanical properties of the torsion deformed specimens were characterized by tensile test at room temperature. The tensile test specimens were cut from near surface regions in the gage part of the torsion deformed specimens (~0.9R), as is illustrated in **Fig. 3.1 (a)**. In the near surface region of the torsion specimens, a high shear strain could be obtained, and that was also the position of microstructural observations. The

sheet-type tensile test specimens had dimensions 2 mm in gage length and 1 mm in gage width. The cut specimens were mechanically polished down to a thickness of 0.4 mm. The tensile test specimen is illustrated in **Fig. 3.1 (b)**.

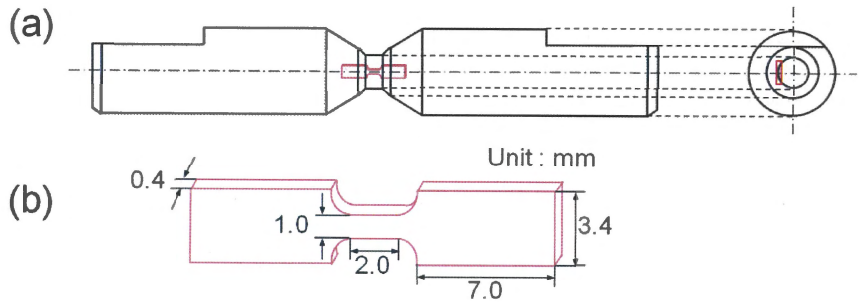

Fig. 3.1 (a) Illustration of the side and top view of the specimen deformed by torsion, showing the position where the tensile specimen was taken. (b) Dimension and shape of the tensile test specimen.

Tensile test was carried out using an universal test machine Shimadzu model AG-I 100 kN at room temperature and an initial strain rate of 8.3×10^{-4} s^{-1}. The tensile direction was perpendicular to the shear direction in torsion. A CCD camera was used to measure the precise elongation during the tensile test. The structural parameters (e.g., morphology of the grains, grain size and misorientation angle) of the torsion deformed specimens reported in **Chapter 2**, were also used for the discussion on the change in mechanical properties and strengthening mechanism of the UFG aluminum in this chapter.

3.3 Results and discussion

3.3.1 Microstructures of torsion deformed specimens

The microstructures of the starting material and the specimens deformed by torsion to an equivalent strain of 3.6 under a wide range of Z conditions from 1.28×10^{10} s^{-1} to 2.21×10^{26} s^{-1} were characterized by EBSD measurement and TEM. The microstructures of the starting material and deformed specimens were shown in the previous chapter (**Fig. 2.4, 2.12** and **2.14**). The starting material had a fully recrystallized structure having an average grain size of 28 μm (**Fig. 2.5 (a)**). After deformation at $Z = 2.21 \times 10^{26}$ s^{-1}, the microstructure consisted of a lamellar boundary structure nearly parallel to the shear direction (**Fig. 2.12 (a)**). The mean grain size (thickness) determined from high-angle boundaries (D_{HAGB}) was 0.63 μm. In the specimen deformed at $Z = 1.69 \times 10^{15}$ s^{-1}, the microstructure mainly consisted of elongated grains, most of the grains were surrounded by high angle grain boundaries, and the mean grain size determined from high-angle boundaries increased to 1.16 μm (**Fig. 2.12 (b)**). With decreasing Z value furthermore, the microstructure changed to more equiaxed grains surrounded by high angle boundaries (**Fig. 2.12 (d) – (f)**). The mean grain size increased with decreasing the Z values. The mean grain sizes (D_{HAGB}) of the specimens deformed at Z values from 1.28×10^{14} s^{-1} to 1.28×10^{10} s^{-1} were in a rage from 2.9 μm to 12.4 μm. When the grain size was determined using all boundaries in the EBSD boundary maps (low-angle boundaries + high-angle ones), the mean grain size (D_{all}) was naturally smaller than D_{HAGB}, which is summarized in **Table 3.1.**

In order to examine more details in the microstructures, TEM observations were also performed. TEM micrographs of the specimens deformed at various Z values were shown in **Fig. 2.14**. It was found that the microstructures of the specimen deformed at

high Z values ($Z \geq 1.69 \times 10^{15}\ s^{-1}$) consisted of elongated grains having large amount of dislocations as shown in **Fig. 2.14 (a)** and **(b)**. When the Z value decreased down to $1.28 \times 10^{14}\ s^{-1}$ and below, the microstructures consisted of equiaxed grains having low dislocation densities (**Fig. 2.14 (c)** and **(d)**).

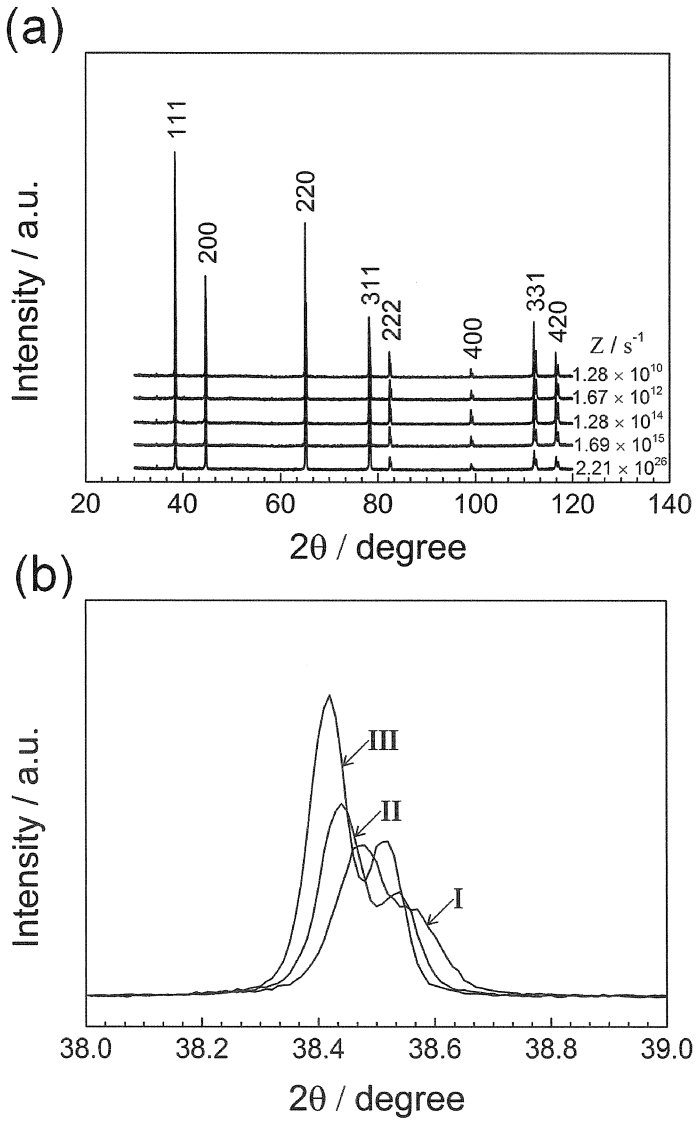

Fig. 3.2 (a) X-ray diffraction patterns of the specimens after torsion deformation by 1.1 rotations at various Z values. (b) X-ray diffraction peaks of (111) plane of the specimens deformed at various Z values: (I) $2.21 \times 10^{26}\ s^{-1}$, (II) $1.69 \times 10^{15}\ s^{-1}$, and (III) $1.28 \times 10^{14}\ s^{-1}$.

Figure 3.2 shows XRD results of the specimens after torsion deformation by 1.1 rotations at various Z values. It was found that all the diffraction peaks were well matched with the diffraction pattern of aluminum with face-centered cubic (fcc) structure and no other phases were observed in the XRD pattern as shown in **Fig. 3.2 (a)**. For a careful examination of the changes in diffraction peaks with increasing the Z value in torsion deformation, the X-ray diffraction peak of (111) plane was selected and shown in **Fig. 3.2 (b)**. It could be clearly seen that the intensity of the X-ray diffraction peak decreased and the peak was broadened with increasing Z value. Though the peak position seems to shift to lower angle side with decreasing the Z value, the accuracy and reason for that are unclear at this moment. Generally, broadening of the peak is caused by refinement of crystalline size and/or increasing dislocation density. The dislocation density (ρ) can be quantitatively estimated from the XRD pattern using Williamson-Hall method through following equations [11,12]:

$$\rho = \frac{k\,\varepsilon^2}{F\,b^2} \tag{3.2}$$

where k and F are constant values (16.1 for FCC material and 1, respectively), b is the magnitude of Burgers vector (0.286 nm for aluminum), ε is the lattice strain described by $\{(\beta\cos\theta/\lambda)/(2\sin\theta/\lambda)\}$, β is the full-width at half maximum height (FWHM) of the peaks, λ is the wave length of X-ray and θ is the diffraction angle.

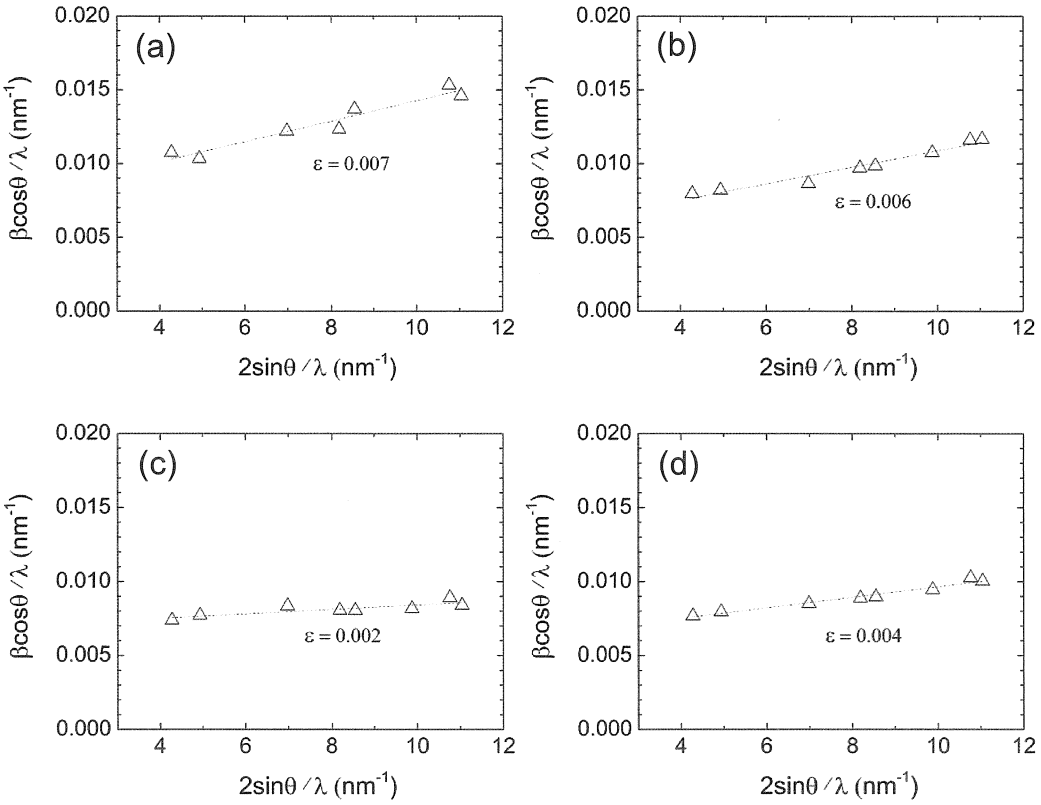

Fig. 3.3 Williamson-Hall analysis of the specimens torsion deformed at various Z values (a) $2.21 \times 10^{26}\ s^{-1}$, (b) $1.69 \times 10^{15}\ s^{-1}$, (c) $1.28 \times 10^{14}\ s^{-1}$, and (d) $1.67 \times 10^{12}\ s^{-1}$.

Figure 3.3 shows ε values obtained from plotting $\beta\cos\theta/\lambda$ of all the eight XRD peaks versus $2\sin\theta/\lambda$, where the lattice strain, ε, is also indicated. The lattice strain values evaluated from the XRD results were used for determining the dislocation density of all the specimens using **Eq. 3.2**. The dislocation density evaluated from the XRD results are summarized in **Table 3.1**. It is found that the dislocation density increases with increasing Z value, which qualitatively coincides with the TEM observations (**Fig. 2.13**). The dislocation densities evaluated from the XRD results are in the range from $7.81 \times 10^{12}\ m^{-2}$ to $9.56 \times 10^{13}\ m^{-2}$. The dislocation density results shown in **Table 3.1** are qualitatively in good agreement with the experimental data reported for aluminum severely deformed by ARB process under similar deformation conditions [13].

Table 3.1 The structural parameters determined by EBSD measurement and XRD. In this table, D_{all} is the average (sub)grain size taking account of all boundaries having misorientation above 2°, D_{HABG} is the mean grain size measured from high angle grain boundaries ($\theta \geq 15°$), F^{HAGB} is the fraction of high angle grain boundaries, and ρ is the dislocation density.

Zener-Hollomon parameter, Z / s^{-1}	D_{all} / μm	D_{HAGB} / μm	F^{HAGB}	ρ /m^{-2}
Starting material	23.00	28.00	0.76	Not measured
2.21×10^{26}	0.38	0.63	0.60	9.56×10^{13}
1.69×10^{15}	0.80	1.16	0.69	5.68×10^{13}
1.28×10^{14}	2.02	2.92	0.69	4.88×10^{13}
1.67×10^{12}	2.83	4.04	0.70	3.12×10^{13}
1.28×10^{10}	8.56	12.40	0.69	7.81×10^{12}

3.3.2 Mechanical properties of torsion deformed specimens

The room-temperature stress–strain curves of the specimens torsion deformed by 1.1 rotations at various Z values are shown in **Fig. 3.4**. The stress-strain curve of the starting (undeformed) specimen is also included in this figure for comparison and the Z value and grain size are indicated in **Fig. 3.4**. Here, D_{all} is indicated as the grain size.

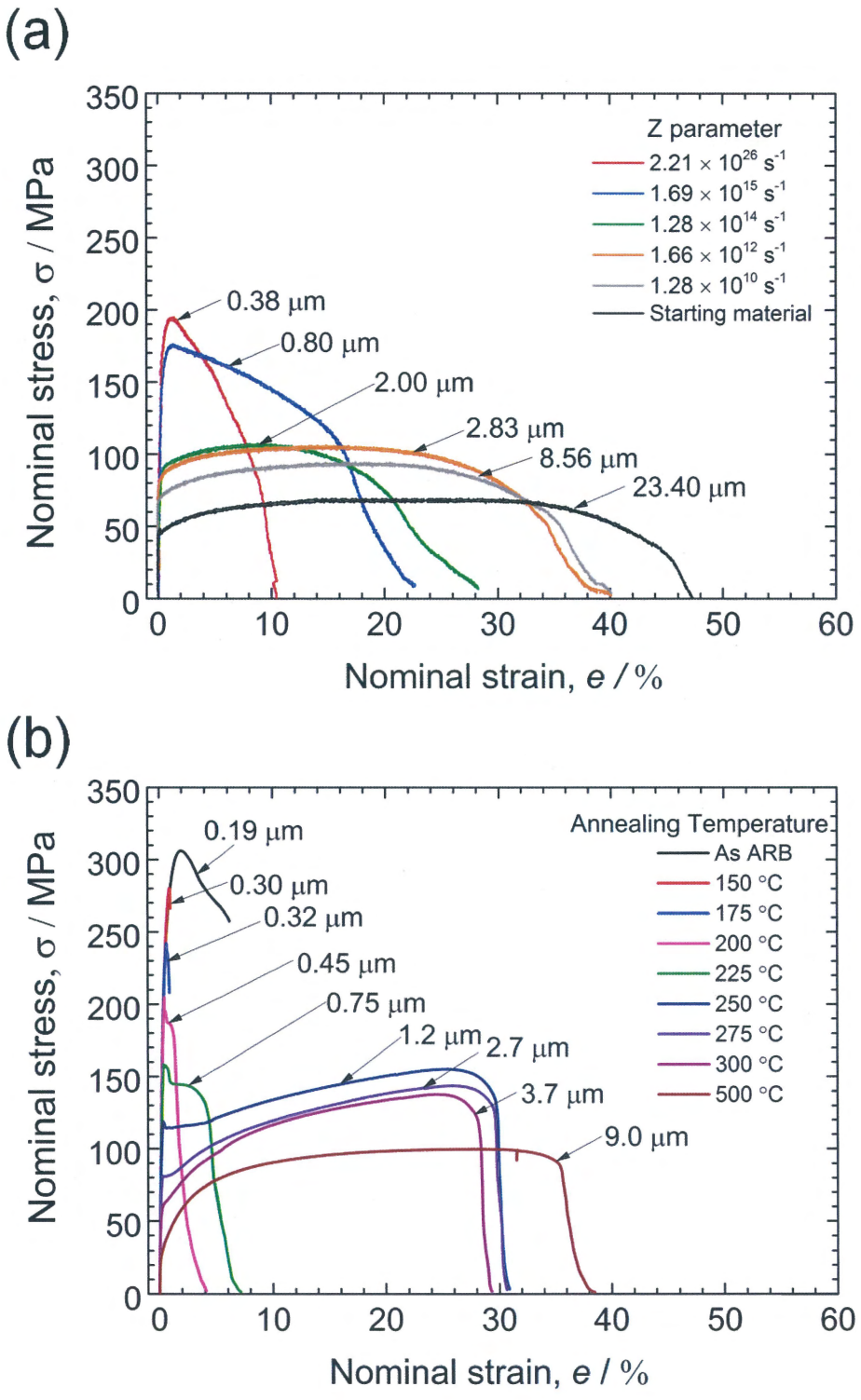

Fig. 3.4 Room-temperature stress-strain curves of the (a) 1100Al torsion deformed by 1.1 rotations under various Z conditions, and (b) 1100Al ARB processed by 6 cycles (equivalent strain of 4.8) at RT and annealed at various temperatures for 1.8 ks [14].

It was seen from **Fig. 3.4 (a)** that the ultrafine grained materials showed very high strength. For example, the yield stress (151 MPa) and ultimate tensile strength (195 MPa) of the specimen with the mean grain size of 0.38 μm were almost three times higher than those of the starting material (27 MPa and 65 MPa, respectively). However, it was also found that the flow curves of the specimens with the mean grain sizes smaller than 1 μm reached the maximum stress at early stage of tensile test, resulting in a very limited uniform elongation. Similar results have been found in the UFG 1100Al produced by ARB process and subsequent annealing [14]. For comparison, the stress-strain curves of the 1100Al ARB processed by 6 cycles (equivalent strain of 4.8) at R.T. are shown in **Fig. 3.4 (b)**. The mean grain size (D_{all}) [14] is also indicated in **Fig. 3.4 (b)**. It should be noted here that the UFG 1100Al fabricated by torsion deformation exhibits different shapes of stress-strain curves from those of the UFG 1100Al produced by ARB and annealing. The ARB processed and annealed specimens having the mean grain sizes smaller than 3.7 μm show discontinuous yielding characterized by yield-drop, while the UFG 1100Al produced by torsion deformation does not show yield point phenomenon.

The 0.2% proof stress ($\sigma_{0.2}$), ultimate tensile strength (σ_{UTS}), uniform tensile elongation (e_u) and total tensile elongation (e_t) were measured from all the stress-strain curves of the torsion deformed specimens and plotted as a function of Z value or average grain size (D_{all}) in **Fig. 3.5**.

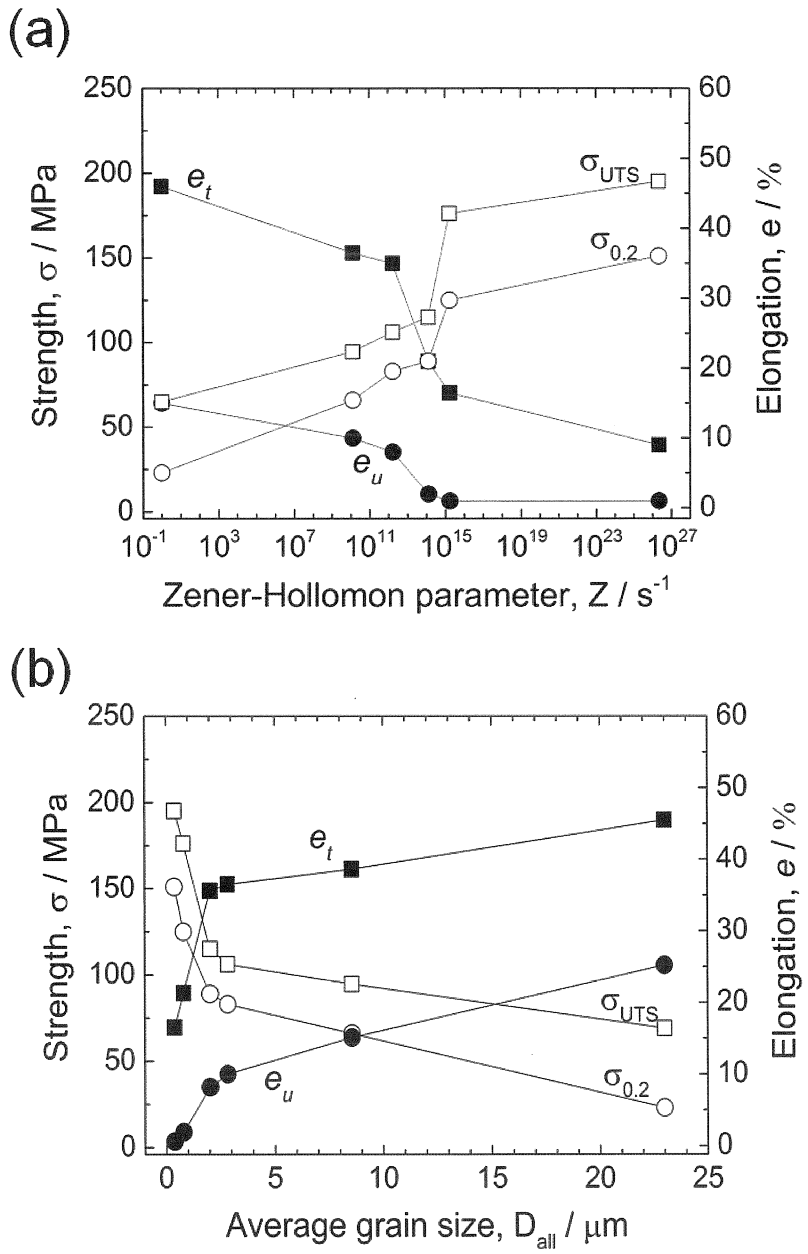

Fig. 3.5 The 0.2% proof stress ($\sigma_{0.2}$), tensile strength (σ_{UST}), uniform elongation (e_u), and total elongation (e_t) of the torsion deformed 1100 aluminum, plotted as a function of (a) Z parameter and (b) grain size (D_{all}).

It is found that the strength increases with increasing Z value **(Fig. 3.5 (a)),** in other words, with decreasing the grain size **(Fig. 3.5 (b)).** The strength gradually increases with increasing Z, but it greatly increases at around $Z = 1.69 \times 10^{15}$ s^{-1}

(corresponding to the grain size of about 0.80 μm). This corresponds to the change in microstructures from more equiaxed morphologies to elongated lamellar morphologies, as was shown in **Fig. 2.12**. The tensile elongation significantly decreases when the grain size is smaller than 1 μm. Similar results have been observed in various kinds of ultrafine grained metallic materials fabricated by severe plastic deformation and subsequent annealing, such as pure aluminum [10], aluminum alloys [6, 15] and IF steel [16]. Actually, sudden drop of tensile elongation below grain size of 1 μm is also found in the ARB processed and annealed 1100Al shown in **Fig. 3.4 (b)**. The low tensile ductility, especially the limited uniform elongation, of ultrafine grained metallic materials is attributed to high yield strength and lack of work hardening, which causes plastic instability (necking in tensile deformation) occurring at very early stage of the tensile test. This can be described by the Considère's criterion for plastic instability, as

$$\frac{d\sigma}{d\varepsilon} \leq \sigma \tag{3.3}$$

where σ is the true flow stress, ε is the true strain and $d\sigma/d\varepsilon$ is the work hardening rate. UFG materials exhibit high flow stress (especially high yield strength) compared with those of the coarse grained materials. On the other hand, the work hardening is not enhanced by grain refinement. Therefore, the plastic instability condition expressed in **Eq. (3.3)** is achieved and necking starts at very low strain, which results in limited uniform elongation.

The 0.2% proof stresses obtained from the tensile test of the torsion deformed specimens are also plotted as a function of minus square root of the grain size (D_{all}) in **Fig. 3.6** (Hall-Petch plot). The 0.2% proof stresses of the same material reported by Kamikawa [14], i.e., the coarse grained specimens fabricated by conventional cold-rolling and annealing processes, and the UFG specimens fabricated by ARB and

annealing processes (corresponding to **Fig. 3.4 (b)**), are also plotted in **Fig. 3.6** for comparison.

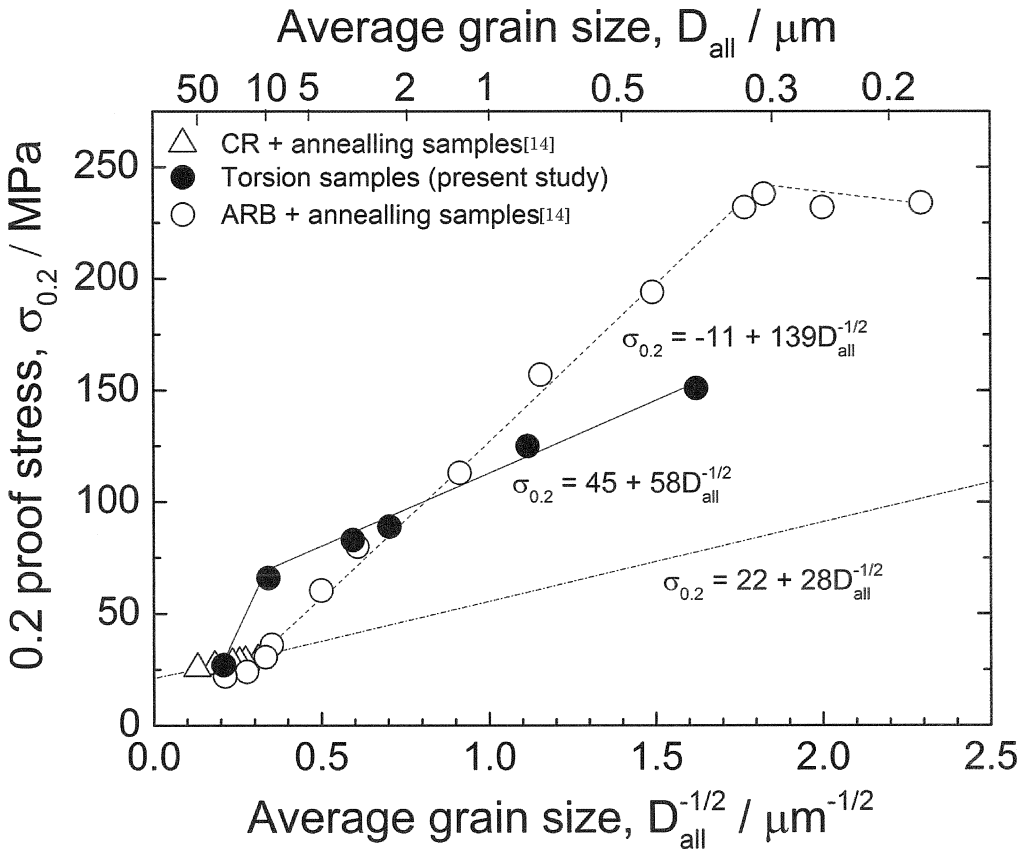

Fig. 3.6 Hall-Petch plot of the 0.2% proof stress of the 1100Al torsion deformed under various *Z* conditions. The proof stress of coarse grained 1100Al cold rolled (CR) and annealed and that of 1100Al ARB processed and annealed (in reference [14]) are also plotted.

One can clearly see from this figure that the UFG aluminum processed by torsion deformation exhibits higher strength than that of the extrapolation of the Hall-Petch relationship for coarse grained aluminum. In other words, the UFG aluminum exhibits extra-hardening. Extra-hardening has been reported in the UFG materials including 1100Al fabricated by ARB and annealing processes [10,14], which is also shown in **Fig. 3.6**. However, it is found in **Fig. 3.6** that the extra-hardening of the UFG

aluminum fabricated by torsion deformation is significantly different from that of the ARB processed and annealed specimens, which seems to correspond with the difference in the stress-strain behaviors between them show in **Fig. 3.4**. It has been clarified that the extra hardening of the UFG materials fabricated by SPD (ARB) and annealing processes is mainly attributed to the yield-point phenomena characteristically happening in UFG microstructures [17], and it is referred as *dislocation source hardening* [10]. It is, however, not the case for the present UFG aluminum fabricated by torsion deformation, since the torsion specimens do not show obvious yield-point phenomena as shown in **Fig. 3.4**.

Probably the difference in the extra hardening behaviors is caused by the difference in the microstructures of the UFG aluminum produced by torsion deformation and that by ARB process and annealing. It is known that the UFG aluminum fabricated by ARB process shows the lamellar morphology having characteristics of deformation structures, i.e., elongated grain shapes, high density of dislocations and large number of low angle boundaries [5]. When the ARB processed aluminum is annealed at relatively low temperatures, the elongated morphology is maintained but the dislocation density decreases by recovery process with increasing the annealing temperature. Eventually, equiaxed grains free from dislocations inside can be obtained [5, 14]. Such microstructures are equivalent to fully recrystallized microstructures. On the other hand, the torsion deformed aluminum always maintains deformation characteristics, although the morphology of the ultrafine grains changes from elongated ones to more equiaxed ones with decreasing Z value (**Figs. 2.12** and **2.14**). In fact, as shown in **Table 3.1**, the specimen torsion deformed under the lowest Z condition (1.28×10^{10} s^{-1}) still maintains the dislocation density of 7.81×10^{12} m^{-2},

which is significantly higher than that in fully recrystallized metallic materials (10^9 – 10^{10} m^{-2}). Then, the extra hardening of the torsion deformed aluminum is discussed quantitatively on the basis of the substructures hereafter.

Now the strength of the UFG aluminum fabricated by torsion deformation is estimated by adding various strengthening mechanisms, in order to understand the extra hardening in the torsion specimens. In metallic materials, several kinds of strengthening mechanisms can be considered, which are dislocation strengthening (strain hardening), grain boundary strengthening, solution hardening and precipitation/dispersion hardening [18]. In the present commercial purity aluminum, contributions of solution hardening and precipitation/dispersion strengthening can be ignored, as the amount of solute atoms and precipitates are little. On the other hand, the EBSD, TEM and XRD results showed that the torsion deformed aluminum contained fine-grained structure and high density of dislocations. Therefore, the yield strength (0.2% proof stress: $\sigma_{0.2}$) of the torsion deformed specimens is estimated from the microstructural parameters, assuming the additional strengthening law of the friction stress (σ_0), the contribution of grain boundary strengthening (σ_{gb}) and that of dislocation strengthening (σ_d), i.e.,

$$\sigma_{0.2} = \sigma_0 + \sigma_{gb} + \sigma_d \tag{3.4}$$

According to Hansen et al. [19], the contributions of grain boundary strengthening and dislocation strengthening in the UFG materials fabricated by SPD can be written as,

$$\sigma_{0.2} = \sigma_0 + k_y d^{-\frac{1}{2}} + M \alpha G b \sqrt{\rho} \tag{3.5}$$

where k_y is the Hall-Petch slope, d is the mean grain size, M is Taylor factor (3.0) [20], α is a constant (0.24) [21], G is the shear modulus (26 GPa), b is the magnitude of Burgers vector (0.286 nm) and ρ is the dislocation density. The value of 22 MPa is used

as σ_0 [14]. As k_y, the value of 28 MPa $\mu m^{0.5}$ obtained by Kamikawa [14] for coarse grained aluminum is used. D_{HAGB} is used as the mean grain size (d) for the calculation, which was summarized in **Table 3.1** together with the dislocation density (ρ).

In **Figure 3.7**, the 0.2% proof stresses of the torsion deformed specimens calculated according to **Eq. 3.5** using experimentally obtained D_{HAGB} and ρ are indicated as bars in the Hall-Petch plot. The results are plotted for two kinds of the mean grain sizes, (a) D_{HAGB} and (b) D_{all}. The 0.2% proof stresses obtained from tensile testes are also plotted as closed circles in **Fig. 3.7** for comparison. It can be seen that the calculated 0.2% proof stress shows a relatively good agreement with the experimental result, regardless of the kind of the mean grain size (D_{HAGB} or D_{all}). The contribution of grain boundary strengthening (σ_{gb}) indicates the Hall-Petch relationship for coarse grained specimens. Therefore, it can be concluded that the extra hardening in the present UFG aluminum fabricated by torsion deformation can be understood mainly by strengthening owing to the substructures observed within the microstructures (dislocation strengthening: σ_d).

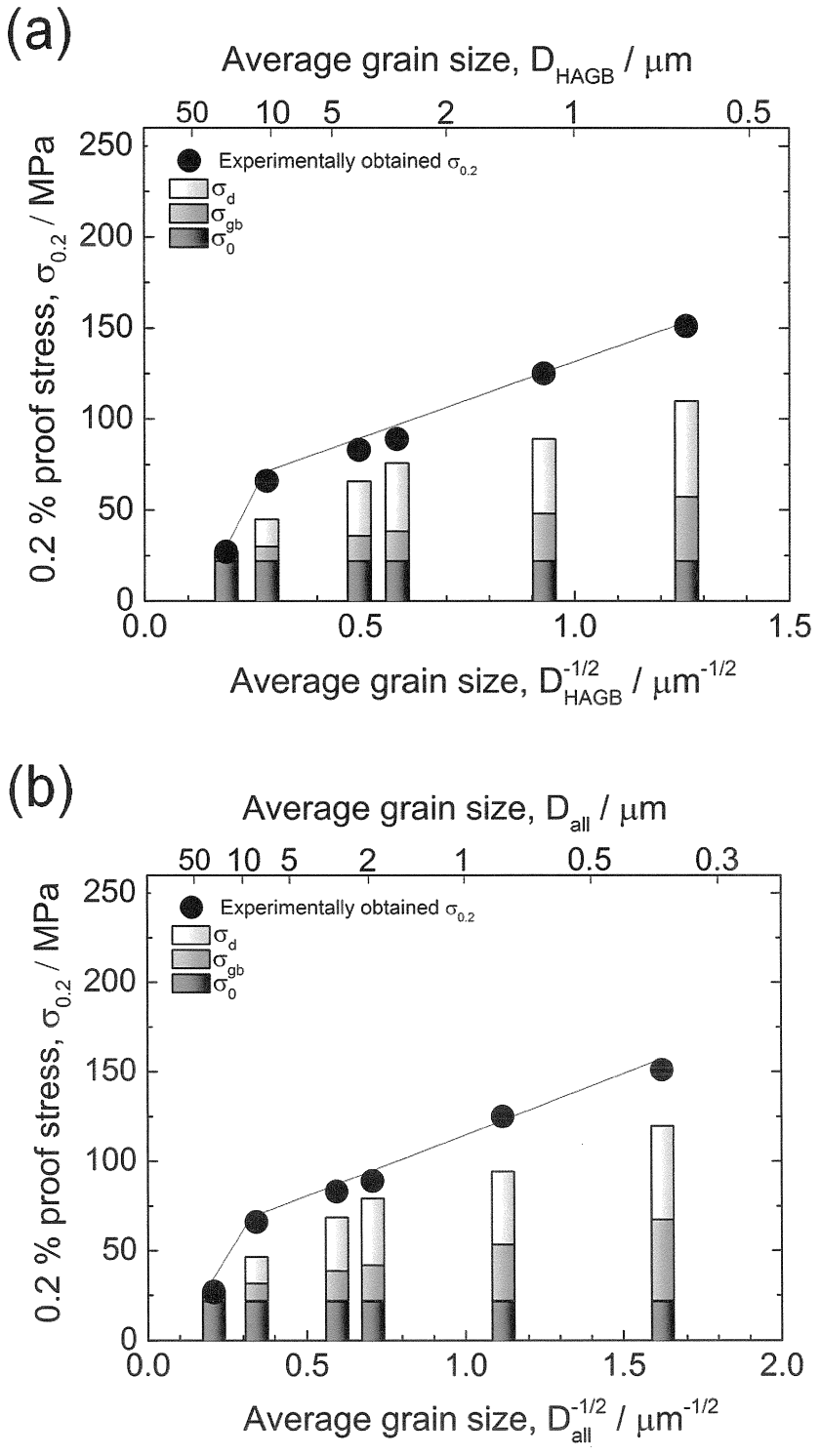

Fig. 3.7 A comparison between the experimental and the calculated values of the 0.2% proof stress. Plotted for two kinds of mean grain sizes shown in Table 2: (a) D_{HAGB} and (b) D_{all}.

3.4 Conclusions

In the present chapter, mechanical properties and microstructures of the ultrafine grained aluminum fabricated by torsion deformation were systematically investigated. The strengthening mechanisms of the ultrafine grained aluminum were also discussed. The main results obtained are as follows:

1. The various fine grain structures having mean grain sizes ranging from 0.38 μm to 8.6 μm were obtained by torsion deformation under various Z conditions. The ultrafine grained microstructures involved high density of dislocations. The mean grain size decreased and the dislocation density increased with increasing the Z value.

2. The strength of the torsion deformed specimens increased with increasing the Z value. The ultrafine grained aluminum having submicrometer grain sizes exhibited very high strength. On the other hand, the tensile ductility of the submicro-meter grained aluminum was limited due to early plastic instability.

3. The 0.2 % proof stress of the ultrafine grained aluminum was much higher than that predicted by conventional Hall-Petch relationship of aluminum extrapolated from coarse grained regions. The extra hardening behavior of the torsion deformed aluminum was significantly different from that of the ARB processed and annealed aluminum. The 0.2% proof stress of the torsion specimens was evaluated from the microstructural parameters experimentally obtained, and compared with the 0.2% proof stress obtained by tensile test. It was concluded that the extra hardening in the torsion specimens was attributed mainly to the substructure strengthening.

References

[1] Meyers MA, Mishr A and Benson DJ
Mechanical properties of nanocrystalline materials.
Pro Mater Sci (2006) 51:427-556.

[2] Mcqueen HJ, Spigerelli S and Kassner ME
Hot deformation and processing of aluminum alloys.
Taylor & Francis Group, (2011) :59.

[3] Hall EQ
The deformation and ageing of mild steel: III discussion of results.
Acta Mater (1951) 64:747-753.

[4] Petch N
The fracture of metals.
Pro Metal Phy (1954) 5:1-52.

[5] Tsuji N, Ito Y, Saito Y and Minamino Y
Strength and ductility of ultrafine grained aluminum and iron produced by ARB and annealing.
Scripta Mater (2002) 47:893-899.

[6] Yu CY, Kao CK and Chang CP
Transition of tensile deformation behaviors in ultrafine-grained aluminum.
Acta Mater (2005) 53:4019-4028.

[7] Masumura R, Hazzledine PM and Pande CS
Yield stress of fine grained materials.
Acta Mater (1998) 46:4527-4534.

[8] Sanders PG, Eastman J and Weertman JR
Elastic and tensile behavior of nanocrystalline copper and palladium.
Acta Mater (1997) 45:4019-4025.

[9] Chokshi AJ and Rosen A
On the validity of the hall-petch relationship in nanocrystalline materials.
Scripta Metall (1989) 23:1679-1684.

[10] Kamikawa N, Huang X, Tsuji N and Hansen N
Strengthening mechanisms in nanostructured high-purity aluminium deformed to high strain and annealed.
Acta Mater (2009) 57:4198-4208.

[11] Williamson GK and Hall WH
Discussion of the theories of line broadening.
Acta Mater (1953) 1:22-31.

[12] Williamson GK and Smallman RE
Dislocation densities in some annealed and cold-worked metals from measurements on the x-ray debye-scherrer spectrum.
Philo Mag (1956)1:37-41.

[13] Huang X, Hansen N and Tsuji N
Hardening by annealing and softening by deformation in nanostructured metals.
Science (2006) 312:249-251.

[14] Kamikawa N (2005)
Grain refinement of structural metallic materials by accumulation roll bonding.
Ph.D. Thesis, Osaka University.

[15] Huang X, Kamikawa N and Hansen N
Strengthening mechanisms in nanostructured aluminum.
Mater Sci Eng A (2008) 483:102-104.

[16] Ueji R, Tsuji N, Minamino Y and Koizumi Y
Effect of rolling reduction on ultrafine grained structure and mechanical properties of low-carbon steel thermomechanically processed from martensite starting structure.
Sci Tech Adv Mater (2004) 1-2:153-162.

[17] Gao S, Chen M, Kamikawa N, Shibata A and Tsuji N
Recent thoughts on yield point phenomenon, "extra-hardening" and hall-petch relationship in metals.
submitted to Mater Trans (2013).

[18] Callister WD and Rethwisch DG (2007)
Materials science and engineering: dislocation and strengthening mechanisms.
New York Wiley 197-233.

[19] Hansen N, Huang X, Ueji R and Tsuji N
Structure and strength after large strain deformation.
Mater Sci Eng A (2004) 387-389:191-194.

[20] Gubicza J, Dirras G, Szommer P and Bacroix B
Microstructure and yield strength of ultrafine grained aluminum processed by hot isostatic pressing.
Mater Sci Eng A (2007) 458:385-390.

[21] Hansen N and Huang X
Microstructure and flow stress of polycrystals and single crystals.
Acta Mater (1998) 46:1827-1836.

Chapter 4 Effects of deformation conditions and precipitates on microstructure evolution in Al-2wt.% Cu heavily deformed by torsion

4.1 Introduction

It has been shown in the previous chapters that torsion deformation is one of the promising severe plastic deformation processes for producing bulk ultrafine grained materials. The torsion deformation has the advantage in accurate control of deformation conditions and also allows a continuous impose of the strain without interruption, compared with other severe plastic deformation (SPD) processes. It has been confirmed in **Chapters 2 and 3** that the microstructure and mechanical properties of the commercial purity aluminum are strongly dependent on the deformation conditions (i.e. strain, strain rate and deformation temperature).

Recently, several researchers have reported that the grain refinement and mechanical properties of two phase materials deformed by SPD processes are greatly different from those of single phased materials [1, 2]. However, the influence of second phases (or precipitates) on grain refinement of Al alloys during SPD has not yet been fully studied. In the present chapter, the author systematically investigates the effect of precipitates on microstructural evolution in aluminum alloy deformed by torsion deformation under various conditions, i.e., equivalent strains, deformation temperatures and stain rates. The microstructure and mechanical properties of the commercial purity aluminum during torsion deformation reported in **Chapter 2**, were used as reference results for discussing the effects of chemical composition and precipitates on microstructure and mechanical properties of Al-2wt.% Cu alloy studied in this chapter.

4.2 Experimental procedure

4.2.1 Aging behavior of Al-2wt.% Cu alloy

The material used in the present chapter was an Al-2wt.% Cu alloy. The chemical composition of the Al-2wt.% Cu alloy is listed in **Table 4.1**.

Table 4.1 The chemical composition of the Al-2wt.% Cu alloy (wt. %)

Cu	Fe	Si	Mn	Zn	Ti	Mg	Al
1.935	0.022	0.004	0.001	0.001	0.000	0.001	Bal.

The torsion specimens 8 mm in gage diameter and 4 mm in gage length were machined from as-received Al-2wt.% Cu alloy bars. The details of the dimension and shape of the torsion specimens were schematically shown in **Fig. 2.1 (a).** The torsion specimens were first solution-treated (ST) at 550 °C for 1 h, followed by water quenching, and then immediately aged in an oil baths at three different temperatures (150 °C, 170 °C, and 180 °C) for various periods up to 1080 ks (300 h). The temperatures of the oil bath were precisely controlled within ±1 °C for each aging temperature. The aging procedure is schematically presented in **Fig. 4.1**.

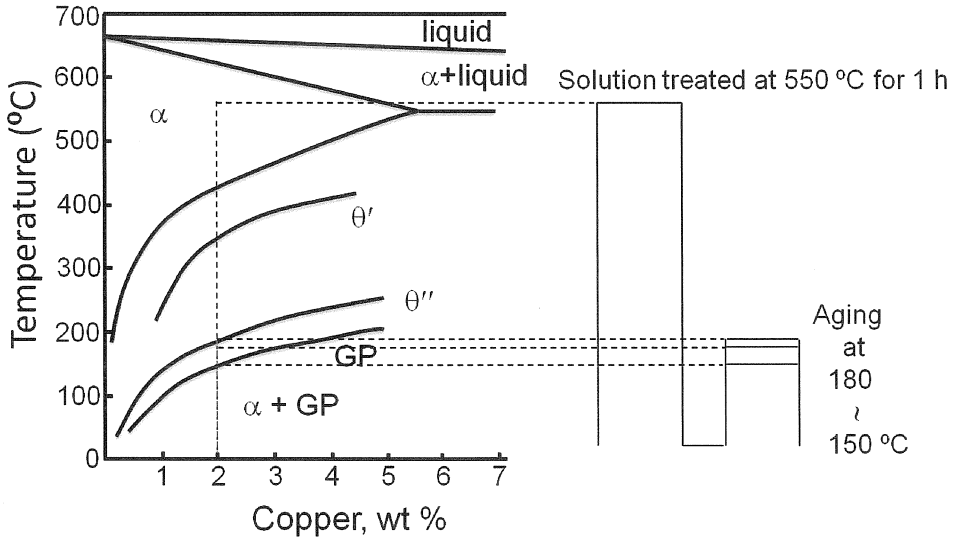

Fig. 4.1 Schematic illustration showing the aging procedure of the Al-2wt.% Cu alloy.

4.2.2 Effect of strain on microstructure evolution in Al-2 wt.% Cu alloy

For preparation, the torsion specimens were first solution-treated (ST) at 550 °C for 1 h, followed by water quenching to room temperature. Some ST-specimens were immediately aged at 180 °C for 360 ks (100 h) to obtain θ′ precipitates [3]. The aged condition was designed according to a preliminary experiment. Both ST and aged specimens were used as starting materials for clarifying the microstructural evolution during torsion deformation of the Al-2%.wt Cu alloy. The ST and aged specimens were deformed by torsion at room temperature under a constant strain rate of 1 s^{-1} to various equivalent strains (0-4). The torsion deformation procedures for the ST and aged specimens are schematically illustrated in **Fig. 4.2 (a)** and **(b)**, respectively.

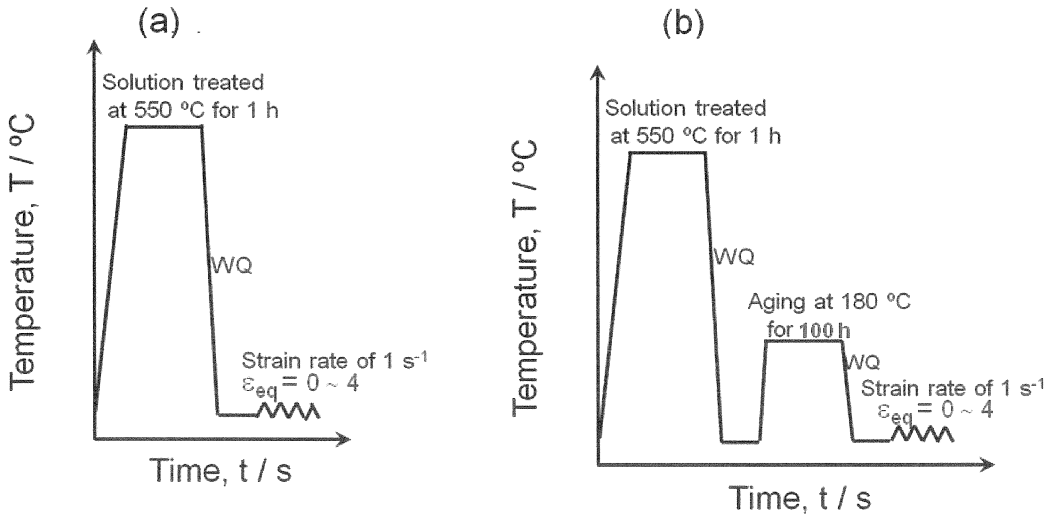

Fig. 4.2 The torsion deformation procedures of (a) ST specimens and (b) aged specimens.

4.2.3 Effects of strain rate, deformation temperature and pre-exiting precipitates (θ′) on microstructural evolution of Al-2wt.% Cu alloy

In order to study the influence of strain rate, deformation temperature and pre-existing θ′ precipitates on microstructure evolution of the Al-2wt.% Cu alloy, the aged specimens were deformed at five different temperatures and three different strain rates to the equivalent strains of 4 to 36 as shown in **Fig. 4.3**. The aged specimens were firstly heated by an induction heating system in the torsion-type thermomechanical processing simulator at a heating rate of 10 °C s^{-1} to the various deformation temperatures (100, 200, 300 and 400 °C), and held for 300 s before the torsion deformation to make the temperature in the specimens homogeneous. The holding time for 300 s at the deformation temperatures mentioned above were short enough to prevent the microstructure modifications. After holding for 300 s, the torsion deformation was carried out at three different strain rates (10^{-2}, 10^{0} and 10^{2} s^{-1}) to equivalent strains of 4 and 36 at the gage surface (corresponding to 1.1 and 10 rotations, respectively), then the hot deformed specimens were immediately quenched by water, at a cooling rate of approximately 200 °C s^{-1}. In addition, the aged specimens were also deformed at room temperature at various strain rates mentioned above to equivalent strains of 4 and 36. In this study, the stress and stain data were computed from the torque (moment) and angular displacement data recorded during the torsion deformation using the equations 2.3 and 2.4, respectively.

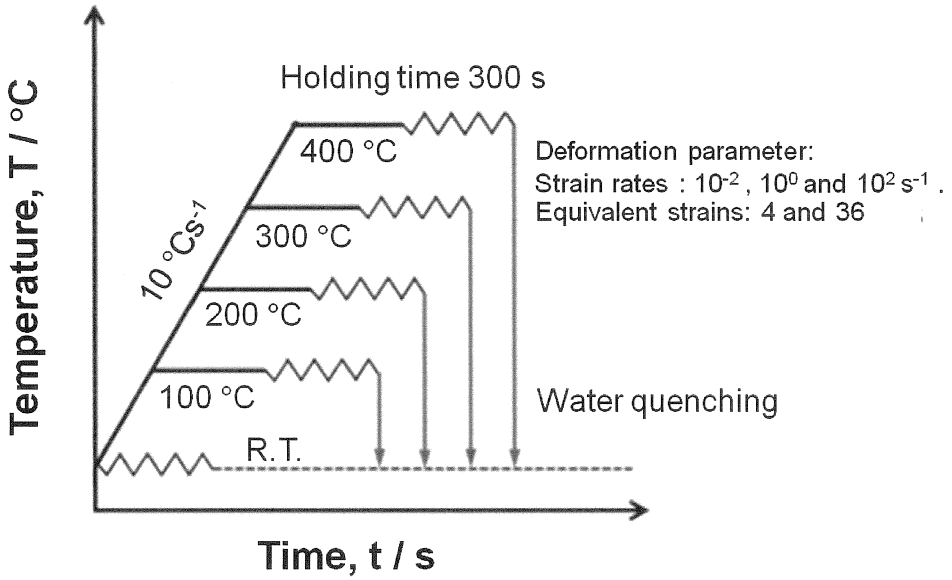

Fig. 4.3 Schematic illustration of the torsion deformation procedure used in this chapter.

4.2.4 Microstructure observation

In this study, microstructures of the ST and Aged specimens after torsion deformation were characterized by scanning electron microscopy (SEM) using field-emission type SEM (Philips XL30S-FEG) equipped with electron backscatter diffraction (EBSD) system operated at 15 kV and by transmission electron microscopy (TEM, JEOL-2000EX) performed at 200 kV. Microstructure observations were carried out on the sections parallel to the torsion axis and the shear direction and at a radial position of 0.9R (R: radius of the gage part), as illustrated in **Fig. 4.4**. The sections for EBSD observation were polished mechanically and followed by electro-polishing at -30 °C at a voltage of 12 V in a 300 ml HNO_3 + 700 ml CH_3OH solution. For TEM analysis, thin-foil specimens were prepared by twin-jet electo-polishing under the same conditions as those for the EBSD observation.

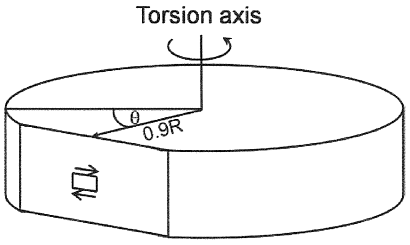

Fig. 4.4 Schematic illustration showing the section for microstructure observation. The parallel arrows indicate the shear direction in torsion.

4.2.5 Hardness test

The hardness of the torsion deformed specimens was determined by Shimadzu micro-hardness tester equipped with Vickers indenter using 1 kgf load with dwell time of 10 s at room temperature. The hardness test was carried out at the same position with that for the microstructure observation (**Fig. 4.4**).

4.3 Aging behaviors

Firstly, the aging behaviors of the Al-2wt%Cu alloy were preliminarily examined before the torsion tests.

4.3.1 Hardness changes during aging

Figure 4.5 illustrates the hardness of the ST specimens of the Al-2wt.% Cu alloy as a function of aging time at 150 °C, 170 °C and 180 °C. The ST specimen had a relatively low hardness of 37 HV. In order to understand the aging behavior of the Al-2wt.% Cu alloy at wide temperature ranges, the hardness data of the same material aged at 190 °C reported by Tsuji et al. were also plotted in this figure [4]. It is clearly seen from **Fig. 4.5** that the hardness is strongly dependent on the aging temperature and time. At aging temperature of 150 °C, the change of the hardness with the aging time is fairly

slow and no significant change in hardness happens even after 360 ks (100 h) aging. By increasing the aging temperature to 170 °C, the different hardness behavior is observed. That is, the hardness slightly increases with increasing aging time at the early stage of aging ($t < 10^4$ s), and then significantly increases with further increasing the aging period. However, it should be noted here that the hardness tends to increase continually even after long aging time (15 days). By further increase in aging temperature to 180 °C, the hardness increases slowly at the early stage of aging, followed by a significant increases between 10^4 to 10^5 s, and reaches the maximum hardness of 65.95 HV at 360 ks (100 h). Then the hardness decreases with further increase of aging time. The hardness reaches almost 1.7 times higher value than that of the as-ST specimen after 180 °C aging. It is also found that the maximum hardness decreases with increasing the aging temperature. Meanwhile, the time to reach the maximum hardness decreases with increasing the aging temperature. These results are well consistent with the previous reports of the similar material in the literatures [5]. The increase in hardness of the aged Al-2wt.% Cu alloy specimens is attributed to the formation of precipitates during the aging process [4-6]. Meanwhile, the decrease in hardness after the peak hardness is generally known as over aging [4-6]. Based on the experimental data, the specimens aged at 180 °C for 360 ks, which show the peak hardness of HV 65.95, are used as the Aged specimens for studying the influence of precipitate on the development of microstructure and mechanical properties during torsion deformation.

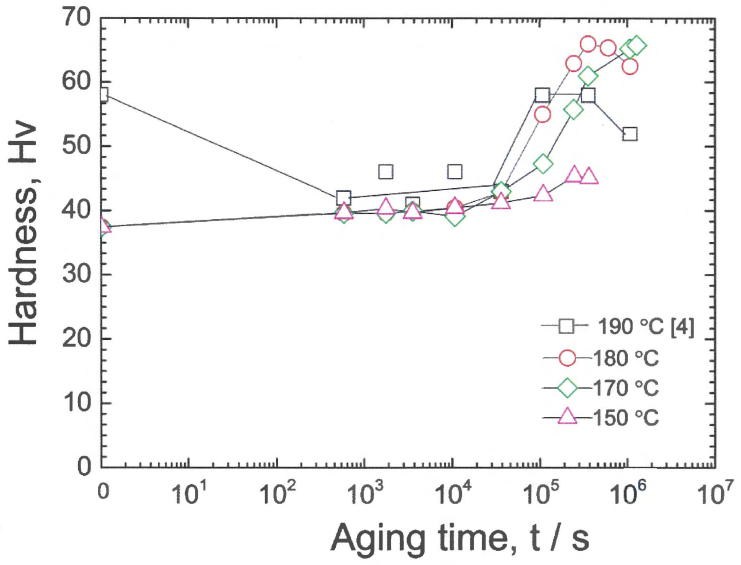

Fig. 4.5 Change in hardness of the Al-2wt.% Cu alloy aged at different temperatures.

4.3.2 Change in microstructures during aging

The EBSD grain boundary maps showing microstructures of the as-ST specimen and the specimen subsequently aged at 180 °C for 360 ks (100 h) are shown in **Fig. 4.6 (a)** and **(b)**, respectively. In the figures, the black and red lines represent high angle grain boundaries ($\theta \geq 15°$, θ: misorientation) and low angle grain boundaries ($2 \leq \theta < 15°$), respectively. Boundaries having misorientation below 2° were removed because of the inaccuracy in EBSD measurement and analysis. It is found that the ST specimen had a fully recrystallized microstructure with a mean grain size of 323 μm and a fraction of high angle grain boundary of 0.84 as shown in **Fig. 4.6 (a)**. The specimen aged at 180 °C for 360 ks shows a similar microstructure to the as-ST specimen (**Fig. 4.6 (b)**). That is, the microstructure comprises of the equaixed grain structure having the mean again size of 332 μm. These results indicate that at this aging temperature (180 °C) the matrix grain structure does not change significantly.

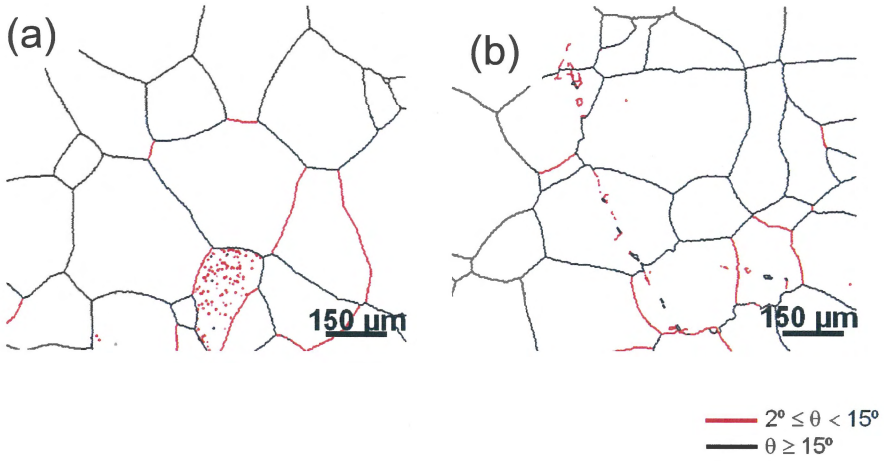

Fig. 4.6 EBSD grain boundary maps of (a) the as-ST specimen and (b) the specimen aged at 180 °C for 360 ks.

In order to observe the precipitation microstructure of the specimen aged at 180 °C for 360 ks at the peak hardness, TEM observation was carried out. The TEM image and corresponding selected area electron diffraction (SAED) of the specimen aged at 180 °C for 360 ks are shown in **Fig. 4.7 (a)** and **(b)**, respectively. It is found that the microstructure shows thin-plate precipitates aligned along particular directions. The SAED pattern in **Fig. 4.7 (b)** related to the area of **Fig. 4.7 (a)** was taken with the electron beam parallel to 110. The SAD pattern indicates that these precipitates are θ′ in Al-Cu alloys, as the 110 θ′ diffraction spots are clearly seen in the SAD pattern [5]. The θ′ phase (Al_2Cu) is a semi coherent precipitate in Al-Cu alloys, which has a body-centered tetragonal structure [7]. The average sizes of the precipitates were 420 nm in length and 7 nm in width. The θ′ plates were parallel to {100} planes of Al matrix. These results indicate that the increase in hardness during 180 °C aging heat treatment of the present Al-2wt%Cu alloy results from the formation of the θ′ precipitates.

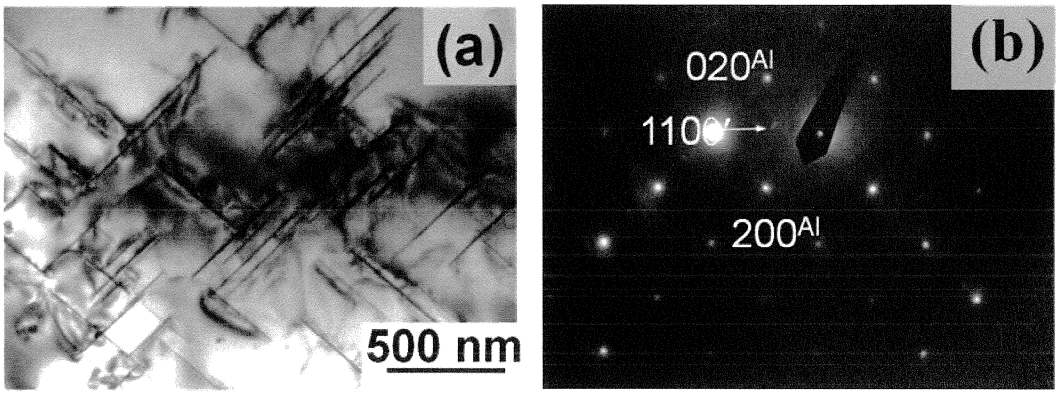

Fig. 4.7 (a) A TEM micrograph and (b) corresponding selected area electron diffraction (SAED) pattern of the specimens aged at 180 ℃ for 360 ks.

4.3.3 Summary

The aging behavior of the Al-2wt.% Cu alloy has been investigated at the temperature range from 150 ℃ to 180 ℃. The results are listed below:

1. The hardness was strongly dependent on the aging temperature and time. The maximum hardness decreased and the time to reach the maximum hardness decreased with increasing the aging temperature. The maximum hardness of HV 65.95 was achieved after the aging at 180 °C for 360 ks.

2. The nano sized θ′ plate precipitates were observed in the specimen aged at 180 °C for 360 ks.

4.4 Torsion deformation at RT

4.4.1 Microstructure evolution

Figure 4.8 shows grain boundary maps of the ST specimens deformed to various equivalent strains by torsion at a strain rate of 1 s^{-1} at RT. Here, the grain boundaries are distinguished by two different colors according to the misorientation angle, θ. The red and black lines indicate the low-angle grain boundary ($2 \leq \theta < 15°$) and high-angle grain boundary ($\theta \geq 15°$), respectively. The microstructure of the ST specimen before torsion deformation is also shown in this figure. The initial ST specimen had a fully recrystallized structure having a mean gain size of 323 μm as shown in **Fig. 4.8 (a)**. It is obviously demonstrated that the grain subdivision takes place with increasing imposed strain. After low equivalent strain of 0.2, the original grains are subdivided by some low angle grain boundaries (**Fig. 4.8 (b)**). After equivalent strain of 0.82, the large amount of low angle grain boundaries are observed (**Fig. 4.8 (c)**). By increasing the imposed equivalent strain to 1.63, the ultrafine grained structure with a mean (sub)grain size of about 0.53 μm is observed **(Fig. 4.8 (d))**. However, most of the (sub)grains are surrounded by low angle grain boundaries. In addition, microstructures of the specimens deformed to equivalent stain below 2 are inhomogeneous where some regions include relatively high density of low angle grain boundaries but the other regions show the remaining original grains with deformation substructures. This may be due to the relatively coarse grain size (323 μm) in the starting specimen. With further increasing the equivalent strain to 3.6, the amount of fine grains with high angle grain boundaries significantly increases, and the microstructure becomes more homogeneous throughout the specimen (**Fig. 4.8 (e)**). The average grain size of this microstructure was 0.26 μm and the fraction of high-angle grain boundaries was 44%.

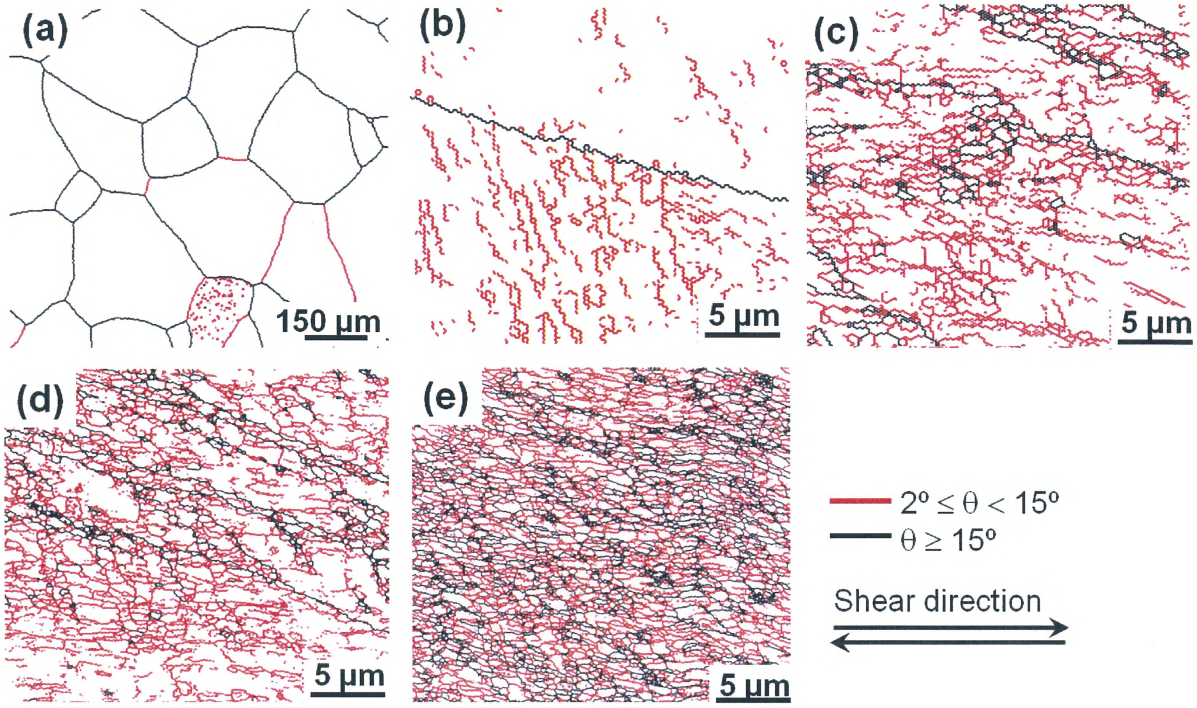

Fig. 4.8 EBSD boundary maps of the ST specimens of Al-2wt.% Cu alloy torsion deformed to various equivalent strains (ε_{eq}) at RT: (a) undeformed material, (b) ε_{eq} = 0.2, (c) ε_{eq} = 0.82, (d) ε_{eq} = 1.63 and (e) ε_{eq} = 3.6.

Figure 4.9 (a)-(e) show the grain boundary maps of the aged specimens torsion deformed to various equivalent strains at a strain rate of 1 s^{-1} at RT. **Figure 4.9 (a)** shows that the undeformed aged-specimen consists of equiaxed grains having an average grain size of 332 µm. After equivalent strain of 0.2, original grains are subdivided by relatively small amount of low angle grain boundaries (**Fig. 4.9 (b)**). With increasing the imposed strain to 0.82, the amount of low-angle grain boundaries increases significantly (**Fig. 4.9 (c)**). Also some ultrafine grains surrounded by high-angle boundaries are observed, which are aligned along the initial grain boundaries. With further increase in the imposed strain, the fine and elongated grains were formed

(**Fig. 4.9 (d)**). However, most of the grains are surrounded by low angle grain boundaries. It is clearly seen from **Fig. 4.9 (b)-(d)** that the microstructures of the specimens deformed to equivalent strain below 2 are inhomogeneous. The ultrafine grained structure was observed after equivalent strain of 3.6 (**Fig. 4.9 (e)**). The amounts of fine grains having high angle boundaries increased but most of the observed boundaries are low-angle ones. The fraction of high-angle grain boundaries and the mean (sub)grain size in **Fig.4.9(e)** are 37 % and 0.28 μm, respectively.

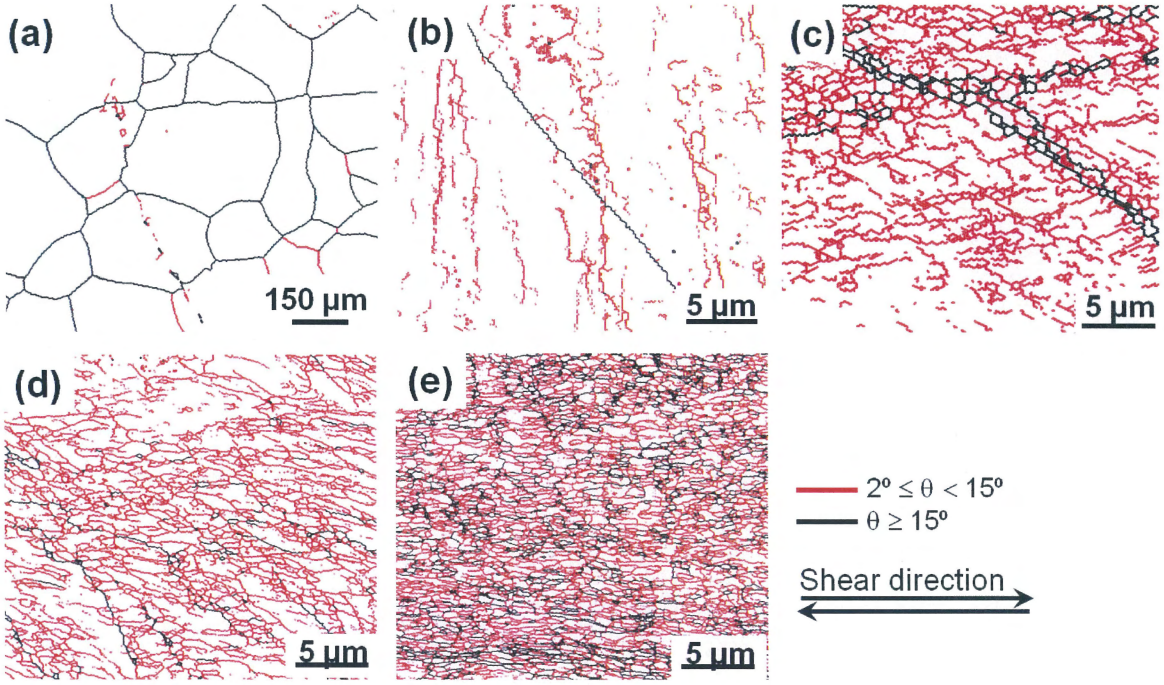

Fig. 4.9 EBSD boundary maps of the aged specimens of Al-2wt.% Cu alloy torsion deformed to various equivalent strains (ε_{eq}) at RT: (a) undeformed material, (b) ε_{eq} = 0.2, (c) ε_{eq} = 0.82, (d) ε_{eq} = 1.63 and (e) ε_{eq} = 3.6.

In order to clarify more detailed deformation microstructures, TEM observation was conducted to the aged specimens after torsion deformation. **Figure 4.10** shows TEM micrographs of the aged specimens deformed to various equivalent strains at RT. The TEM micrograph of the undeformed specimen is also presented in this figure. The

microstructure of the undeformed specimen is composed of θ′ precipitates having plate morphologies 420 nm in average length and 7 nm in average width (**Fig. 4.10 (a)**). The average inter-precipitates distance is 126 nm. After equivalent strain of 0.2, large amount of dislocations were accumulated nearby θ′ precipitates (**Fig. 4.10 (b)**). Increase in equivalent strain to 0.82 results in the increase in the amount of dislocations and the formation of fine lamellar structures (**Fig. 4.10 (c)**). Those fine lamellar structures are divided by θ′ precipitates. In addition, at this imposed strain, most of the θ′ plate precipitates were fragmented by shear deformation. After further increase in imposed strain to 3.26, the microstructure is composed of highly elongated lamellar boundary structures with straight morphologies. The structure is again subdivided by very thin θ′ plates. The mean interval of the lamellas measured in TEM images was 89 nm. It was also seen that the lamellar size decreased with increasing imposed strain.

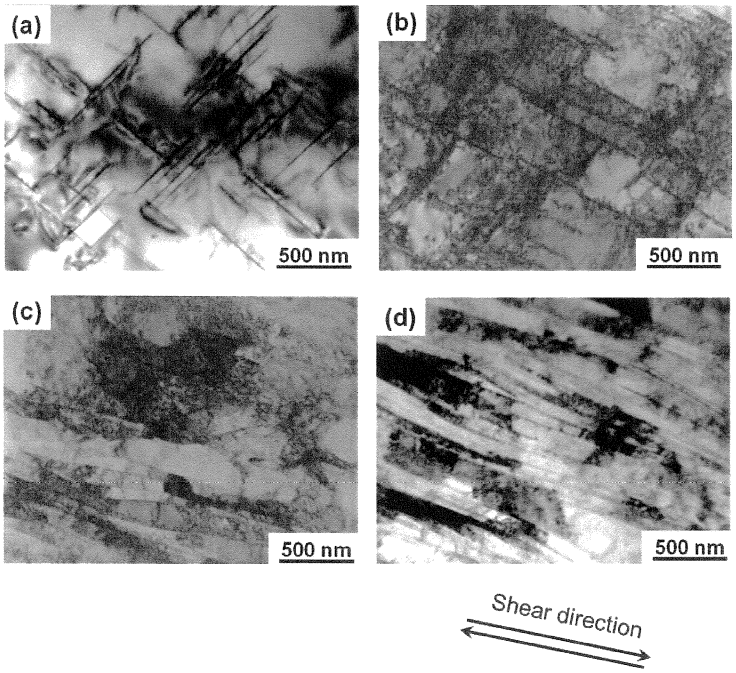

Fig. 4.10 TEM microstructures of the aged specimens torsion deformed to various equivalent strains (ε_{eq}) at RT: (a) undeformed material, (b) ε_{eq} = 0.2, (c) ε_{eq} = 0.82, (d) ε_{eq} = 1.63 and (e) ε_{eq} = 3.6.

The changes of the grain size (D_{all}) and the fraction of high angle grain boundary (F^{HAGB}) with increasing imposed equivalent strain of the ST and aged Al-2wt.% Cu alloy deformed by torsion at RT are summarized in the **Fig. 4.11 (a)** and **(b),** respectively. In this plot, the mean grain size was measured from all grain boundaries having the misorientaion above 2° using line intercept method. The mean grain size and the fraction of high angle grain boundary of the 1100 commercial purity Al deformed under the same deformation conditions, which were shown in **Chapter 2**, were also plotted in **Fig. 4.11** for comparison. It is apparent in **Fig. 4.11 (a)** that the mean grain size of the torsion deformed ST and aged Al-2wt.% Cu alloy specimens exhibit the similar trend to the torsion deformed 1100Al specimens. That is, the grain size rapidly decreases to below 1 μm at equivalent strain below 1, and then slightly decreases with increasing imposed strain. However, observing the change in **Fig. 4.11 (a)** carefully (see the insert), it is found that at similar equivalent strains the grain sizes of the ST and aged Al-2wt.% Cu alloy specimens are finer than that of the 1100Al specimens. Meanwhile, it was found that the fraction of high angle grain boundaries in the aged Al-2wt.% Cu alloy specimens are significantly lower than that of the 1100Al and ST Al-2wt.% Cu alloy specimens deformed under the same equivalent strains. In addition, the fraction of high angle grain boundaries in the ST specimens is also lower than that of the 1100Al specimens. The average (sub)grain size and fraction of high angle boundaries obtained from the EBSD data are summarized in **Table 4.2**.

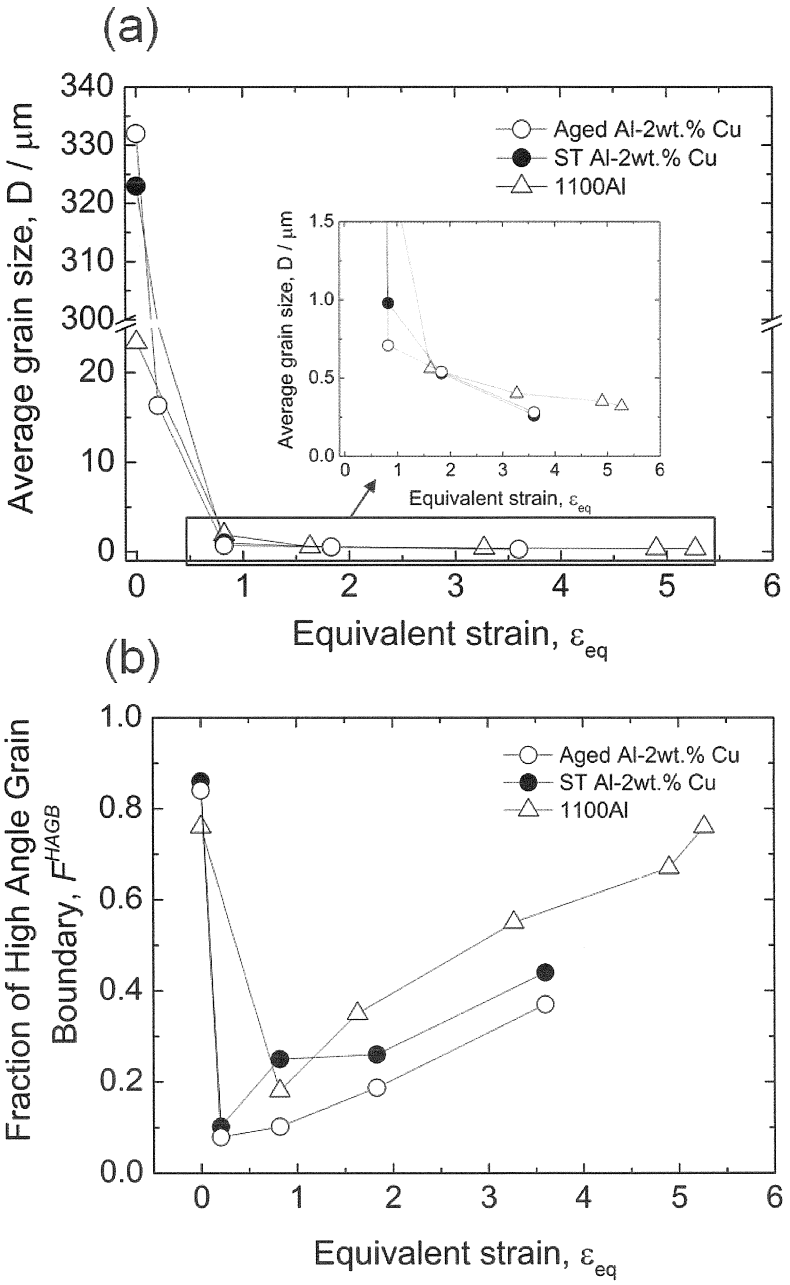

Fig. 4.11 (a) Average grain size (D_{All}) and (b) fraction of high angle boundaries (F^{HAGB}) in the ST and aged Al-2wt.% Cu alloy specimens deformed by torsion at RT. Plotted as a function of equivalent strain. The data of the 1100 commercial purity Al obtained in **Chapter 2** are also shown.

Table 4.2: Summary of the microstructural parameters of the ST and aged Al-2wt.% Cu alloy specimens torsion deformed to various equivalent strains at RT, where D_{All} is the average (sub)grain size taking account of all boundaries having misorientation above 2 °, and D_{HAGB} is the mean grain size obtained from high angle grain boundaries ($\theta \geq 15°$). The microstructure parameters of 1100Al specimens deformed under the similar deformation conditions are also included in the table.

Material	Equivalent strain (at 0.9R)	Average grain size (μm)		Fraction of high angle boundaries, F^{HAGB}
		D_{All}	D_{HAGB}	
ST Al-2wt.% Cu	0	323.00	338.00	0.86
	0.2	25.26	25.00	0.102
	0.82	0.98	12.80	0.25
	1.63	0.53	9.86	0.26
	3.27	0.26	5.24	0.44
Aged Al-2wt.% Cu	0	332.00	342.00	0.84
	0.2	16.30	66.66	0.08
	0.82	0.71	56.67	0.10
	1.63	0.54	25.16	0.19
	3.27	0.28	7.56	0.37
1100Al	0	23.4	28.0	0.76
	0.82	1.94	6.29	0.18
	1.63	0.56	1.86	0.35
	3.27	0.40	0.46	0.55
	4.90	0.35	0.36	0.67
	5.27	0.32	0.33	0.76

Here, let's compare the microstructure evolution in the aged Al-2wt.% Cu alloy specimens with those in the ST Al-2wt.% Cu alloy specimens and 1100Al deformed under the similar deformation conditions by torsion deformation. It is found that the microstructures in the ST and aged Al-2wt.% Cu alloy specimens after torsion deformation were greatly different from that of the 1100Al specimen. That is, the grains

formed were fairly fine and elongated and most of the grains were surrounded by low angle grain boundaries in the Al-Cu alloy. Meanwhile the microstructure of the torsion deformed 1100Al was rather equixed and most of the grains were surrounded by high angle grain boundaries (**Fig. 2.4**). It was also found that the mean grain size of the ST Al-2wt.% Cu alloy specimen was finer than that of the 1100Al deformed under the same deformation conditions. These results suggest that the solute atoms (Cu) significantly influence the microstructure evolution during SPD process. The solute atoms inhibit the dynamic recovery during SPD. They might be effective to refine the grain size through grain subdivision. Similar results have been reported in Al-2wt.% Cu alloy in the literatures [4]. On the other hand, under the same deformation conditions, the aged specimen also showed different microstructures from the ST and 1100Al specimens. That is, the microstructure of the aged specimen was composed of highly elongated fine (sub)grains. It has been reported in Al-Cu alloy that the presence of fine and plate-shaped precipitates inhibits the development of high-angle grain boundaries and the formation of fine grain structures during SPD [2, 7]. It is believed that the dispersion of fine plate-shaped precipitates homogenize the slip and inhibit the formation of shear bands during deformation to retard the evolution of ultrafine grained structures surrounded by high angle grain boundary [2].

4.4.2 Hardness change during torsion

Figure 4.12 illustrates the hardness of the ST and aged Al-2wt.% Cu alloy specimens plotted as a function of the equivalent strains imposed by torsion. The data of the 1100Al are also shown in the figure for comparison. It can be clearly seen from **Fig. 4.12** that the initial hardness of the aged specimen is greatly higher than that of the

ST and 1100Al specimens. The higher hardness of the aged specimen is attributed to precipitation hardening. It is also found that the hardness of the ST specimen after equivalent stain of 0.2 is drastically enhanced to 68 HV, which is nearly two times higher than that of the non-deformed ST specimen. After equivalent strain of 0.2, the hardness gradually increases with increasing the equivalent strain. The aged and 1100Al specimens show the similar results with the ST. That is, the hardness increases with increasing the equivalent strain. However, comparing the hardness of the aged specimens with that of the ST specimens and 1100Al deformed at the similar strains, it is found that the increasing rate of the hardness in the age specimens is greatly higher than that of the 1100Al specimens, but it is significantly lower than that of the ST specimens, especially at the early stage of plastic deformation less than ε_{eq} = 0.2. Similar results have been reported by Maya et al. [2] in Al-1.7 at.% Cu alloy deformed by ECAP process. It can be concluded, therefore, that the solute-atom enhances the work hardening rate in the Al-2wt.% Cu alloy rather than θ′ precipitates.

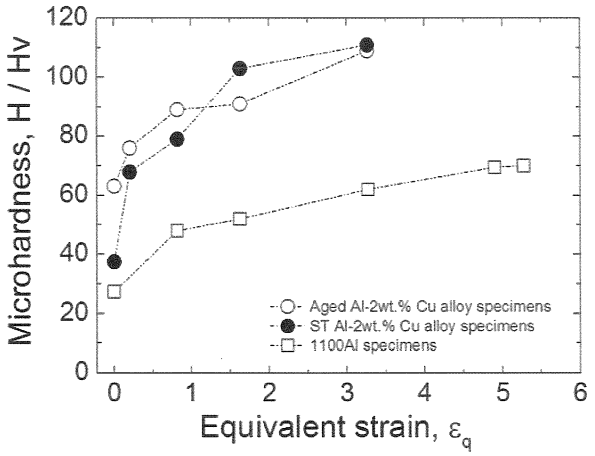

Fig. 4.12 Hardness change in the Al-2wt.% Cu alloy as a function of equivalent strain imposed by torsion at RT. Results of the 1100 Al are also shown.

4.4.3 Summary

The evolution of microstructures in the Al-2wt.% Cu alloy specimens during torsion deformation at room temperature has been investigated. The main results obtained are as follows:

1. The grain size of the ST and aged Al-2wt.% Cu alloy specimens tended to decrease with increasing equivalent strain in torsion deformation. However, the mean grain size of the Aged specimens after equivalent strain of 3.27 was finer than that of the 1100Al specimens, but slightly larger than the ST specimens. The fractions of high-angle grain boundaries in the aged specimens were significantly lower than that of the ST and 1100Al specimens deformed under the similar conditions. The presence of fine θ′ precipitates with plate morphologies inhibited the development of high angle grain boundaries and the formation of the fine grain structure during SPD.

2. The θ′ plate precipitates was fragmented into the nano precipitates by localized shear, and fine and elongated lamellar structures divided by the θ′ precipitates developed in the matrix.

3. The hardness of the ST and aged Al-2wt.% Cu alloy specimens increased with increasing equivalent strain. The increasing rate of the hardness in the aged specimen was higher than the 1100Al, but significantly lower than the ST specimens. The solute-atom enhanced work hardening rate in the Al-2wt.% Cu alloy than θ′ precipitates.

4.5 Effect of deformation conditions on microstructure evolution in Al-2%Cu alloy

The influence of the precipitate on the formation of ultrafine grained structure at RT in the Al-2wt.% Cu alloy is systematically studied in the section 4.4. In this part, the effects of deformation temperature and strain rate on the evolution of microstructure and mechanical properties of the aged Al-2wt.% Cu alloy will be clarified.

4.5.1 Stress-strain behaviors

Figure 4.14 shows the stress-strain curves of the aged-specimens of Al-2wt.% Cu alloy torsion deformed at three different strain rates (10^{-2} s^{-1} to 10^{2} s^{-1}) and five different deformation temperatures (RT to 400 °C). It is found that the flow stress increases with decreasing deformation temperature and increasing strain rate, which is generally observed in hot deformation of metals including aluminum alloys. It is also observed that the total elongation increases with increasing deformation temperature up to 100 °C, then significantly decreases at 200 °C, and after that gradually increases with further increasing deformation temperature. This is significantly different from the 1100Al specimens deformed under the similar deformation conditions (see **Fig. 2.10** in **Chapter 2**). That is, in the 1100Al, the total elongation gradually increases with increasing deformation temperature. In addition, it was observed that the Al-2wt. % Cu alloy specimens deformed under these deformation conditions showed two different types of stress-strain curves, depending on the deformation parameters. Firstly, the specimens deformed at low temperature (below 200 °C) at all strain rates and those at 200 °C at strain rates of 10^{0} and 10^{2} s^{-1} show simple work hardening. The flow stress increases with increasing strain until the maximum stress followed by fracture. Secondly, in the specimens torsion deformed at temperatures higher than 300°C, the

flow stress increases rapidly with increasing strain, then reaches to the maximum stress at relatively low strains, and thereafter dynamic softening is seen at high strains. In **Fig. 4.14**, the steady state flow stress after dynamic softening was also observed in the specimens deformed at 400 °C. The results reveal that the flow stress and shape of the flow curves are strongly dependent on the deformation conditions. These results were similar to those of the 1100Al, reported in **Chapter 2**. However, comparing the stress-strain curves of the aged Al-2wt.% Cu alloy with those of the 1100Al, it is found that the shape of the stress–strain curves in the aged Al-2wt.%Cu alloy specimens are greatly different from those of 1100Al under the same deformation parameters, especially at high temperatures. That is, the softening of flow curves in the aged Al-2wt.% Cu alloy specimens is clearer than that in the 1100Al specimens. The results indicate that the pre-exsiting θ′precipitate has a strong effect on the stress-strain behaviors. The reason for the large drop of the flow stress will be discussed in the next section.

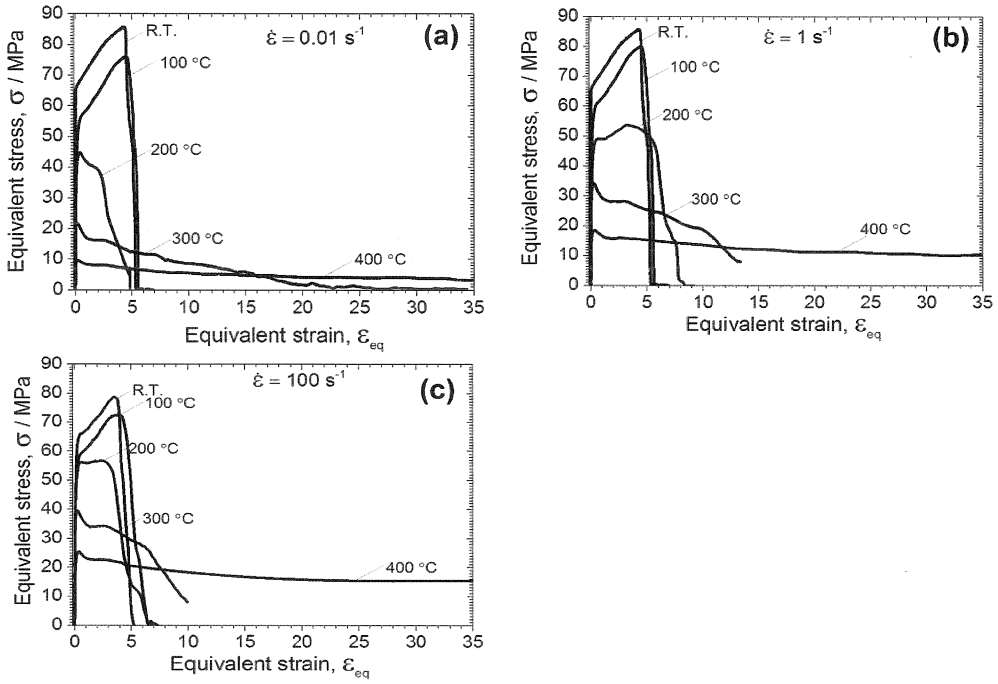

Fig. 4.14 The stress-strain curves of the aged-Al-2wt.% Cu alloy specimens deformed at various deformation temperatures from RT to 400 °C at various strain rates, (a) 10^{-2} s^{-1}, (b) 10^{0} s^{-1} and (c) 10^{2} s^{-1}.

The relationship between flow stresses, deformation temperature and strain rate could be presented by Zener-Hollomon (Z) parameter in the equations shown below [9]:

$$Z = A \cdot \sigma_M^{\,n} \tag{4.1}$$

$$Z = A' \cdot exp(\beta \cdot \sigma_M)^{\,n'} \tag{4.2}$$

$$Z = A'' \cdot [sinh(\alpha \cdot \sigma_M)]^{\,n''} \tag{4.3}$$

$$Z = \dot{\varepsilon} \cdot exp(\frac{Q}{RT}) \tag{4.4}$$

where A, A', A'', α and β are the material constants, σ_M is the maximum stress, n, n' and n'' are the stress exponents, and Q is an apparent activation energy for high temperature deformation, R is the gas constant and T is an absolute temperature. The power law, **Eq. 4.1**, and the exponential law, **Eq. 4.2**, are suitable for the low stress and the high stress

cases, respectively. Meanwhile, the hyperbolic-sine equation, **Eq. 4.3**, is applicable to both cases. The activation energy Q for the present Al-2wt.% Cu was calculated using **Eq. 4.1**. It was found that the activation energy for high temperature torsion deformation of the aged specimens was 174 kJ mol^{-1}. As this value was close to the value of 156 kJ mol^{-1} for pure Al reported by Jonas et al. [10] and used for calculating Z value in **Chapter 2**, 156 kJ mol^{-1} was again used for calculating Z values in this chapter.

Figure 4.15 (a) and **(b)** show log-log plots of the maximum stress (σ_M) obtained from the stress–strain curves in **Fig, 4.14** and $\sinh(\alpha \cdot \sigma_M)$ calculated by the hyperbolic-sine equation, as a function of Z parameter, respectively. The flow stress presented in **Fig. 4.15** can be divided into two regions depending on high Z values (region I) and low Z values (region II). Such a trend was found in the torsion deformed 1100 Al in **Chapter 2**. The transition of the flow stress from region I to region II occurs at a critical Z value (Z_c) of 3.21×10^{15} s^{-1}. The Z_c value observed in the aged Al-2wt.% Cu alloy is slightly higher than that of 1100Al.

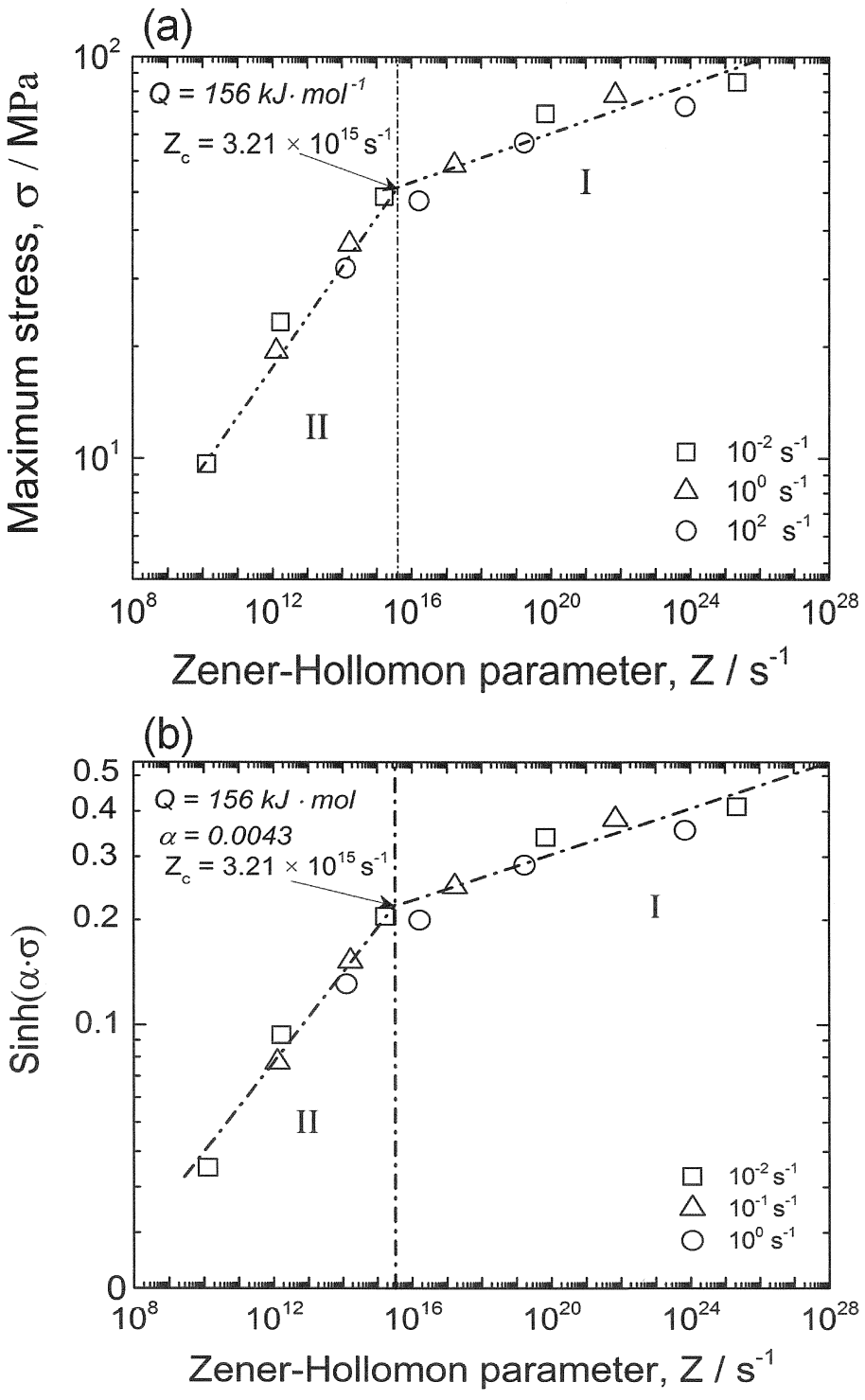

Fig. 4.15 The maximum flow stress plotted as a function of Zener-Hollomon parameters calculated by using (a) power law equation and (b) hyperbolic-sine law equation.

The n values evaluated in the regime I and II using **Eq. (4.1)** are shown in **Fig. 4.15 (a)** and **(b),** respectively. These n values are used for re-calculating the Q values (apparent activation energies for hot deformation) in region I and II using **Eq. 4.1**. In order to evaluated Q value ln σ were plotted as a function of $1/T$. The Q values evaluated are 155 and 174 kJ mol^{-1} in the region I and II, respectively. The reason of the difference in the n and Q values will be discussed later, considering the microstructures.

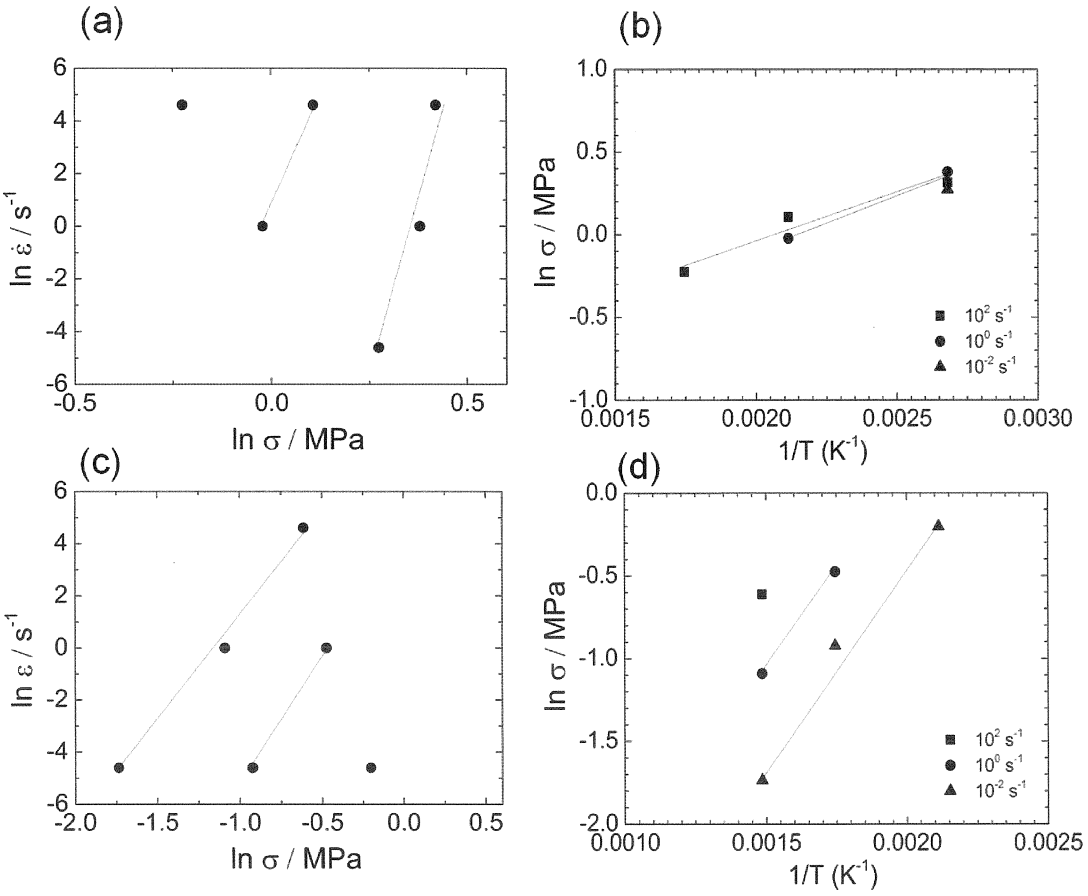

Fig. 4.16 The evaluated n and Q values in (a), (b) region I, (c) and (d) region II.

4.5.2 Microstructure evolution during torsion

EBSD measurement and TEM were carried out for the microstructure observations of the Al-2wt.% Cu alloy specimens torsion deformed under various conditions. The EBSD grain boundary maps of the aged Al-2wt.% Cu alloy specimens

torsion deformed under various Z conditions to an equivalent strain of 3.6 are shown in **Fig. 4.16**. In boundary maps, the high-angle grain boundaries ($15 \leq \theta$, where θ is the misorientation) are depicted by red lines and low-angle grain boundaries ($2 \leq \theta < 15$) as black lines, respectively. The microstructures of the specimens deformed under high Z conditions (region I) are displayed in **Fig. 4.16 (a)-(c)**. It is found that the microstructures consist of elongated fine grains aligned nearly parallel to the shear direction. Grain size increases slightly with decreasing Z value. Meanwhile, in the region II, the microstructures mainly consist of equiaxed grains (**Fig. 4.16 (d)-(e)**). The grain size increases significantly with decreasing Z parameter. These results indicated that the grain boundary migration occurred during high temperature torsion deformation.

Figure 4.17 shows TEM micrographs of the specimens deformed under various Z conditions. In the region I, the microstructures are composed of highly elongated lamellar boundary structures, which are nearly parallel to the shear direction. Most of the grains are sandwiched by very thin θ' precipitates (**Fig. 4.17 (a)**). The decrease in Z value results in the increase in the grain size, the decrease in the amount of dislocations, and the formation of clear subgrain structures. In addition, as mentioned in the previous section, the precipitates are fragmented after torsion deformation to an equivalent strain of 1.63 at room temperature (high Z value). The similar results were also observed in the specimen deformed under the deformation conditions corresponding to the region I. In **Fig. 4.17 (a)-(c)**, on the other hand, the size of the precipitates having particle morphologies increases with decreasing Z value, in other words, with increasing deformation temperature and decreasing strain rate (increasing deformation time). For example, at $Z = 4.68 \times 10^{17}\ s^{-1}$, the coarse and spherical precipitates were clearly observed at grain boundaries (**Fig. 4.17 (c)**). With further decrease in Z value below Zc,

the matrix structure completely changed from the lamellar structures to more equixed grain structures with low dislocation density and large amount of coarse and spherical precipitates. Those precipitates are located in the grain interior. The results revealed that the grain boundary migration and precipitation coarsening happened in this deformation condition.

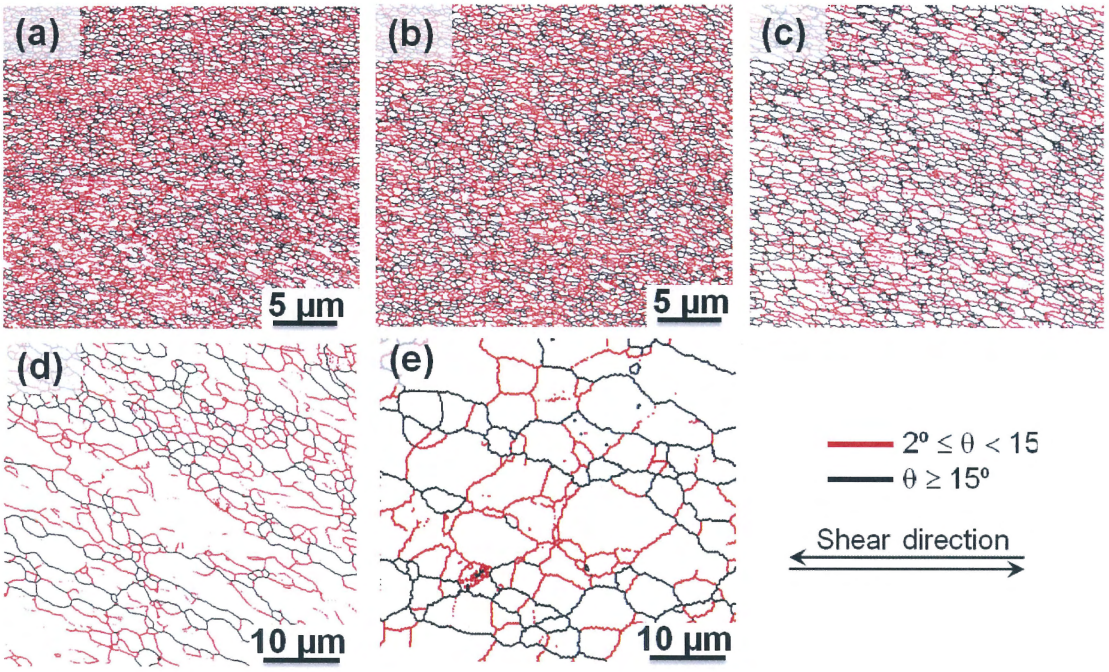

Fig. 4.17 EBSD boundary maps of the Al-2wt.% Cu alloy specimens torsion deformed to an equivalent strain of 3.6 under various Z conditions: (a) $Z = 2.55 \times 10^{24}\ s^{-1}$ (Region I), (b) $Z = 2.55 \times 10^{22}\ s^{-1}$ (Region I), (c) $Z = 4.68 \times 10^{17}\ s^{-1}$ (Region I), (d) $Z = 2.62 \times 10^{14}\ s^{-1}$ (Region II) and (e) $Z = 2.62 \times 10^{10}\ s^{-1}$ (Region II).

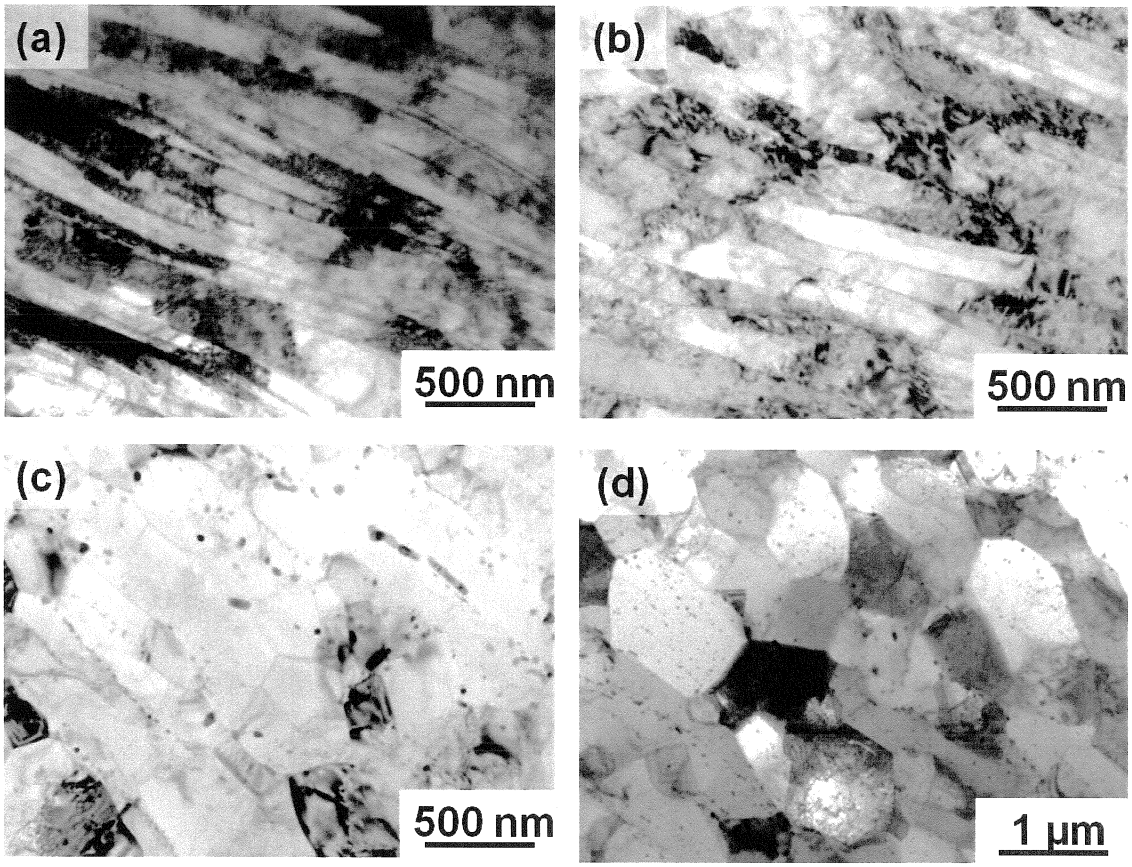

Fig. 4.16 TEM micrographs of the Al-2wt.% Cu alloy specimens torsion deformed to an equivalent strain of 3.6 under various Z conditions: (a) $Z = 2.55 \times 10^{24}\ s^{-1}$ (Region I), (b) $Z = 2.55 \times 10^{22}\ s^{-1}$ (Region I), (c) $Z = 4.68 \times 10^{17}\ s^{-1}$ (Region I), and (d) $Z = 2.62 \times 10^{10}\ s^{-1}$ (Region II).

4.5.3 Effect of Z parameter on grain size

Figure 4.18 (a) and **(b)** show the grain size and fraction of high angle grain boundary measured from the grain boundary maps presented in **Fig. 4.16**, which are plotted as a function of Z parameter in the log-log scales, respectively. The grain size and fraction of high angle grain boundary of the 1100Al deformed under the similar deformation conditions by torsion were also plotted in the figures for comparison. It is obvious in **Fig. 4.18 (a)** that the mean grain size of the aged Al-2wt.% Cu alloy specimens torsion deformed exhibits the similar trend to the 1100Al specimens. That is,

the grain size rapidly decreases with increasing Z value up to Zc, and then slightly decreases with further increase in Z value. Meanwhile, the fraction of high angle grain boundaries increases slightly with increasing Z value up to Zc. In contrast, above Zc, the fraction of high-grain boundaries decreases with increasing Z value as shown in **Fig. 4.18 (b).** It is also found that in the region I the grain size of the Al-2wt.% Cu alloy is significantly finer than that of the 1100Al, while the fraction of high angle grain boundary is significantly lower than that of the 1100Al. The results indicate that the θ′ plate precipitates inhibit the formulation of high angle grain boundary.

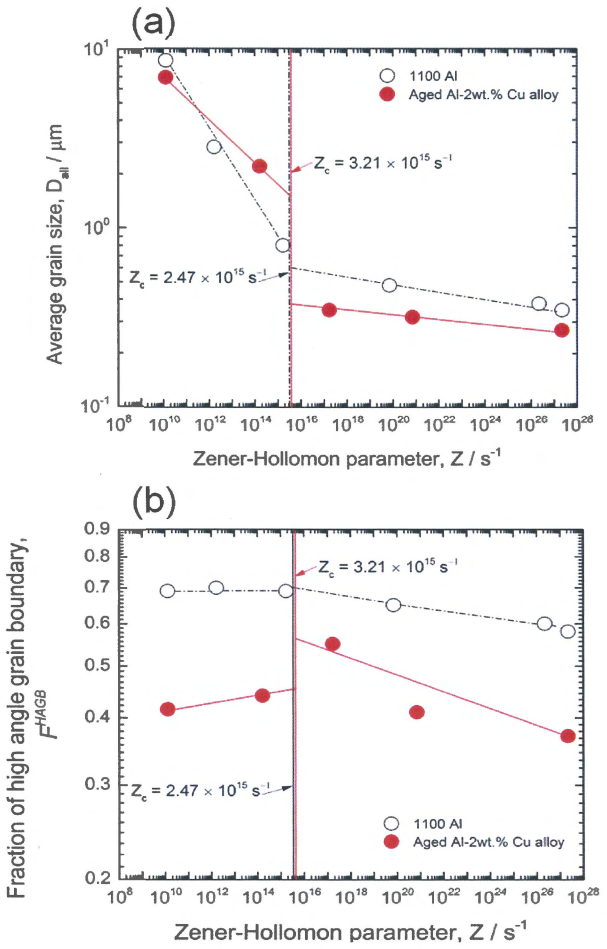

Fig. 4.18 (a) Average grain size (D_{All}) and (b) fraction of high angle boundaries (F^{HAGB}) of the torsion deformed Al-2wt.% Cu alloy and 1100 Al plotted as a function of Z parameter in log-log scale.

4.5.4 Discussion

The stress-strain results indicated that the flow stress and the shape of the stress-strain curves are significantly dependent on the deformation conditions, i.e. strain rate and deformation temperature, in other words, Z parameter. The flow stress tended to decrease with decreasing the Z parameter. Two different regions were observed in the plot of the maximum flow stress (σ_M) versus Z parameter. The differences between these two regions are discussed in terms of microstructure evolution mechanism.

In the region I, the stress-strain curves of the specimens deformed under high Z conditions ($Z \geq Z_c$) exhibited work hardening type. The n and Q values evaluated from the stress-strain results are 24 and 155 kJ mol^{-1}, respectively. This n value is quite high, which is two times higher than that of 1100Al (n = 12, in **Chapter 2**). The high n value may be caused by the presence of the θ′ precipitates [11]. Meanwhile, the evaluated Q value is slightly higher than the activation energy for self-diffusion of aluminum (142 kJ mol^{-1}) [12], the activation energy for diffusion of copper in aluminum (138 kJ mol^{-1}) [13], and the activation energy for hot deformation of the 1100Al deformed under the similar deformation conditions by torsion deformation (128 kJ mol^{-1}) (**Chapter 2**). The increase in the activation energy may be due to the existence of the θ′ precipitates and must reflect the difference in the microstructural evolution during deformation. In the 1100Al, the TEM micrographs showed that the microstructure consisted of elongated grains, grains were subdivided by mainly high angle grain boundary, and the subgrain structures were formed in the grain interiors, which caused by the rearrangement and annihilation of the dislocations (**Fig. 2.15 (b), Chapter 2**). Meanwhile, the microstructure of the aged Al-2wt.% Cu alloy specimens composed of the highly elongated grains sandwiched by very thin θ′ precipitates and most of the grains had

high density of the dislocations (**Fig. 4.17 (a)**). The amount of dislocations decreased with decreasing Z value (**Fig. 4.17 (b)**), which was attributed to the dislocation annihilation during the deformation process due to dynamic recovery. In addition, the density of dislocations in the aged Al-2wt.% Cu alloy was higher than that of 1100Al. This may be due to the decrease in dynamic recovery rate and the restriction of dislocation motion by precipitates. It can be concluded that grain subdivision and dynamic recovery of dislocations are the main microstructural evolution mechanism in the high Z value.

In the region II, the specimens exhibited sharp drop of the flow stress and steady state. The n and Q values are 8 and 174 kJ mol^{-1}, respectively. This Q value was closed to the activation energy for the grain boundary migration in pure aluminum (172 kJ mol^{-1}). These n and Q values are higher than those of the 1100Al deformed under the same deformation parameters (**Chapter 2**: 4.5 and 164 kJ mol^{-1}). The difference in n and Q value may be due to the different stress-strain behavior and microstructure evolution during torsion deformation. That is, the stress-strain curves of the aged Al-2wt.% Cu showed large drop of the flow stress. It has been claimed that the softening of the flow stress in the aluminum alloy was caused by the coarsening of precipitates during hot deformation [14-17] and grain boundary migration. The microstructures qualitatively support this interpretation. That is, the microstructures composed of the equiaxed grains containing low density of dislocations and coarse spherical precipitates.

4.5.5 Summary

The effects of deformation conditions on the stress-strain behavior and microstructure evolution in the pre-aged Al-2wt.% Cu alloy were investigated. The following conclusions can be made.

1. The flow stress and the shapes of the stress–strain curves were strongly dependent on the deformation conditions. At low temperature (T < 300 °C), the specimens exhibited a stress-strain curves of work hardening type. The large drop of the flow stress and steady state flow stress were observed in the specimen deformed at high temperature (T ≥ 300 °C). The aged Al-2wt.% Cu alloy exhibited the different shape of the stress-strain curve from those of the 1100Al deformed under the same deformation conditions, especially, at high deformation temperatures. The drop of the flow stress in the aged Al-2wt.% Cu alloy was clearer than that of the 1100Al. The flow softening in the Al-2wt.% Cu alloy was attributed to the coarsening of precipitates and grain boundary migration occurred during hot deformation.

2. The dependence of flow stress on the deformation conditions was fitted to a power law relationship using the Zener-Hollomon (Z) parameter. The two different regions were observed in the σ-Z plot. The changes of the slope occurred at a critical Z value of 3.21×10^{15} s^{-1}. The activation energies (Q) were 155 and 174 kJ mol^{-1} and the stress exponents (n) were 24 and 8 for the high Z and low Z regions (regions I and II), respectively. The Q and n values observed in the aged Al-2wt.% Cu alloy were significantly higher than those of the 1100Al deformed under the same deformation

conditions. The difference in the Q and n values was attributed to the presence of the θ′ precipitates and reflected the microstructure evolution mechanism.

3. The main microstructure evolution mechanism in the region I was found to be grain subdivision and dynamic recovery of dislocations. Meanwhile, grain boundary migration and coarsening of precipitates were found to be the main microstructure evolution mechanism operated in the region II.

4. The grain size decreased and fraction of high-angle grain boundary increased with decreasing Z parameter. The grain size of the Al-2wt.% Cu alloy was finer than that of the 1100Al deformed under the similar deformation conditions. However, the fraction of high-angle grain boundary in the Al-2wt.% Cu alloy was significantly lower than 1100Al. The results indicate that the θ′ plate precipitates significantly inhibited the formulation of high angle grain boundary.

4.6 Conclusions

In **Chapter 4**, the effect of pre-existing θ′ precipitates on the formation of UFG structures in the Al-2wt.% Cu alloy was systematically investigated. The solution treated and aged Al-2wt.% Cu alloy specimens were deformed to various equivalent strains at room temperature under a constant strain rate of 1 s^{-1}. The grain size of the solution treated and aged Al-2wt.% Cu alloy tended to decrease with increasing equivalent strain. However, the mean grain size and fraction of high-angle grain boundary of the solution treated specimens after strain of 3.27 was finer and higher than that of the aged Al-2wt.% Cu alloy specimen. The results indicated that the presence of fine θ′ plate precipitates inhibited the development of high angle grain boundaries and the formation of fine grain structures.

The effects of deformation conditions on the stress-strain behavior and microstructure evolution in the pre-aged Al-2wt.% Cu alloy were also investigated. Comparing the stress-strain curves of the aged Al-2wt.% Cu alloy with those of 1100Al, it was found that the shape of the stress- strain curves in the aged 2wt.% Cu alloy specimens were greatly different from those in the 1100Al deformed under the same deformation parameters, especially at high temperatures (above 200 °C). The flow softening in the aged Al-2wt.% Cu alloy specimens was clearer than that in the 1100Al specimens. These results indicated that the pre-existing θ′ precipitates strongly affected the stress-strain behavior in heavy (torsion) deformation of the aluminum alloy. Microstructure observations indicated that the flow softening in the aged Al-2wt.% Cu alloy was caused by coarsening of precipitates and grain boundary migration occurred during high temperature deformation. The flow stress of the aged Al-2wt.% Cu alloy was also strongly dependent on the Z parameter. The maximum stress decreased with

decreasing Z values. The change in the slope of σ-Z plot occurred at a critical Z value (Z_c) of 3.21×10^{15} s^{-1}. Microstructure observations showed that the structure obviously changed at Z_c from elongated grain sandwiched by thin θ′ precipitates to equiaxed grains containing coarse precipitates. The grain size and the fraction of high-angle grain boundary of the aged Al-2wt.% Cu alloy showed the similar trend with that of the 1100Al, i.e., the grain size tended to decrease with increasing Z parameters. The fraction of high-angle grain boundary increased slightly with increasing Z value up to Zc, then decreased significantly with further increasing Z value. At high Z region, the fraction of high-angle grain boundary in the aged Al-2wt.% Cu alloy was significantly lower than that of the 1100Al deformed under the similar deformation conditions.

Based on the results in **Chapter 4**, it could be concluded that the θ′ precipitates and deformation conditions strongly affected the microstructure evolution in the aluminum alloys. The presence of fine θ′ plate precipitates inhibited the development of fine grain structures composed of high angle grain boundaries. The stress-strain curve analysis and microstructure results revealed that the grain subdivision and dynamic recovery were the main microstructure evolution mechanism operated in the high Z region (region I). Meanwhile, at low Z region (region II), the grain boundary migration and coarsening of precipitates were the main microstructure evolution mechanism.

References

[1] Nam C, Han J, Chung Y and Shin M
Effect of precipitates on microstructural evolution of 7050 Al alloy sheet during equal channel angular rolling.
Mater Sci Eng A (2003) 347:253-257.

[2] Murayama M, Horita Z and Hono K
Microstucture of two-phase Al-1.7 at % Cu alloy deformed by equal-channel angylar pressing.
Acta Mater (2001) 49:21-29.

[3] Ringer SP and Hono K
Microstructural evolution and age hardening in aluminium alloys: atom probe field-ion microscopy and transmission electron microscopy studies.
Mater Charact (2000) 44:101-131.

[4] Tsuji N, Iwata T, Sato M, Fujimoto S and Minamino Y
Aging behavior of ultrafine grained Al-2 wt%Cu alloy severely deformed by accumulative roll bonding.
Sci Tech Adv Mater (2004) 5:173-180.

[5] Hughes D and Robertson WD
The mechanism of hardening in aged aluminum-copper alloys.
Acta Metall (1960) 8:156-167.

[6] Noble B, Malauchlin IR and Thompson G
Clustering processes in aluminum-copper.
Acta Mater (1970)18:339-345.

[7] Ringer SP, Sofyan BT, Prasad KS and Quan GC
Precipitation reactions in Al–4.0Cu–0.3Mg (wt.%) alloy.
Acta Meter (2008) 56:2147-2160.

[8] Berta M and Prangnell PB
Effect of processing route and second phase particles on grain refinement during equal-channel angular extrusion.
Mater Sci Eng A (2005) 410-411:381-385

[9] Sellars CM and Mctegart WJ Farghalli
On the mechanism of hot deformation.
Acta Mater 14:1136-1138.

[10] Jonas JJ, Sellars CM and Tegart WJ
Strength and structure under hot-working conditions.
Int Mater Rev (1969) 14:1-24.

[11] Wang J, Wu X and Xia K
Creep behaviour at elevated temperatures of an Al-Cu-Mg-Ag alloy.
Mater Sci Eng A (1997) 234-236: 287-290.

[12] Lundy TS and Murdock FJ
Diffusion of Al26 and Mn54 in aluminum
J Appl Phy (1962) 33:1671.

[13] Farghalli A
Creep Characteristics of an AI-2wt.% Cu Alloy in the solid solution Range.
Mater Sci Eng A (1988) 101: 13-23

[14] Verlinden B, Wouters P, Leuven KU, McQueen HJ, Aernoudt E, Delaey L, Leuven KU, Cauwenberg S and Sidal NV
Effect of different homogenization treatments on the hot workability of aluminium alloy AA2024.
Mater Sci Eng A (1990) 123: 229-237.

[15] Wouters P, Verlinden B, Mcqueen HJ, Aernoudt E, Delaey L, Leuven KU, Cauwenberg S, and Sidal NV
Effect of homogenization and precipitation treatments on the hot workability of an aluminium alloy AA2024.
Mater Sci Eng A (1989) 123: 239-245.

[16] Ebrahimi GR, Zarei-Hanzaki A, Haghshenas M and Arabshahi H
The effect of heat treatment on hot deformation behaviour of Al 2024.
J Mater Proc Tech (2008)206: 25-29.

[17] Cavaliere P
Hot and warm forming of 2618 aluminium alloy.
J Light Metal (2002) 2:247-252.

Chapter 5 Summary and conclusions

In the present dissertation, the effects of deformation conditions and precipitate on the changes in the microstructure and mechanical properties of aluminum alloys heavily deformed by torsion deformation have been clarified. Commercial purity aluminum (1100Al) and Al-2wt.% Cu alloy were used as the investigation materials. In order to study the influences of deformation parameters on the microstructure evolution in aluminum, the 1100Al specimens were deformed in torsion to various strains at five different temperatures and four different strain rates. The microstructures of the torsion deformed 1100Al specimens were characterized by EBSD measurement and TEM. Meanwhile, the mechanical properties of those deformed specimens were examined by tensile test at room temperature. On the other hand, the influence of pre-existing precipitate on the microstructural evolution in aluminum was also researched in the present work. For this study, the Al-2wt.% Cu alloy specimens were firstly solution treated at 550 °C for 1 h and then aged at 180 °C for 3600 ks (100 h) to obtain θ′ precipitates having thin plate morphologies. Then the aged specimens were deformed to various strains at three different strain rates and three different deformation temperatures. Microstructure and hardness of the deformed specimens were characterized by TEM, EBSD measurement and micro-hardness test.

The main results achieved in the present dissertation can be summarized as follows:

In **Chapter 1**, the background and purpose of the present work were elucidated.

In **Chapter 2**, the evolution of microstructures in the 1100Al heavily deformed by torsion deformation was systematically studied. Microstructure observations revealed that the change in the grain size and misorientation angle of the commercial

purity aluminum deformed by torsion showed similar trend with that deformed by ARB process. That is, the grain size decreased and the fraction of high angle grain boundary increased with increasing strain. The ultrafine grained structure with a mean grain size of 0.32 μm having large amounts of high angle grain boundaries (76 %) were achieved by torsion after a strain of 5.27. The results indicated that torsion deformation worked as a kind of severe plastic deformation.

The influences of deformation temperature and strain rate on the microstructural evolution in 1100Al during torsion deformation were also systematically studied at wide ranges of strain, deformation temperature and strain rate. The strain rate and deformation temperature were combined into a single parameter, i.e., Zener-Hollomon (Z) parameter. The flow stress of the specimens deformed under various Z conditions (various strain rates and deformation temperatures) tended to decrease with decreasing Z value. A transition of flow stress in the σ-Z plot was observed at a critical Z value of 2.47×10^{15} s^{-1}. The flow stress and microstructure indicated that the transition in the σ–Z plot could be attributed to the change in the mechanism of microstructure evolution from dynamic recovery governed by dislocation cross slip to grain boundary migration accompanied with dislocation climb at grain interior.

In **Chapter 3**, the mechanical properties of the ultrafine grained (UFG) aluminum fabricated by torsion deformation at various Z values were systematically investigated by tensile test at room temperature. The strengthening mechanisms of the UFG materials were also clarified. The strength of the UFG aluminum increased with increasing Z values, i.e., with decreasing the grain size. Meanwhile, the tensile ductility decreased gradually with decreasing the grain size. These results were similar with those of the UFG aluminum fabricated by ARB process and subsequent annealing at

various temperatures. However, at the grain sizes below 1 μm, the yield strength of the torsion deformed specimens was significantly lower than that of the ARB processed and annealed specimens. This was caused by the difference in the microstructures of the UFG aluminum produced by torsion deformation and that by ARB and annealing. In addition, the yield stress obtained from the UFG aluminum produced by torsion deformation was significantly higher than that predicted from the Hall-Petch relationship for the coarse grain aluminum cold-rolled and annealed. The extra hardening in the torsion specimens was attributed mainly to the substructure strengthening

In **Chapter 4**, the effect of pre-existing θ′ on the formation of UFG structure in the Al-2wt. % Cu alloy was systematically investigated. The solution treated and aged Al-2wt.% Cu alloy specimens were heavily deformed by torsion deformation at room temperature under a constant strain rate of 1 s^{-1}. The grain size of the solution treated and aged Al-2wt.% Cu alloy tended to decrease with increasing equivalent strain. However, the mean grain size of the solution treated specimens after imposed strain of 3.6 was finer than that of the aged Al-2wt.% Cu alloy specimen. The results indicated that the presence of fine θ′ plate precipitates inhibited the development of high angle grain boundaries and the formation of fine grain structures.

The effects of deformation conditions on the stress-strain behavior and microstructure evolution in the pre-aged Al-2wt.% Cu alloy were also investigated. Comparing the stress-strain curves of the aged Al-2wt.% Cu alloy with those of 1100Al, it was found that the shape of the stress-strain curves in the aged Al-2wt.% Cu alloy specimens were greatly different from those in the 1100Al deformed under the same deformation parameters, especially at high temperature deformation (above 200 °C).

The flow softening in the aged Al-2wt.% Cu alloy specimens was clearer than that in the 1100Al specimens. These results indicated that the pre-existing θ′ precipitates strongly affected the stress-strain behavior in heavy (torsion) deformation of the aluminum alloy. Microstructure observations indicated that the flow softening in the aged Al-2wt.% Cu alloy was caused by coarsening of precipitates during hot deformation. The flow stress of the aged Al-2wt.% Cu alloy was also strongly dependent on the *Z* parameter. The maximum stress decreased with decreasing Z values. The change in the slope of σ-*Z* plot occurred at a critical *Z* value (Z_c) of 2.1×10^{18} s^{-1}. Microstructure observations showed that the structure obvious changed from the elongated grain sandwiched by the thin θ′ precipitates to the equiaxed grains contained of the coarse precipitates at *Zc*. The grain size and the fraction of high-angle grain boundary of the aged Al-2wt.% Cu alloy showed the similar trend with that of the 1100Al, grain size tended to decrease with increasing the *Z* parameters. The fraction of high-angle grain boundary increased slightly with increasing *Z* value up to Z_c, then decreased significantly with further increasing *Z* value. At high *Z* condition, the fraction of high-angle grain boundary of the aged Al-2wt.% Cu alloy was significantly lower than that of the 1100Al deformed under the similar deformation conditions.

The results in this chapter indicated that the θ′ precipitates and deformation conditions strongly affected on the microstructure evolution in the aluminum alloys. The presence of fine θ′ plate precipitates inhibited the development of fine grain structures surrounded by high angle grain boundaries. The stress-strain curve analysis and microstructure results revealed that grain subdivision and dynamic recovery governed by dislocation cross-slip were the main microstructure evolution mechanism operated in the high *Z* conditions (region I). Meanwhile, at low *Z* conditions (region II),

the grain boundary migration and coarsening of precipitates were the main microstructure evolution mechanism.

Acknowledgements

I would like to express my sincere gratefulness to Professor Nobuhiro Tsuji of Kyoto University, my supervisor, for the encouragement, personal guidance, assistance and valuable suggestions enabling me to steer my research work efficiently and effectively. I also would like to acknowledge my co-supervisor, Dr. Daitsuke Terada of Kyoto University and Associate Professor Hiroshi Adachi of University of Hyogo, for their valuable comments and supports. On the other hand, I also would like to thank Prof. Ei-ichiro Matsubara and Prof. Hideyuki Yasuda for accepting to evaluate my thesis.

Special thanks to the Ministry of Education, Culture, Sports, Science and Techology (MEXT) of Japan for their generosity in giving me the opportunity of Japanese Government Scholarship and financial support to pursue my doctoral degree.

I would like to express my sincere gratitude to all of my teachers starting from Primary School until now. Their nourishment facilitated me to reach this height.

I also would like to convey thanks to all my friends in Tsuji lab for their great companion and friendship, especially Dr. Nokeun Park for his kind help and supports.

Finally, I would like to take this opportunity to express my heartfelt sincere thanks to my beloved parents; Somneuk Khamsuk and Song Khamsuk who have been involved in raising me up to the height that I am in at present with their love, courage and support. I dedicated this thesis to them. My special appreciation and gratitude goes to my sister, my auntie and their families for their love and kindness.

List of publications:

Publications (Journal articles):

1. Sunisa Khamsuk, Nokeun Park, Hiroki Adachi, Daisuke Terada and Nobuhiro Tsuji, "Nanostructure Evolution in Commercial Purity Aluminum Heavily Deformed by Torsion",
J. Mater. Sci., Vol.47, No.22 (2012), pp.7841-7847.

2. Sunisa Khamsuk, Nokeun Park, Gao Si, Daisuke Terada, Hiroki Adachi and Nobuhiro Tsuji,
"Mechanical properties of bulk ultrafine grained aluminum fabricated by torsion deformation at various temperatures and strain rates",
submitted, Mater. Trans. (2013)

3. N. Park, S. Khamsuk, A. Shibata and N. Tsuji,
"Effect of austenite grain size on kinetics of dynamic ferrite transformation in low carbon steel",
Scripta Mater., Vol. 68 (2013), pp 611-614.

4. Nokeun Park, Sunisa Khamsuk, Akinobu Shibata, Nobuhiro Tsuji,
"Occurrence of dynamic ferrite transformation in low-carbon steel above Ae3",
Scripta Mater., Vol. 68 (2013), pp 538-541.

Conferences attended:

1. Sunisa Khamsuk, Nokeun Park, Gao Si, Daisuke Terada, Hiroki Adachi and Nobuhiro Tsuji,
"Mechanical properties of bulk ultrafine grained aluminum fabricated by torsion deformation"
International symposium on strength of fine grained materials - 60 years of hall-petch, (2013), University of Tokyo, Japan.

2. Sunisa Khamsuk, Nokeun Park, Daisuke Terada, Hiroki Adachi and NobuhiroTsuji,
"Influence of deformation conditions on microstructure and texture in commercial purity aluminum heavily deformed by torsion",
Proceeding of meeting of the Japan institute of metals, (2012), Ehime University, Japan.

3. S.Khamsuk, N.Park, D.Terada, H.Adachi and N.Tsuji,
"Deformation temperature and strain rate dependence of microstructure evolution in torsion deformation of commercial purity aluminum", International conference on the strength of the 16th-metal alloy (ICSMA 16), (2012), Bangalore, India.

4. S.Khamsuk, N.Park, D.Terada, H.Adachi and N.Tsuji,
"Influence of zener-hollomon parameter on formation of ultrafine grained aluminum in torsion deformation",
Bulk nanometal international workshop, (2012), Kyoto University, Japan.

5. Sunisa Khamsuk, Nokeun Park, Daisuke Terada, Hiroki Adachi and NobuhiroTsuji,
"Effects of strain rate and temperature on microstructure evolution in high purity aluminum during torsion deformation",
Proceeding of meeting of the Japan institute of metals, (2011), Yokohama university national, Japan.

6. S.Khamsuk, N.Park, D.Terada, H.Adachi and N.Tsuji,
"Change in microstructure and texture during hot torsion deformation of commercial purity aluminum",
60th anniversary of the light metals society, (2011), Kansai University, Japan.

7. Sunisa Khamsuk, Hiroki Adachi and Nobuhiro Tsuji,
"Effect of strain on microstructure and hardness of 1100 aluminum highly deformed by torsion"
Joint symposium on materials science and engineering 2011, (2011), Nanyang Technological University, Singapore.

8. Sunisa Khamsuk, Nobuhiro Tsuji and Hiroki Adachi,
"Effect of strain on nanostructure formation in pure aluminum deformed by torsion",
German-Japanese Symposium on Nanostructures international symposium, (2011), Ritsumeikan University, Japan.